Physik-Department

Munich School of Bioengineering

Diagnostic MRI Relaxometry for Sensitive Detection of Magnetically Labelled Particles in Biological Systems

Alexander Clemens Joos

Vollständiger Abdruck der von der Fakultät für Physik der Technischen Universität München zur Erlangung des akademischen Grades eines

Doktors der Naturwissenschaften (Dr. rer. nat.)

genehmigten Dissertation.

Vorsitzender:		Prof. Dr. Martin Zacharias
Prüfer der Dissertation:	1.	Prof. Dr. Axel Haase
	2.	Priv.-Doz. Dr. Marion I. Menzel

Die Dissertation wurde am 19.10.2017 bei der Technischen Universität München eingereicht und durch die Fakultät für Physik am 18.12.2017 angenommen.

Abstract

Magnetic nanoparticles (MNPs) can be assembled with pharmaceutical agents, injected into the body and directed to diseased tissues using external magnets where the agent is released - a method called magnetic drug targeting. Due to their strong contrast enhancing properties, the therapy progress can be monitored non-invasively using MRI relaxometry. Since MNPs affect the MRI contrast only indirectly by shortening relaxation times of water protons, comprehensive in-vitro characterisation of the particles and the particle-agent complexes have to be performed to allow for reliable in-vivo therapy monitoring. In this work, several characterisation methods were employed, studied and improved which is expected to contribute to the successful use of MNPs for drug targeting. First, room temperature Mössbauer spectroscopy combined with external magnetisation of particle samples was shown to be a potent technique for the quality assessment of MNP synthesis even for particles with sizes below 15 nm. Second, NMR relaxation measurements of particles fractionated by size was shown to be a new method that can test the suitability of a given particle system for quantification using MRI relaxometry and also allows for verification of relaxation theories. Third, extensive MRI relaxometry experiments were performed. The results confirmed that R_1 and R_2 relaxation rates are sensitive to complex formation and cell incorporation while R_2^* rates are more suitable for particle quantification. In addition, two general conclusions can be drawn from these experiments regarding their practical implementations. First, sequences for fast R_1, R_2 and R_2^* mapping are not available on all MRI systems and often suffer from severe artifacts. MRI system, sequences and sequence parameters thus have to be chosen with care. Second and most importantly, any air inside the in-vitro samples has to be strictly avoided in order to prevent susceptibility artifacts.

Zusammenfassung

Magnetische Nanopartikel (MNPs) können an pharmazeutische Wirkstoffe gebunden, in den Körper injiziert und mithilfe externer Magnetfelder im krankhaften Gewebe angesammelt werden, wo sie die Wirkstoffe freigeben - diese Methode heißt *magnetic drug targeting*. Aufgrund ihrer kontrastverstärkenden Eigenschaften kann der Fortschritt der Therapie nichtinvasiv mittels MRT Relaxometrie überwacht werden. Da MNPs den MRT Kontrast nur indirekt über eine Verkürzung der Relaxationszeiten der Wasserprotonen beeinflussen, muss eine umfassende in-vitro Charakterisierung der Partikel und der Partikel-Wirkstoff Komplexe durchgeführt werden, um eine zuverlässige Kontrolle der Therapie zu ermöglichen. In dieser Arbeit wurden mehrere Charakterisierungmethoden verwendet, untersucht und verbessert. Es wird erwartet, dass dies zur erfolgreichen Verwendung von magnetischen Nanopartikeln für das *magnetic drug targeting* beiträgt. Erstens wurde gezeigt, dass Mößbauerspektroskopie bei Raumtemperatur in Kombination mit einem äußeren Magnetfeld zur Magnetisierung der Partikelproben eine wirkungsvolle Methode ist, um die Produktionsqualität von Partikeln zu bewerten, selbst für solche mit einem Durchmesser unterhalb von 15 nm. Zweitens ist die Messung der NMR Relaxationszeiten von größensortierten Partikeln eine neue Methode, mit der die Eignung des Partikelsystems für die Quantifizierung mittels MRT Relaxometrie geprüft werden kann. Diese Methode kann außerdem verwendet weden, um Relaxationstheorien zu überprüfen. Drittens wurden umfangreiche MRT Relaxometrieexperimente durchgeführt. Die Ergebnisse bestätigen, dass die R_1 und R_2 Relaxationsraten sensibel auf die Bildung von Komplexen und die Aufnahme der Partikel in Zellen reagieren, während die R_2^* Raten eher zur Partikelquantifizierung geeignet sind. Zusätzlich können zwei allgemeine Schlussfolgerungen bezüglich der praktischen Umsetzung aus diesen Experimenten gezogen werden. Erstens sind schnelle Sequenzen zur quantitativen R_1, R_2 und R_2^* Bildgebung nicht auf allen MRT-Geräten vorhanden oder leiden unter schweren Artefakten. MRT-Scanner, Sequenzen und Sequenzparameter müssen daher sorgfältig ausgewählt werden. Zweitens müssen Luftblasen innerhalb der in-vitro Proben unbedingt vermieden werden, damit keine Suszeptibilitätsartefakte auftreten.

Contents

1. Introduction

Magnetic nanoparticles (MNPs) have been used for several biomedical applications such as bioseparation, transfection, hyperthermia and magnetic drug targeting and are promising tools for the treatment of different conditions such as cancer and heart diseases [1, 2, 3, 4, 5]. For magnetic drug targeting, MNPs are bound to pharmaceutical agents such as anticancer molecules or viruses and then injected into the body. Using strong external magnets, the MNP complexes can subsequently be assembled at the location of the disease where they release the active agent. In addition to their use for treatment itself, the strong contrast enhancing properties of MNPs can be exploited for non-invasive therapy monitoring using magnetic resonance imaging (MRI) relaxometry. Relaxometry refers to the measurement of the relaxation times T_1, T_2 and T_2^* and can, in principle, be used to assess both the spatial distribution of particle concentration as well as their aggregation state and degree of cell incorporation [6, 7, 8, 9]. However, in contrast to other imaging modalities such as magnetic particle imaging, which measures a signal produced by the particles themselves, MRI only detects the influence of MNPs on the relaxation times of water protons. This makes the application of MRI relaxometry to therapy monitoring in biological tissue inherently challenging. In order to obtain reliable information from the measurement of relaxation times in-vivo, one needs to collect as much in-vitro information as possible about the system of MNPs and biological components, such as viruses and cells. A number of different characterisation methods exist that can be used to assess the composition, stability, size, magnetic properties and MRI relaxation behaviour of MNPs. Some of these techniques have been used, evaluated and improved in this work and the results are presented in three main experimental chapters.

In the first main experimental chapter (Chapter 3), a new method for characterising the iron composition of small MNPs (diameter < 15 nm) using Mössbauer spectroscopy is presented. MNPs are usually composed of two types of iron oxides - magnetite and maghemite. Magnetite is preferred due to its higher magnetisability and the resulting stronger contrast enhancing properties. Moessbauer spectroscopy can differentiate between magnetite and maghemite and can therefore be used for quality assessment of the MNP synthesis. This

chapter is based on a previous publication [10]. Chapter 4 is based on another publication and deals with the fundamental NMR relaxation behaviour of particles of different sizes [11]. A relatively new method for hydrodynamic size fractionation was used to test existing relaxation theories and evaluate the suitability of a particle system for quantification through MRI relaxometry. This chapter also contains a section describing a Monte Carlo method for the simulation of T_2 and T_2^* relaxation times that can contribute to the understanding of relaxation mechanisms. The third experimental section, Chapter 5, describes extensive MRI experiments that have been conducted to test the ability of MRI relaxometry to quantitatively assess the distribution and aggregation state of MNPs and MNPs bound to viral targets in biological systems.

Each of these experimental chapters contains its own introduction outlining the current state of research and sections presenting the employed methods, results, discussion and conclusion. In Chapter 6, all findings are summarised and correlated and an outlook regarding future experiments is given. In the general theory part (Chapter 2), the background information necessary for the understanding of the experimental chapters is described.

2. Theory

2.1. Nuclear Magnetic Resonance (NMR)

Nuclear magnetic resonance was first discovered by Isidor Isaac Rabi which earned him the 1944 Nobel Prize in Physics. Rabi and his team were using a modified version of the Stern-Gerlach experiment to precisely measure the magnetic moment of molecules and atomic nuclei by applying an additional, oscillating field at the same time [12]. In 1946, Felix Bloch and Edward Mills Purcell independently performed the first NMR experiments on liquid and solid samples [13, 14], for which they received the Nobel Prize in Physics in 1952. The NMR phenomenon is the basis for both NMR spectroscopy and magnetic resonance imaging (MRI).

In the following, the basic principles of NMR that are necessary for the understanding of Chapter 4 and of magnetic resonance imaging will be reviewed. More detailed descriptions can be found in "'Principles of Nuclear Magnetism"' [15] and "'Spin Dynamics"' [16].

2.1.1. Spin and Magnetism of Atomic Nuclei

Spin is an intrinsic and quantum mechanical property of elementary particles. As the name suggests, it bears a strong resemblance to classical angular momentum. In contrast to its mechanical counterpart, however, spin is not caused by the spinning of a mass and when measured, it can only assume discrete values. All elementary particles have a fixed spin quantum number s. Particles with a half-integer spin such as $\frac{1}{2}, \frac{3}{2}, \frac{5}{2}$ are called fermions with electrons and quarks being the best-known examples. Particles with an integer spin such as $0, 1, 2$ are known as bosons with the most prominent representative being the photon. The spin quantum number should not be confused with the closely related norm of the spin vector $\left|\widehat{\mathbf{S}}\right|$ or the secondary spin quantum number m_s:

$$\left|\widehat{\mathbf{S}}\right| = \hbar\sqrt{s(s+1)} \tag{2.1}$$

$$\widehat{S}_\mathrm{z}\left|s, m_\mathrm{s}\right\rangle = \hbar m_\mathrm{s}\left|s, m_\mathrm{s}\right\rangle \quad . \tag{2.2}$$

The eigenvalue Equation 2.2 means that m_s is the z-component of the spin vector ranging from $-s$ to $+s$ in steps of one. For composite particles, the spins and angular momenta of their constituents become coupled resulting in a total spin quantum number. Being composed of protons and neutrons (which in turn consist of quarks), an atomic nucleus is such a composite particle. The nuclear spin I has a half integer value and is therefore > 0 for nuclei consisting of odd numbers of protons or neutrons. Well known examples are the $^1\mathrm{H}$ nucleus (proton) and the $^{13}\mathrm{C}$ nucleus.

A nuclear spin greater than zero always results in a nuclear magnetic moment $\boldsymbol{\mu}$, which is a necessary condition for nuclear magnetic resonance:

$$\boldsymbol{\mu} = \gamma \mathbf{I} \ . \tag{2.3}$$

γ is the gyromagnetic ratio which has a characteristic value for every type of particle or nucleus. The values for the proton and the electron are $\gamma_\mathrm{Proton} = 2.675 \times 10^8\ \mathrm{s^{-1}T^{-1}}$ and $\gamma_\mathrm{Elektron} = 1.76 \times 10^{11}\ \mathrm{s^{-1}T^{-1}}$, respectively. For this reason, the magnetic moment of the electron is greater than the magnetic moment of the proton by a factor of 658, which is essentially the reason for the small signals measured in NMR compared to ESR (electron spin resonance). If a nucleus with a magnetic moment is placed in a magnetic field, its Hamiltonian reads:

$$\widehat{H} = \widehat{H}_\mathrm{int} + \widehat{V} \quad \text{with} \quad \widehat{V} = -\widehat{\boldsymbol{\mu}}\mathbf{B} \ , \tag{2.4}$$

where $\widehat{H}_\mathrm{int}$ is the Hamiltonian for the interaction among the nucleons themselves and $\widehat{V}$ represents the interaction with the external magnetic field. Given a time independent field in z-direction $\mathbf{B} = (0, 0, B_0)$ and assuming that $\widehat{H}_\mathrm{int} \gg \widehat{V}$, one can employ first order perturbation theory to calculate the splitting of the nuclear energy levels due to the external field (Zeeman effect):

$$E^Z_{\mathrm{m_I}} = -\gamma \hbar B_0 m_\mathrm{I} \ . \tag{2.5}$$

For a hydrogen nucleus (proton) with $I = \frac{1}{2}$, there are therefore two energy eigenstates and m_I can assume the two values $-\frac{1}{2}, +\frac{1}{2}$. The proton can be brought from the lower energy eigenstate to the higher one by absorbing a photon whos energy equals the energy gap:

$$\Delta E^Z_{\mathrm{m_I}} = \hbar\omega_0 \ , \ \ \omega_0 = \gamma B_0 \ . \tag{2.6}$$

ω_0 is called the Larmor frequency. This is the quantum mechanical basis of nuclear magnetic resonance.

Many introductions to NMR continue by saying or at least imply that in a real NMR experiment, where there are a great number of protons, each proton is individually forced into one of its two energy eigenstates. This is wrong, unless the experiment would be conducted at 0 K. In an ensemble of spins placed in an external magnetic field, every individual spin is in a random superposition of the two energy eigenstates and the spins are free to point in arbitrary directions in space, independent of whether the total magnetisation of the spin ensemble is being measured or not [17]. However, as for a classical magnetic moment in an external field, the spins are a bit more likely to point towards the direction of the field, which results in a macroscopic magnetisation M. This static magnetisation can be calculated either classically or by means of quantum mechanics yielding the following formula:

$$M \approx \frac{NI(I+1)\gamma^2\hbar^2}{V 3 k_{\mathrm{B}} T} B_0 = \frac{\chi_0}{\mu_0} B_0 \ . \tag{2.7}$$

Here, μ_0 is the magnetic constant and χ_0 the static susceptibility of the nucleus. The proportionality $\chi_0 \propto 1/T$ is called Curie's Law. Due to the proportionality to γ^2, the static magnetisation of atomic nuclei is smaller than the electron magnetisation by a factor of 10^{-6} and therefore very hard to measure experimentally. For this reason, the nuclear magnetisation has only become interesting for applications due to the discovery of nuclear magnetic resonance.

2.1.2. Bloch Equations and Resonance

The behaviour of a macroscopic magnetisation M in an external field can be calculated based on the considerations for a single spin. Using quantum mechanical tools such as the density matrix and the master equation, one can proof that the following classical equation holds:

$$\frac{d\mathbf{M}(t)}{dt} = \gamma \mathbf{M}(t) \times \mathbf{B} \ . \tag{2.8}$$

This implies that the macroscopic magnetisation essentially behaves like a classical magnetic needle, rotating around its own length direction (therefore having spin or angular momentum) and placed in an external magnetic field. Assuming that the external field points in z-direction $\mathbf{B} = (0, 0, B_0)$, above equation is solved by:

$$M_{\mathrm{x}}(t) = M_{\perp}(0) \sin \omega_0 t, \quad M_{\mathrm{y}}(t) = M_{\perp}(0) \cos \omega_0 t, \quad M_{\mathrm{z}} = M_{\parallel} = \text{konstant} \tag{2.9}$$

The z-component is constant, but the transverse component rotates around the z-axis if its initial value is different from zero. This precessing magnetisation can induce an easily measurable voltage in an electromagnetic coil, which is exactly how the signal in an NMR experiment is acquired. But for this to work, the magnetisation first has to be tilted into the xy-plane. This is achieved by applying an additional, oscillating magnetic field to the sample, which is polarized perpendicular to the z-axis. The effect of such an oscillating field $\mathbf{B}_1(t) = B_1(2\cos\omega_1 t, 0, 0)$ polarized along the x-axis is best understood by splitting it into two components rotating in opposite directions around the z-axis:

$$\mathbf{B}_1^+(t) = B_1 \begin{pmatrix} \cos\omega_1 t \\ \sin\omega_1 t \\ 0 \end{pmatrix}, \quad \mathbf{B}_1^-(t) = B_1 \begin{pmatrix} \cos\omega_1 t \\ -\sin\omega_1 t \\ 0 \end{pmatrix}, \quad \mathbf{B}_1 = \mathbf{B}_1^+ + \mathbf{B}_1^- \ . \tag{2.10}$$

The effect of the $\mathbf{B}_1^-$ component cancels out which will become apparent shortly. Considering just the $\mathbf{B}_1^+$ component and switching to a frame of reference rotating with $\mathbf{B}_1^+$ around the z-axis yields:

$$\frac{d\mathbf{M}'(t)}{dt} = \gamma\mathbf{M}'(t) \times \begin{pmatrix} B_1 \\ 0 \\ B_0 - \frac{\omega_1}{\gamma} \end{pmatrix} = \gamma\mathbf{M}'(t) \times \mathbf{B}_{\text{eff}} \ . \tag{2.11}$$

In the rotating frame, the $\mathbf{B}_1^+$ component of the oscillating field is therefore constant and the magnetisation $\mathbf{M}'$ precesses around the effective field $\mathbf{B}_{\text{eff}}$ analogous to equation 2.8. The $\mathbf{B}_1^-$ component rotates with $2\omega_1$ in this frame of reference, which is why its effect cancels out over time. If the frequency of the applied oscillating field is chosen to be the Larmor frequency $\omega_1 = \omega_0 = B_0\gamma$, only the x' component of the effective field $\mathbf{B}_{\text{eff}}$ remains and the magnetisation will therefore precess around the x'-axis. This is the resonance phenomenon in NMR and the precession is called Rabi oscillation. Because of the typical frequency range in NMR, the oscillating field is often called radiofrequency (RF) field and it is usually created using the same electromagnetic coil that is used for the signal detection. If the RF field is applied just for a short time t, $\mathbf{M}'$ will be tilted by an angle $\alpha = \gamma B_1 t$ (in radian) with respect to the z-axis. Back in the original frame of reference, the magnetisation M will subsequently precess around the z-axis and can induce a voltage in a coil. α is usually called the flip angle (α) and typical values are $90°$ and $180°$. According to this model, the magnetisation would continue precessing infinitely and so would the measured signal. Due to mechanisms that will be explained in Section 2.2, the signal decreases with time in a real NMR experiment. This observation is taken into account in the Bloch equations, first

published by Felix Bloch in 1946 [13]:

$$\frac{dM_{\mathrm{x}}}{dt} = \gamma(\mathbf{M} \times \mathbf{B})_{\mathrm{x}} - \frac{M_{\mathrm{x}}}{T_2^*} \tag{2.12}$$

$$\frac{dM_{\mathrm{y}}}{dt} = \gamma(\mathbf{M} \times \mathbf{B})_{\mathrm{y}} - \frac{M_{\mathrm{y}}}{T_2^*} \tag{2.13}$$

$$\frac{dM_{\mathrm{z}}}{dt} = \gamma(\mathbf{M} \times \mathbf{B})_{\mathrm{z}} - \frac{M_0 - M_{\mathrm{z}}}{T_1} \quad . \tag{2.14}$$

T_1 and T_2^* are called the longitudinal and transverse relaxation times and M_0 is the magnetisation in thermodynamic equilibrium. Instead of the relaxation times, the relaxation rates are often used: $R_1 = \frac{1}{T_1}$ and $R_2^* = \frac{1}{T_2^*}$. The Bloch equations are usually written using T_2 instead of T_2^*, but the measured signal after a simple 90° pulse decays with the time constant T_2^*.

2.1.3. Experimental Setup, FID and Spin Echo

As discussed above, the main components of any NMR experiment are a sample containing atomic nuclei with non-zero nuclear spin, a strong magnetic field to polarize the sample and an RF coil for exciting the sample and detecting the signal created by the precession of the magnetisation. Figure 2.1 shows a schematic setup of such an NMR experiment. The sample is placed inside the coil which is in turn placed inside the magnetic field B_0. The RF field produced by the coil has to be polarised perpendicular to the B_0 field. The RF signal used for excitation is created using a signal generator and amplified before it reaches the coil. Immediately after excitation, the electronic circuit is switched from transmission to receive mode using a fast electronic switch (T/R switch) and the induced voltage is amplified. In order for the analogue signal to be displayed on the computer, it has to be converted into a digital signal. Since the typical signal frequencies in NMR ($B_0 = 1T \Rightarrow f_0 = 42.6\,\mathrm{Mhz}$) are too high for analogue-to-digital converters, the signal first has to be mixed down or demodulated electronically. For applications such as NMR spectroscopy or MRI, an additional set of electromagnetic coils - called shim coils - is used to compensate the inhomogeneities of the B_0 field.

The shape of the signal measured with a simple NMR experiment can be easily calculated using the Bloch equations. After the magnetisation has been tilted into the xy-plane by a

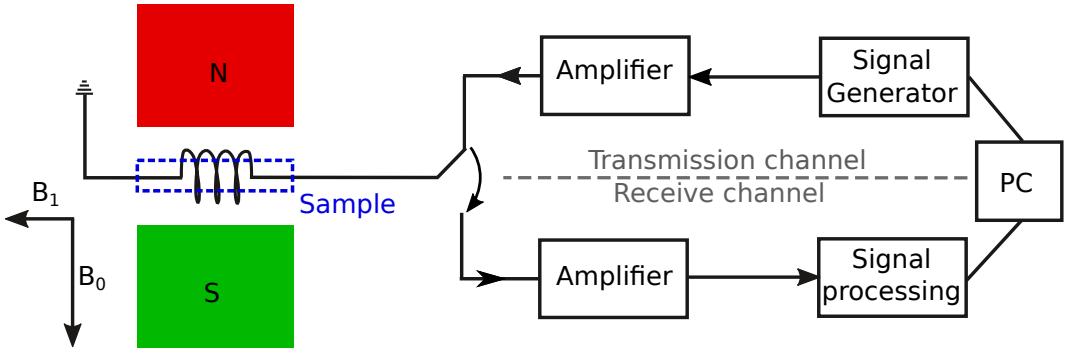

Figure 2.1.: Schematic setup of a basic NMR experiment in transmission mode.

90° pulse, the solution of the Bloch equations for $\mathbf{B}_0 = (0, 0, B_0)$ is:

$$M_{\mathrm{xy}}(t) = M_{\mathrm{x}}(t) + iM_{\mathrm{y}}(t) = M_{\mathrm{xy}}(0)e^{i\omega_0 t}e^{-\frac{t}{T_2^*}} \tag{2.15}$$

$$M_{\mathrm{z}}(t) = M_0(1 - e^{-\frac{t}{T_1}}) \ . \tag{2.16}$$

Complex notation of the transverse magnetisation is used here. This is very common since the NMR signal gets split into a real (M_{x}) and an imaginary (M_{y}) part during signal processing. The longitudinal (z-) component of the magnetisation recovers exponentially with the time constant T_1 until it reaches the (thermodynamic) equilibrium magnetisation M_0. The transverse component rotates around the z-axis which implies that the individual components M_{x} and M_{y} oscillate sinusoidally. Their amplitude decreases exponentially with the time constant T_2^*. This kind of signal is called a free induction decay (FID). The real part of the signal is depicted in Figure 2.2. Performing a Fourier transform of an FID yields the frequency spectrum of the sample. This is the basis for NMR spectroscopy. Different contributions in the spectrum are a result of the different positions of the hydrogen nuclei (protons) within a molecule. Neighbouring atoms slightly change the Larmor frequency of individual protons, a mechanism that is called chemical shift. In addition, neighbouring atoms can also change the relaxation times of the protons, further influencing the form of the NMR spectrum. NMR spectroscopy can therefore be used to elucidate the structures of molecules. Now it becomes apparent why shim coils have to be used in NMR spectroscopy for the compensation of B_0 inhomogeneities. If the field is too inhomogeneous, small differences in Larmor frequencies due to the chemical shift are superimposed by the frequency differences due to the B_0 inhomogeneity, thus decreasing the resolution of the spectrum.

The 90° pulse followed by the acquisition of an FID is the most basic NMR experiment. A

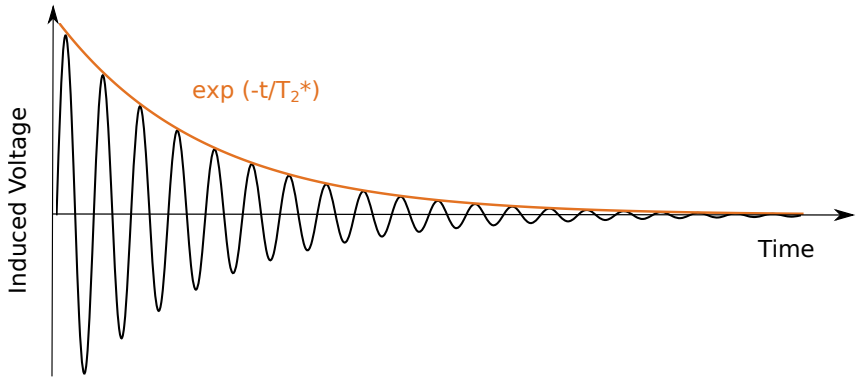

Figure 2.2.: FID (free induction decay) signal with exponential decay $S_0 \cos(\omega_0 t)\exp(-t/T_2^*)$ as measured in a typical NMR experiment.

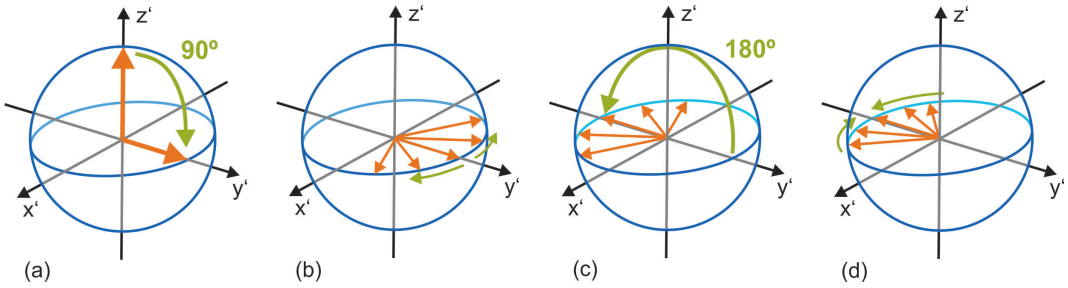

Figure 2.3.: The Hahn spin echo: (a) The 90° pulse tilts the magnetisation into the $x'y'$-plane. (b) The spins dephase due to static field inhomogeneities. (c) At time $T_E/2$ the 180° pulse rotates all spins around the x'-axis. (d) The spins rephase and the signal increases again, forming an echo with its peak at time T_E. Image taken from [19].

second fundamental experiment was developed by Erwin Hahn in 1950 and uses a 90° pulse followed by a 180° pulse, followed by the acquisition ($90° - \frac{T_E}{2} - 180° - \frac{T_E}{2} - AQ$) [18]. It is called a Hahn echo or more commonly a spin echo. Using a spin echo, some of the signal lost during the FID can be recovered. The principle of a spin echo is demonstrated in Figure 2.3. After the initial 90° pulse, the spins start precessing at their individual Larmor frequencies. Due to the spatial inhomogeneities of the B_0 field, the spins precess at slightly different frequencies. In the rotating frame of reference, these differences in precession frequencies appear as a dephasing of the spins. This is the main reason for the rapid decay of the total magnetisation with the time constant T_2^* during an FID. After the signal has vanished, a 180° pulse is applied. This flips all the individual spins around the x'-axis by 180° without changing their phase relation. Assuming that the protons do not change

their position within the inhomogeneous B_0 field, their precession frequencies and therefore their angular velocities in the rotating frame will not change either. This causes the spins to converge again resulting in an increase of the total magnetisation - the spin echo. The 180° pulse in such an experiment is also called the refocussing pulse. The time between the 90° pulse and the peak (center) of the echo is called the echo time T_{E}. However, the assumption that the spins do not move is not correct and in addition, there are other, quantum mechanical processes that lead to loss of phase coherence among the spins. For these reasons, the signal cannot be recovered completely by means of a spin echo experiment. This will be explained in more detail in the next section.

2.2. NMR Relaxation

In this section, the theoretical background and the mechanisms of NMR relaxation will be explained together with experimental techniques for relaxation time determination. The measurement of relaxation times or rates is often called relaxometry. Section 2.3.6 will expand in more detail on relaxometry by means of MRI.

2.2.1. Measuring Relaxation Times

T_1 Time

The T_1 relaxation time is the time constant for the exponential increase in the longitudinal magnetisation (along the axis of the B_0 field) until thermal equilibrium is reached. Since a longitudinal magnetisation does not precess around the z-axis, it cannot be measured directly. Therefore, the magnetisation has to be tilted into the xy-plane in order to determine the absolute value of M_{z}. There are several methods for the determination of the T_1 time of a sample. The most basic one is the inversion recovery technique (IR) with the following pulse sequence:

$$(180^\circ - T_{\mathrm{I}} - 90^\circ - AQ - D)_{\mathrm{n}} \quad . \tag{2.17}$$

After the initial 180° pulse, also called the inversion pulse, the longitudinal magnetisation starts at $-M_0$ and evolves according to the Bloch equations:

$$M_{\mathrm{z}}(t) = M_0(1 - 2e^{-\frac{t}{T_1}}) \quad . \tag{2.18}$$

At a time point T_{I} (inversion time), the whole longitudinal magnetisation is tilted into the xy-plane by a 90° pulse and acquisition of the FID is started immediately. This 90° pulse is called a readout pulse. The height of the FID signal is directly proportional to $M_{\mathrm{z}}(T_{\mathrm{I}})$ and

therefore represents one measurement point on the relaxation curve according to Equation 2.18. After acquisition the magnetisation has to be given enough time to reach thermodynamic equilibrium again - usually $D = 5T_1$ is chosen - until the same sequence is repeated using a different T_I. In this way, the whole relaxation curve can be acquired and the data can be fitted with Equation 2.18 to extract the T_1 time. In order to improve the signal-to-noise ratio (SNR), the integral of the FID can be used instead of its height. This sequence can be combined with the spin echo experiment by adding one or several 180° pulses after the 90° pulse increasing the total acquired signal and therefore the SNR even further.

This method of determining the longitudinal relaxation time is rather slow, mainly due to the long delay time D. A faster method starts every iteration with a rapid series of 90° pulses that effectively cancel out the magnetisation, which is why this technique is called saturation recovery sequence. The 90° pulses are followed by an adjustable waiting period T_I and FID acquisition, which yields one measurement point on the corresponding relaxation curve $M_\mathrm{z}(t) = M_0(1 - e^{-\frac{t}{T_1}})$. Here, a delay time is not necessary and the next iteration can be started immediately. Another fast technique was developed by Look and Locker in 1970 and can be used to determine the T_1 time with a single inversion pulse [20]. The initial 180° pulse is followed by a train of pulses with small flip angles. Each of these pulses reads out part of the current longitudinal magnetisation during its recovery and represents one measurement point on the relaxation curve. Because the readout pulses are applied continuously, the longitudinal magnetisation cannot reach its thermal equilibrium value M_0, but reaches a steady state M_∞ [21]:

$$M(t) = M_\infty - (M_0 + M_\infty)e^{-t/T_1^*}, \quad M_\infty = M_0 \frac{1 - e^{-T_\mathrm{R}/T_1}}{1 - \cos(\alpha)e^{-T_\mathrm{R}/T_1}} \ . \tag{2.19}$$

Here, α is the flip angle of the readout pulses and T_R is the time between them. Since the readout pulses continuously remove longitudinal magnetisation during the relaxation process, the time constant for the relaxation differs from the true T_1 and is called T_1^*:

$$T_1^* = \left\{ \frac{1}{T_1} - \left(\frac{1}{T_\mathrm{R}} \right) \ln\left[\cos(\alpha)\right] \right\}^{-1} \ . \tag{2.20}$$

In theory, T_1 could therefore be directly calculated using the T_1^* extracted by curve fitting. However, no exact value for α can be inserted in the formula, because the flip angle differs within a sample due to inhomogeneities of the RF coil. However, T_1 can be calculated precisely using a three-parameter fit of the relaxation curve as described in [21].

T_2^* and T_2 Times

The T_2^* relaxation time is the time constant for the exponential decay of the FID. It can therefore be determined by simply fitting the amplitude of an FID curve. As described above, the signal loss during an FID resulting from static inhomogeneities of the B_0 field can be recovered by a spin echo experiment. The signal loss due to quantum mechanical relaxation processes cannot be recovered by a spin echo, however, and this contribution is called T_2 relaxation. The T_2^* time is therefore a combination of two processes:

$$\frac{1}{T_2^*} = \frac{1}{T_2} + \frac{1}{T_2'}, \quad R_2^* = R_2 + R_2' \ , \tag{2.21}$$

where T_2' is the contribution due to the B_0 field inhomogeneity. In contrast to T_2^*, the T_2 time only depends on the sample itself making it a very important parameter for sample characterisation. If the diffusion of the spins inside the B_0 field inhomogeneities can be neglected, the height of a spin echo is given by $M_0 e^{-t/T_2}$. By repeatedly acquiring single spin echoes (SE) and varying the echo time, the T_2 relaxation time can therefore be determined with a simple exponential fit of the data. As for the T_1 determination, the integral of the echoes can be used instead of their height in order to improve the SNR. This method is rather slow, because after each echo acquisition, the spin system has to be given a delay time $D = 5T_1$ to return to thermodynamic equilibrium. Another disadvantage is that the diffusion of the spins inside the B_0 field inhomogeneities cannot be neglected for longer echo times. When a spin moves too far, its precession frequency before and after the 180° pulse will be different and the refocussing will not work perfectly, resulting in incorrect T_2 values. This aspect of T_2 relaxation has first been investigated by Henry Torrey in 1953 [22].

In order to minimise the diffusion effects, the CPMG sequence has been developed [23, 24]. The CPMG is a multi-echo spin echo (MESE) sequence and uses a train of refocussing pulses as depicted in Figure 2.4. The time between successive 180° pulses is kept short which prevents the spins from diffusing too far away. Another advantage is that T_2 can be determined much faster, because every echo contributes a separate measurement point to the relaxation curve and there is no need to return to thermodynamic equilibrium. In order to prevent deviations of the 180° pulses to be cumulative in their effect, the phase of the 90° pulse and 180° pulses is shifted by 90°. However, this does not prevent problems arising from stimulated echoes. Because of their T_1 weighting, stimulated echoes can severely corrupt the relaxation curve and the T_2 determination. Stimulated echoes are formed whenever three or more pulses are applied to a spin system and the 90° and 180° pulses are not perfect.

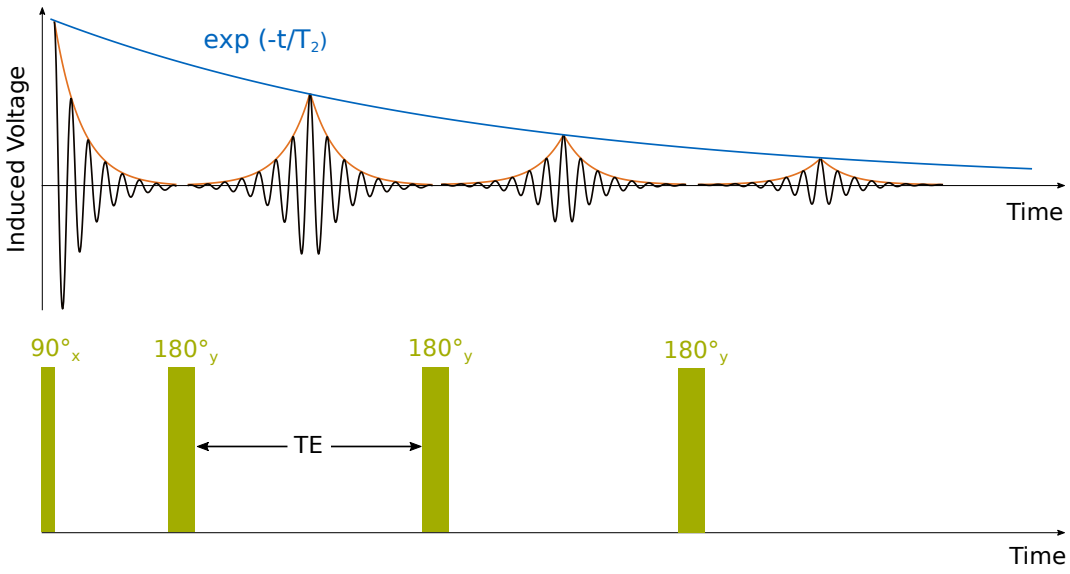

Figure 2.4.: CPMG sequence for T_2 determination: After an initial 90° pulse, a train of 180° pulses is applied in order to minimise diffusion effects and speed up data acquisition. The phase of the 90° and the 180° pulses is shifted by 90° to avoid accumulation of deviations of the 180° pulses.

For example, applying three 90° RF pulses results in three conventional spin echoes (one for every combination of pulses), one secondary spin echo and one stimulated echo. The influence of stimulated echoes can be minimised by using a precise timing of the refocussing pulses and the acquisition windows. In general, the behaviour of a spin system exposed to many RF pulses is very complicated, but it can be understood and simulated using the concept of extended phase graphs [25]. An advantage of the SE approach is therefore the lack of stimulated echoes.

2.2.2. Fitting of Relaxation Curves

In theory, the relaxation times can be extracted from a measurement by simply fitting the data points with the corresponding functions derived from the Bloch equations:

$$\begin{aligned} M(t) &= M_0(1 - 2e^{-t/T_1}) && \text{For IR sequence} \\ M(t) &= M_0 e^{-t/T_2^{(*)}} && \text{For } T_2,\ T_2^* \end{aligned} \tag{2.22}$$

Care should be taken, however, to ensure an appropriate choice of sequence parameters when acquiring the relaxation curves. For this, prior knowledge about the expected relax-

ation times is necessary. The delay times at the end of every IR (for T_1) and SE (for T_2) iteration has to be chosen according to five times the expected T_1 to allow for full recovery of the spin system before the next iteration. In addition, the minimum and maximum inversion time T_{I} and echo time T_{E} as well as their spacing has to be selected according to the expected T_1 and T_2 times as well. If, for example, the T_2 of the sample is considerably shorter than the shortest echo time used for either the SE or the MESE sequences, then the signal of the sample will be mostly gone before the acquisition even starts. If, on the other hand, the T_1 and T_2 times are longer than the longest T_{I} or T_{E}, respectively, the measured signal change will be too small to allow for a precise fit. Another problem arises when too many data points are acquired on the plateau at long T_{I} or T_{E} (M_0 for T_1 and 0 for T_2 or T_2^*). In this case, the fitting algorithm will mainly fit the plateau and not the part of the curve where there is actually a change in the signal, resulting in a high goodness of fit but a possibly inaccurate determination of the relaxation times.

In addition, in a real experiment, noise and sequence imperfections can corrupt the relaxation data, making a more sophisticated fitting approach necessary to get optimal results. For T_1 determination, the main sources of error are imperfections of the inversion pulse and - if spin echoes are used after the readout pulse - the refocussing pulse. If the direction of the magnetisation does not get inverted perfectly, the factor before the exponential function in Equation 2.18 will be smaller than 2. This can be taken into account by choosing this factor as a variable for the fit resulting in a three parameter fit which is the method of choice for most applications [26].

$$M_{\mathrm{z}}(t) = A + Be^{-t/T1} \quad . \tag{2.23}$$

Depending on the type of data acquisition, the FID and spin echo, respectively, will only have positive values. In order to fit the results with Equation 2.23, the part of the relaxation curve before the zero crossing has to be mirrored on the time axis. This can be achieved, for example, by finding the smallest (positive) signal value, inverting all previous data points and discarding the smallest value. In order to avoid losing data, the full complex data should be used and phase-adjusted so that the real part can be fitted according to Equation 2.23.

The main problems when fitting T_2 curves are imperfections of the refocussing pulses, leading to stimulated echoes, and noise. Due to their T_1 weighting, stimulated echoes can prolong the signal decay leading to an overestimation of T_2 values. Since absolute values of the raw data are often used for data evaluation - especially in imaging - the noise distribution of low SNR data follows the Rician distribution instead of the standard zero-mean

Gaussian noise. This can lead to a bias in the T_2 measurement that appears as a baseline offset. T_2^* determination mainly suffers from the same noise issue. Due to T_2^* being usually much shorter than T_2, the SNR of T_2^* data is lower rendering the noise issue even more pronounced. Methods and fitting models for compensating these problems will be described in the imaging chapter (Section 2.3.6), but can basically be applied to NMR experiments as well. In general, the noise statistics issue can be minimised by evaluating the full complex data as was suggested above for T_1 determination.

2.2.3. T_1 and T_2 Relaxation Mechanisms

In order to understand the results of relaxation experiments and use the contrast enhancing properties of magnetic nanoparticles in MRI, the processes leading to the changes in relaxation times have to be understood. In this section, a short review of the general mechanisms leading to transverse and longitudinal relaxation will be given while MNPs will be treated in the next section.

T_1 and T_2 relaxation in NMR is caused by the interaction among the nuclear spins themselves and between the nuclear spins and (para- or ferro-) magnetic substances in the sample. There are several types of interactions, for example scalar and quadrupolar coupling, but by far the most important and usually dominant interaction responsible for relaxation is the magnetic dipole-dipole interaction. Bloembergen, Purcell and Pound published a comprehensive treatment of NMR relaxation due to dipole-dipole interaction in pure substances in 1948; their theory was subsequently called the BPP theory [27]. They treated the dipole-dipole interaction as a quantum mechanical perturbation of the Hamiltonian of the whole spin system and identified six different terms after expanding the interaction potential. These terms correspond to three different types of relaxation mechanisms, which can be understood by considering a single spin being perturbed by the dipolar fields of its (moving) neighbours. The strength of this perturbation can be expressed by the spectral density $J(\omega)$, which is a function of the frequency of the perturbation. Therefore, the greater the spectral density $J(\omega)$, the greater are the relaxation rates ($R = 1/T$).

The first two terms in the interaction potential represent perturbations near zero frequency and therefore depend on $J(0)$. These secular perturbations classically correspond to the change of the z component of the magnetic field at the location of a spin by the z components of the magnetic moments of neighbouring spins. This causes small differences in the Larmor frequencies of the spins which leads to dephasing and decaying transverse

magnetisation. Because there is no net energy change of the spin system, this process only contributes to T_2 relaxation. It is actually similar to the effect of the static B_0 inhomogeneity (equation 2.21), but on a much smaller scale, and is therefore unaffected by refocussing pulses. The remaining four terms in the interaction potential represent perturbations at the Larmor frequency and twice the Larmor frequency and therefore depend on $J(\omega_0)$ and $J(2\omega_0)$. These perturbations correspond to a spin being exposed to RF fields from its moving neighbouring spins, that can induce quantum mechanical energy level transitions. Therefore, these four terms in the interaction potential are able to change the total energy of the spin system by transferring energy to the so called "lattice". Consequently, they contribute to T_1 relaxation, which is also sometimes called the spin-lattice relaxation time. The word "lattice" refers to motional and vibrational degrees of freedom of the atomic nuclei that act as a heat reservoir. The energy level transitions of a spin limit its lifetime in a given state, which is why $J(\omega_0)$ and $J(2\omega_0)$ also contribute to T_2 relaxation.

In order to apply this general theory to a specific substance, the spectral densities have to be calculated. The Wiener-Khinchin theorem states that the spectral density of a stationary random process is given by the Fourier integral of its autocorrelation function $K(\lambda)$:

$$J(\omega) = \int_{-\infty}^{\infty} K(\lambda) e^{2\pi i \omega \lambda} d\tau \ . \tag{2.24}$$

The BPP theory then makes a simplifying assumption for the form of $K(\lambda)$, namely that it decays exponentially with the correlation time τ_c:

$$K(\lambda) = \langle B(t) B(t)^* \rangle e^{-\tau/\tau_c} \ , \tag{2.25}$$

where $B(t)$ is the time depending perturbation. The correlation time τ_c is a very important parameter in relaxation theory, because it is a measure of how fast the perturbations change from the perspective of a spin exposed to the fields created by its neighbouring spins. τ_c can be calculated for a particular substance by considering the diffusion and rotation of spins. Combining Equations 2.24 and 2.25 yields a Lorentz function:

$$J(\omega) \propto \frac{\tau_c}{1 + \omega^2 \tau_c^2} \ . \tag{2.26}$$

For long correlation times or high Larmor frequencies ($\omega_0 \tau_c \gg 1$), $J(\omega_0)$ and $J(2\omega_0)$ and therefore R_1 becomes small. However, the secular perturbation term $J(0)$ contributing to T_2 relaxation will further increase. For small values of τ_c, corresponding to rapid fluctua-

tions of the perturbing fields, all spectral densities including the secular term become small resulting in long relaxation times. For T_2 relaxation, the decreasing secular part can descriptively be explained by averaging out of the field inhomogeneities that cause dephasing. This process is usually called motional averaging or motional narrowing, because it leads to decreased linewidths.

The same theoretical approach can be applied to the relaxation caused by the presence of paramagnetic ions in water. Since the magnetic moment of electrons is larger than the magnetic moment of the ^{1}H core by a factor of about 1000, the relaxation is being dominated by the ion-proton interaction. Again, considering just the dipole-dipole interaction, and assuming a small correlation time ($\omega_0\tau_c \ll 1$), Bloembergen et al. developed a simple formula for the relaxation rates:

$$R_2 \approx R_1 = 12\pi^2\gamma^2\eta N_{\mathrm{ion}}\mu^2/5k_{\mathrm{B}}T \ , \tag{2.27}$$

Here, N_{ion} is the number of ions per cm^3 and μ the magnetic moment of an ion.

2.2.4. $T_2^{(*)}$ Relaxation Due to Magnetic Nanoparticles

Due to their large size compared to paramagnetic ions or protons, magnetic nanoparticles produce slowly varying perturbation fields and therefore usually exhibit a comparatively small influence on the longitudinal relaxation time. For this reason, only their effect on the T_2 time will be discussed here. Magnetic nanoparticles have a huge magnetic moment compared to paramagnetic substances or protons and can therefore dominate transverse relaxation even at small concentrations.

The relaxation mechanism of magnetic nanoparticles depends strongly on their size. This can be understood by considering the diffusion process of protons in the vicinity of an MNP. Assuming that protons cannot penetrate a magnetic particle, Ayant and Freed showed that the correlation time of the diffusion process is given by [28, 29, 30]:

$$\tau_{\mathrm{D}} = \frac{d_{\mathrm{Hyd}}^2}{4D} \ , \tag{2.28}$$

where d_{Hyd} is the hydrodynamic diameter of the MNP and D is the self diffusion coefficient of water. Aggregates of particles or multi-core particles can be treated the same way as single particles using adapted overall hydrodynamic diameters and magnetisations. Due to their size, the correlation time of magnetic nanoparticles is rather long. Therefore, the

secular contribution in the interaction potential dominates over the higher frequency parts in the transverse relaxation process.

For small particles and aggregates that satisfy the motional averaging condition $\Delta\omega_{\mathrm{eq}}\tau_D < 1$, the transverse relaxation rate has been shown to depend quadratically on the particle diameter [31, 32, 33, 34]

$$R_2 = R_2^* = \frac{16}{45} f(\Delta\omega_{\mathrm{eq}})^2 \tau_D \propto {d_{\mathrm{Hyd}}}^2 \ . \tag{2.29}$$

Here, $\Delta\omega_{\mathrm{eq}} = \gamma\frac{\mu_0}{3}M_S$ is the angular frequency shift at the particle surface compared with a point infinitely far away, γ is the gyromagnetic ratio of the proton, μ_0 the vacuum permeability and f the volume fraction of the particles in the sample, which can be converted into the iron concentration. This formula is a result of the quantum mechanical outer sphere theory, which is similar to the BPP theory. As in the BPP theory discussed above, motional averaging means that the dephasing of the water protons due to the presence of the MNPs is averaged out by diffusion. The mechanism of motional averaging becomes less effective with increasing particle size, because the protons are not able to diffuse far enough, which is why the relaxation rates increase. R_2 and R_2^* are equal only if the inhomogeneity of the B_0 field of the MR magnet can be neglected.

If the particles are too big for motional averaging to be significant, the relaxation process can be described by the static dephasing regime (SDR) model, in which the protons are assumed to be motionless. The SDR model was presented by Yablonskiy and Haacke in 1994 [35]:

$$R_2 = R_2^* = \frac{2\pi}{3\sqrt{3}} f \Delta\omega_{\mathrm{eq}} \ . \tag{2.30}$$

According to the SDR model, the relaxation rates only depend on the particle concentration and not on the particle or aggregate size, which allows MNPs in this regime to be quantified by simply measuring the relaxation rate. Particles in this regime also show maximum relaxivity, that is to say, their contrast enhancing properties are optimal. Relaxivity is defined as the relaxation rate divided by the particle concentration in mM (mmol/litre).

For even bigger particles ($\Delta\omega_{\mathrm{eq}}\tau_D \gg 1$), a new mechanism starts taking effect. The magnetic material is distributed among an increasingly small number of MNPs - when comparing the situation to a sample containing smaller particles but with same overall concentra-

tion. Most of the water protons are therefore far away from the next particle, which is why the field fluctuation experienced by them are so slow that refocussing pulses start becoming effective. As a result of that, the R_2 rates drop and also become echo time dependent. This model is called partial refocusing model [36]:

$$R_2 = 2.25\frac{x^{1/3}}{\tau_{\mathrm{D}}}[1.34 + fx]^{5/3} < R_2^* \ , \tag{2.31}$$

where $x = \sqrt{4/5}\gamma\frac{\mu_0}{3}M_S T_{\mathrm{E}}$ and T_{E} is the echo time. The small proportion of protons that are close to an MNP experience such a strong field inhomogeneity that their signal decays too rapidly to be detected. Since R_2^* rates are measured without refocussing pulses, $R_2^* \neq R_2$ even in the absence of external inhomogeneities of the B_0 field. Instead, a measurement of the R_2^* rates will still show the value predicted by the static dephasing model.

2.3. Magnetic Resonance Imaging

After NMR had been developed in 1946, it took 25 years until Paul Lauterbur invented magnetic resonance imaging in 1971. Lauterbur described his discovery in a short paper in 1973, where he showed the first MR image showing two water tubes [37]. Projections of the samples were acquired by rotating the samples inside a magnetic field gradient and the final image was reconstructed using filtered backprojection. Lauterbur was awarded the Nobel Prize in Physiology or Medicine in 2003 together with Peter Mansfield for their discovery and contributions to MRI. MRI has become one of the most important techniques in medical imaging, mainly because of its excellent soft tissue contrast.

This section describes the basics of MRI necessary for understanding the imaging experiments that will be presented in Chapter 5. Compact introductions to MRI can be found in the papers by Hanson [38] or Gossuin et al. [39] and some of their ideas were incorporated in this chapter. For a more comprehensive description, the book by Brown, Cheng, Haacke, Thompson and Venkantesan is recommended [40].

2.3.1. Spatial Encoding

The decisive idea of Paul Lauterbur was to superimpose a linear magnetic field gradient on the homogeneous B_0 field in order to produce a spatial encoding. However, his method of acquiring projections by rotating the sample and reconstructing using filtered backpro-

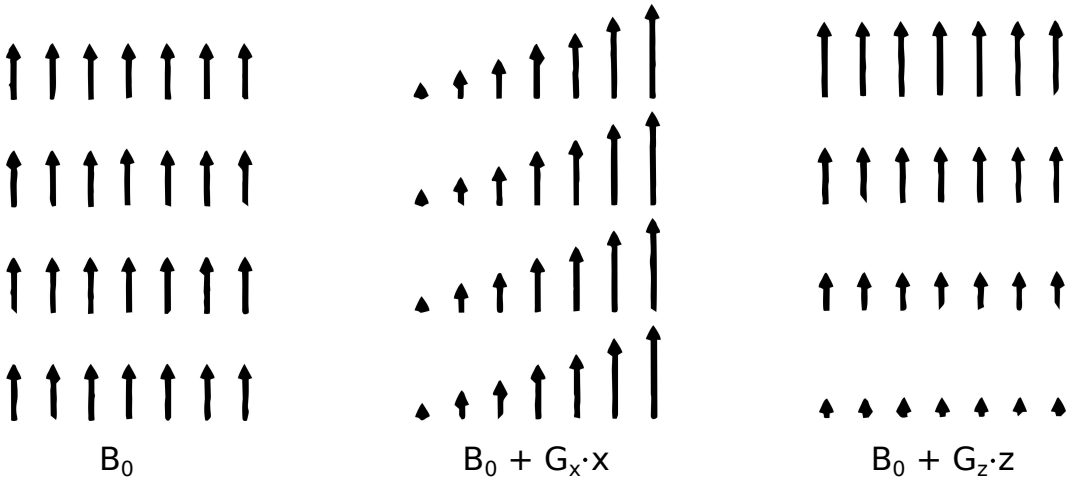

Figure 2.5.: Direction and norm of the main magnetic field. Homogeneous field (left); linear gradient in x-direction (center) and z-direction (right). The scale of the gradients is exaggerated for visualisation - the gradients are much weaker in a real system.

jection is not commonly used any more. Instead, modern MRI scanners use three sets of gradient coils that can produce linear field gradients in all three spatial directions. These gradients cause spatial variations in the norm of the main magnetic field $\mathbf{B} = (0, 0, B_0)$, while preserving its direction along the z-axis. This is illustrated in Figure 2.5 for gradients in x- and z-direction. Since the Larmor frequency of a spin is directly proportional to the main field ($\omega_0 = \gamma B_0$), superimposing a gradients results in a position dependent Larmor frequency:

$$\omega = \gamma(B_0 + G_\mathrm{x}x + G_\mathrm{y}y + G_\mathrm{z}z) = \gamma(B_0 + \mathbf{Gx}) = \omega_0 + \omega_\mathrm{G} \ . \tag{2.32}$$

In this way, contributions to the total signal coming from different locations can be distinguished by their different precession frequencies. Unfortunately, Maxwell's equations do not permit a field gradient so that every position in a three-dimensional volume or even in a two-dimensional plane has its own unique field norm. Applying three linear gradients at the same time will just result in a linear gradient along an arbitrary direction $\mathbf{G}$. Therefore, the gradients have to be applied at different time points in order to get an image.

Slice Selection

A simple way of reducing the number of spatial directions that have to be encoded is slice selection, which is performed by most MRI sequences. Slice selection is achieved by ap-

plying a gradient and an RF excitation pulse with a small bandwidth at the same time. If a gradient in z-direction is applied, for example, the Larmor frequency of the proton spins increases linearly along z. By using an RF pulse at a specific frequency, only spins with an z-coordinate corresponding to the correct resonance frequency get excited. These spins lie in a plane perpendicular to the gradient direction. The frequency spectrum of the RF pulse therefore determines the slice position as well as the slice thickness. Since the frequency spectrum is obtained by taking the Fourier transform of a signal in the time domain, a pulse with a rectangular time function will excite a sinc shaped slice. Conversely, in order to excite a rectangular slice, one has to use an RF pulse with a sinc time function. When slice selection is used during excitation, subsequent pulses such as refocussing pulses should be slice selective as well in order to avoid signal contributions from outside the desired slice.

1D Imaging and Phase Roll

After selectively exciting a slice of the object, a two-dimensional spatial encoding needs to be performed to acquire an image. First, one-dimensional encoding will be explained by considering spins along the x-direction with spin density $\rho(x)$. While applying a gradient along x, the Larmor frequency of those spins is $\omega_0 + \omega_\mathrm{G} = \omega_0 + \gamma G_\mathrm{x} x$. Neglecting relaxation, the total signal acquired from all the spins along x after demodulation (ω_0 is cancelled) is:

$$S(t) = \int \rho(x) e^{-i\omega_\mathrm{G} t} \mathrm{d}x = \int \rho(x) e^{-i\gamma G_\mathrm{x} x t} \mathrm{d}x \ . \tag{2.33}$$

This expression does not take into account the actual size of the magnetization vector as determined by the flux density of the main field B_0 and the temperature nor the process of signal detection by electromagnetic induction in the coil and the electronics. However, these and other factors can be included by replacing the spin density with an effective spin density $\rho_\mathrm{eff}(x)$. The exact expression for $\rho_\mathrm{eff}(x)$ can be found in the literature [40]. Equation 2.33 can be rewritten using $k_\mathrm{x} = \gamma\!\!\!^{-} G_\mathrm{x} t$ in the exponent with $\gamma\!\!\!^{-} = \gamma/2\pi$:

$$S(k_\mathrm{x}) = \int \rho_\mathrm{eff}(x) e^{-i2\pi k_\mathrm{x} x} \mathrm{d}x \ . \tag{2.34}$$

k_x is the spatial frequency along x that is caused by the gradient. The purpose of MRI is essentially to obtain the proton density of the sample. Looking at Equation 2.34, one recognises that the signal is actually the Fourier transform of the proton density. Therefore, the proton density can be obtained by simply taking the inverse Fourier transform of the signal:

$$\rho_\mathrm{eff}(x) = \mathrm{FT}^{-1}[S(k_\mathrm{x})] = \int S(k_\mathrm{x}) e^{i2\pi k_\mathrm{x} x} \mathrm{d}k_\mathrm{x} \ . \tag{2.35}$$

This expression is called the 1D imaging equation and it is the most important equation in MRI. Every spin along x has a slightly different precession frequency during acquisition due to the gradient and by taking the Fourier transform of the total signal, the location of each spin is revealed. This technique is called frequency encoding and most introductions to MRI start this way. In order to encode the second spatial direction, a second gradient G_{y}, perpendicular to the first has to be applied. As mentioned above, applying both gradients at the same time will just result in a single linear gradient with a different direction. The second gradient therefore has to be applied before the first one and before signal acquisition, which is called phase encoding.

There is a slightly different way of interpreting the above equations that facilitates the understanding of phase encoding and also k-space. This approach is based on a publication by Lars Hanson [38], that can be downloaded online: `http://eprints.drcmr.dk/37/1/MRI_English_a4.pdf`. Considering again the spins aligned along the x-direction and assuming that the spin density is constant along x, the situation will look as depicted in Figure 2.6 a. When observed from the rotating frame of reference, the spins all point in the same direction before the application of a gradient. Spins refers here to a small, but still macroscopic magnetisation at a specific location, not the quantum mechanical spin. After a gradient has been applied for a certain time along x, all spins will have rotated by a slightly different angle, which is called the phase roll. When the total magnetisation is measured, the signal will be very small because the different spin directions cancel each other out. However, if the spin density along x is not homogeneous, as it is usually the case for a real sample, the situation is different (see Figure 2.6 b). This time, the total magnetisation measured after the application of the gradient will be much larger than in the first situation, because the phase pattern of the spins matches their spatial distribution. The two situations depicted in Figure 2.6 after application of the gradient correspond to one specific spatial wavelength or spatial frequency k_{x}. By varying k_{x} and measuring the signal, the function $S(k_{\mathrm{x}})$ (see Equation 2.34) is obtained. $S(k_{\mathrm{x}})$ indicates, which phase roll patterns and their corresponding spatial frequencies are similar to the structure of the object that is to be imaged. k_{x} can be varied either by applying a gradient for different periods of time or by applying different gradient strengths for a fixed period of time. Which of the two methods is chosen is essentially irrelevant. The first method is most easily implemented by continuously acquiring the signal while the gradient is switched on (frequency encoding). The second method can be realised by applying a gradient for a fixed amount of time and subsequently acquiring the signal, then applying a different gradient, followed by acquisition again and so on (phase encoding). Having obtained the signal $S(k_{\mathrm{x}})$ of the sample in

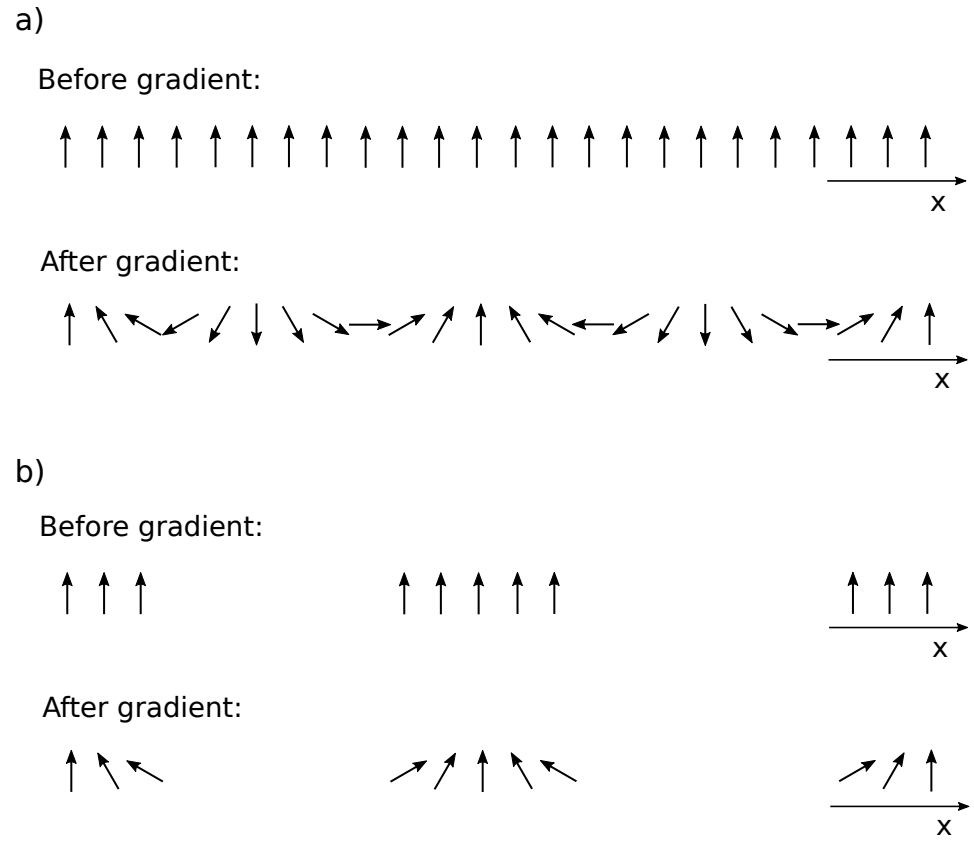

Figure 2.6.: Phase roll pattern before and after the application of a gradient. a) for a homogeneous distribution of spins along x (constant $\rho_{\mathrm{eff}}(x)$); b) non-homogeneous distribution. Adapted from [38].

the spatial frequency domain, the signal in the spatial domain is obtained with a Fourier transform.

Multidimensional Imaging

The concept of explaining MRI using phase roll patterns can be easily extended to two or three dimensions. In Figure 2.7 a, the situation in a slice of spins with homogeneous spin density is shown after gradients in both x- and y-direction have been applied. In this situation, the total magnetisation and therefore the signal will be small, because the spin directions cancel each other out. In analogy to the one-dimensional case, Figure 2.7 b shows the phase roll pattern for an inhomogeneous spin density distribution, where the phase pattern and the structure of the object match. Again, the two situations correspond to one specific spatial frequency. However, the spatial frequency is now a vector: $\mathbf{k} = (k_{\mathrm{x}}, k_{\mathrm{y}})$

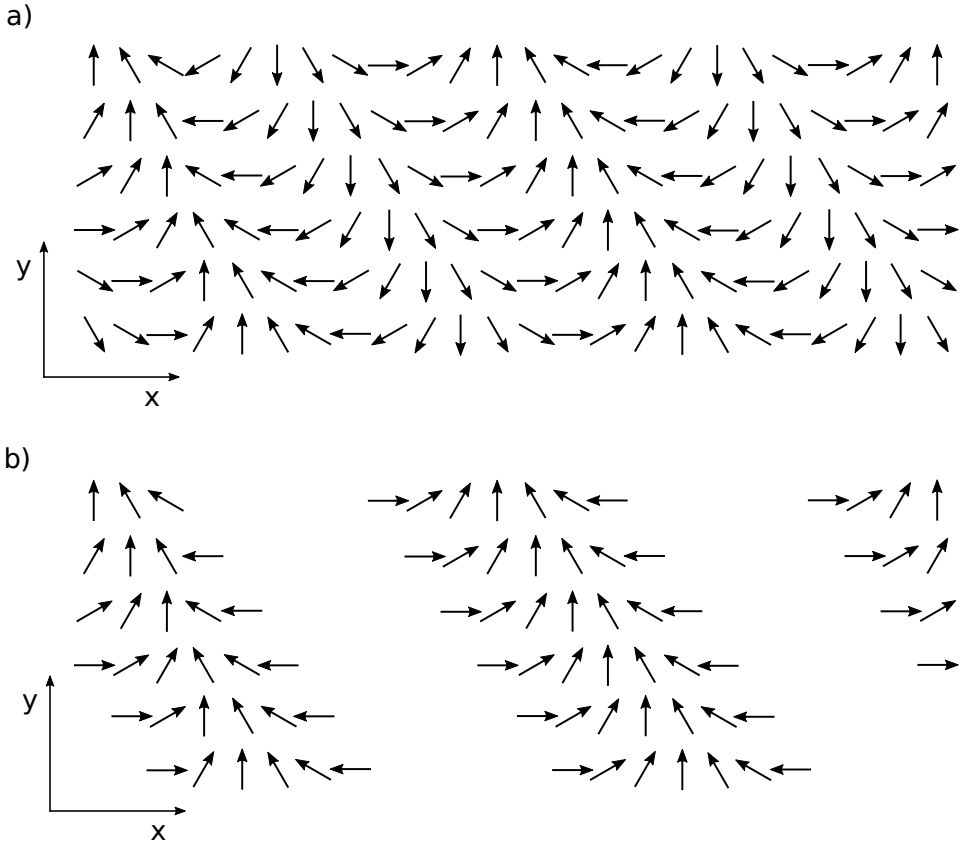

Figure 2.7.: 2D phase roll pattern after the application of two orthogonal gradients G_{x} and G_{y}. a) for a homogeneous distribution of spins (constant $\rho_{\mathrm{eff}}(x, y)$); b) non-homogeneous distribution. Adapted from [38].

and the acquired signal is a function of $\mathbf{k}$:

$$S(k_{\mathrm{x}}, k_{\mathrm{y}}) = \int \rho_{\mathrm{eff}}(x) e^{-i2\pi(k_{\mathrm{x}}x + k_{\mathrm{y}}y)} \mathrm{d}x\mathrm{d}y \ , \tag{2.36}$$

where $k_{\mathrm{x,y}} = \gamma G_{\mathrm{x,y}} t$. In order to check all possible phase roll patterns for similarities with the structure of the object, the norm and the direction of the $\mathbf{k}$-vector have to be varied by varying the gradients G_{x} and G_{y}. The vector space containing the spatial frequency vectors $\mathbf{k}$ is called k-space and the raw data of an MRI scan is depicted by plotting the measured signal intensity as a function of k_{x} and k_{y}. Analogous to the 1D case, the 2D MRI image (i. e. the proton density) is reconstructed by taking the 2D inverse Fourier transform of the

signal:

$$\rho_{\mathrm{eff}}(x,y) = \mathrm{FT}^{-1}[S(k_{\mathrm{x}},k_{\mathrm{y}})] = \int\int S(k_{\mathrm{x}},k_{\mathrm{y}})e^{i2\pi(k_{\mathrm{x}}x+k_{\mathrm{y}}y)}\mathrm{d}k_{\mathrm{x}}\mathrm{d}k_{\mathrm{y}} \quad . \tag{2.37}$$

For practical reasons - digitalisation of the data and time constraints - the signal can only be acquired for a limited number of (k_{x}, k_{y})-pairs and the image reconstruction is performed by a discrete Fourier transform. This is one of the main reasons, why the reconstructed proton density differs significantly from the real proton density. The number of (k_{x}, k_{y})-pairs, that the signal is acquired for is equal to the number of pixels in the reconstructed image. For example, if a 128 x 128 k-space matrix is acquired, the reconstructed image will have 128 x 128 pixels. The k-space matrix is usually centred around the origin of the coordinate system, which corresponds to zero spatial frequency ($k_{\mathrm{x}} = k_{\mathrm{y}} = 0$). The size of a pixel strongly correlates with the level of detail of the image and depends on the maximum k:

$$\Delta x, \Delta y = \frac{1}{2k_{\mathrm{x,y,max}}} = \frac{1}{2\gamma G_{\mathrm{x,y,max}}\Delta t} \quad , \tag{2.38}$$

where Δt is the time period for which the corresponding gradient is switched on. This is a result of the Fourier transform properties, but it is easy to understand considering that large k_{x} and k_{y} correspond to high spatial frequencies which in turn correspond to the fineness of an image. The effect of the k-space matrix size and the maximum k_{x} and k_{y} on the reconstructed image is illustrated in Figure 2.8. If just the very centre of the k-space is used for reconstruction, only the overall signal contrast is visible, but no details can be identified (Figure 2.8 a). The more higher spatial frequencies are used for reconstruction, the more details become visible (Figure 2.8 b and c). On the other hand, if only higher spatial frequencies are used and lower ones are ignored, the reconstructed image shows the fine lines of the details but lacks the overall contrast, because most of the acquired signal is concentrated in the centre of k-space (Figure 2.8 d). In the field of MRI, the size or the number of pixels of the reconstructed image is usually referred to as the "resolution" of the image. However, this "resolution" is not equivalent to what is normally considered the resolution in physics, which is the ability of an imaging modality to differentiate two objects that are close together. In order to calculate this kind of resolution for an MR image, other factors such as relaxation have to be taken into account. Another important consequence of the properties of discrete Fourier transformation is related to the total spatial dimension of the reconstructed image in x- and y-directions, which is called the field of view (FOV):

$$\mathrm{FOV}_{\mathrm{x,y}} = \frac{1}{\Delta k_{\mathrm{x,y}}} \quad . \tag{2.39}$$

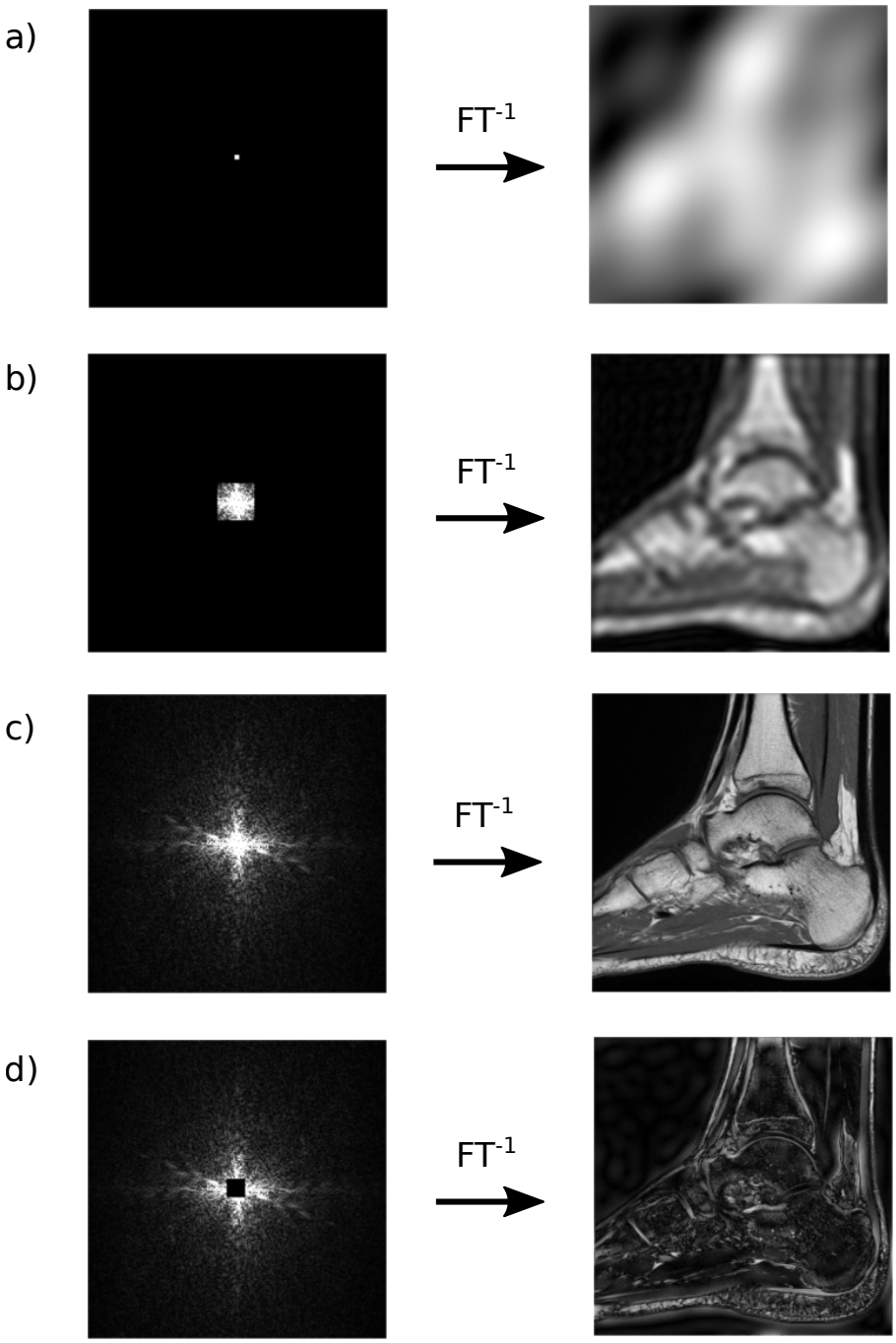

Figure 2.8.: T1-weighted turbo spin echo image of left ankle joint (acquired at "Die Radiologie München", Germany) reconstructed using the following k-space sizes: a) just the central 4 x 4 k-space pixels; b) central 32 x 32 pixels; c) whole 256 x 256 k-space; d) whole k-space without the central 16 x 16 pixels.

The properties of the discrete Fourier transform are crucial for the understanding of most MRI artifacts and this will be discussed in more detail in Section 2.3.5.

2.3.2. Basic Sequences

The last section dealt with how the image in MRI is created by acquiring an NMR signal for different phase roll patterns corresponding to different $\mathbf{k}$-vectors and Fourier transforming $S(\mathbf{k})$. In this section, a short overview will be given about how the k-space matrix is filled in a typical MRI scan. The succession of RF pulses and gradients being switched on and off to acquire $S(\mathbf{k})$ is called a pulse sequence in MRI. Pulse sequences are usually visualised by drawing pulse sequence diagrams consisting of several parallel timelines corresponding to the RF pulses, the gradients and the signal acquisition.

Gradient Echo Sequence

In Figure 2.9, the sequence diagrams of some of the most commonly used MRI pulse sequences are shown together with the corresponding k-spaces. The most basic sequence is the gradient echo sequence (a). First, the magnetisation is tilted by a flip angle α with an RF pulse while at the same time a gradient G_z is applied in z-direction for slice selection. The slice selection gradient also causes the spins inside the slice to dephase during excitation. This dephasing has to be reversed by applying another z-gradient with opposite sign and half of the duration of the previous one (or half the gradient strength) immediately after the RF pulse. The two other gradients in x- and y-direction are also switched on immediately after the RF pulse, which transfers the $\mathbf{k}$-vector to the third quadrant in k-space (black arrow). This quadrant corresponds to tilted phase roll patterns of the spin system like the one depicted in Figure 2.7. For the resulting image, there is no difference between the x and y gradients being applied simultaneously or one after the other. In order to save imaging time though, they are usually applied at the same time. Subsequently, the G_y gradient is switched off and the sign of G_x is reversed moving the $\mathbf{k}$-vector along a horizontal line in k-space. At the same time, signal acquisition is started which results in frequency encoding. For this reason, x is called the frequency encoding direction here whereas y is the phase encoding direction.

The grey dots in the k-space coordinate systems in Figure 2.9 represent the digitalised signal intensities that are saved by the MRI software and used for reconstruction. The dots are intentionally arranged slightly asymmetrically around the k-space centre. This is because an even number of data points are required in every direction for the Fourier transform while

at the same time, the signal also has to be acquired on the k_{x} and k_{y} axes. After one line in k-space has been acquired in this way, the whole procedure is repeated using a different gradient strength or sign for phase encoding. The time between successive RF pulses is called the repetition time T_{R} and can be adjusted by a delay or waiting time after each frequency encoding. If a 90° pulse is used, for example, $T_{\mathrm{R}} \approx 5T_1$ has to be chosen in order to allow full recovery of the magnetisation before the next RF pulse. The number of repetitions is given by the desired number of pixels in phase encoding direction N_{y}. For an image with 128 x 128 pixels, 128 phase steps have to be performed and the total scan time will be 128 x T_{R}. In order to obtain a better signal-to-noise ratio (SNR), the k-space matrix can be acquired more then once and the image is reconstructed from the sum of the k-spaces. If N_{acq} is the number of acquisitions, the total scan time increases by this factor.

While the $\mathbf{k}$-vector is located in the 2nd or 3rd quadrant, the total signal is very small as a result of the (intentional) dephasing due to the gradients. When the $\mathbf{k}$-vector crosses the y-axis, however, the dephasing reaches a minimum (due to $k_{\mathrm{x}} = 0$) and the signal therefore reaches a temporary maximum. This is called a gradient echo. The time between the RF pulse and the center of the gradient echo is called echo time in analogy to the echo time in a spin echo experiment. Since no refocussing pulse is applied, the peak height of the gradient echo signal is proportional to e^{T_{E}/T_2^*}. Echo time and repetition time are chosen depending on the desired contrast, SNR and scan time. For more details on MRI contrast see Section 2.3.3. Using low flip angles and very short repetition times, a 256 x 256 image can be acquired within just a few seconds. This method is called FLASH (Fast Low Angle Shot) and was developed in 1985 [41]. Due to the low flip angle in combination with the repetition time being much shorter than the T_1 time of the object, a steady-state of the magnetisation is reached after a few repetitions. The optimal flip angle (α) for a given T_{R} and T_1 is given by the Ernst angle:

$$\alpha = \arccos\left(e^{-T_{\mathrm{R}}/T_1}\right) \ . \tag{2.40}$$

Spin Echo Sequence

A second basic sequence is the spin echo sequence (see Figure 2.9 b). After a slice selective 90° pulse, the phase and read gradients, G_{y} and G_{x}, are switched on and move the $\mathbf{k}$-vector to the fourth quadrant in k-space. After half of the desired echo time and switching off both gradients, a slice selective 180° refocussing pulse is applied. The slice selection gradient G_{z} for this pulse is not followed by an inverted gradient to account for the dephasing, because

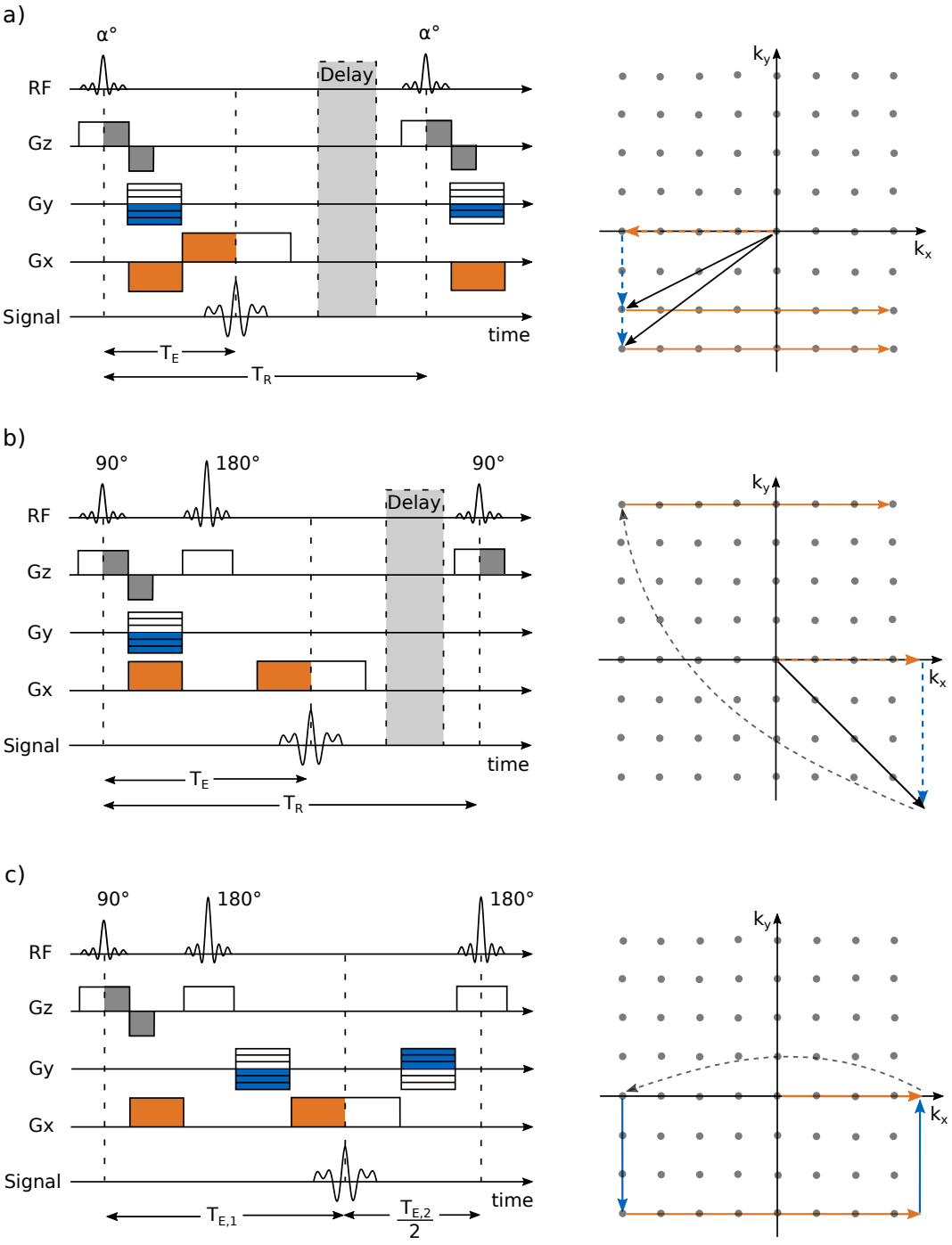

Figure 2.9.: Diagrams for gradient echo (a), spin echo (b) and a modified (multi) spin echo (c) sequences including k-space coverage.

the 180° pulse refocusses this additional dephasing as well. The 180° pulse also inverts the phases of all spins in the slice causing a point reflection of the **k**-vector at the k-space origin. Frequency encoding and data acquisition can start now, without having to invert G_{x}. The frequency encoding has to be timed in such a way that the gradient echo coincides with the spin echo. This timing is important for optimal SNR. The peak height of the acquired signal is thus proportional to e^{T_{E}/T_2}. This procedure is subsequently repeated following a delay time until the whole k-space is covered. As for the gradient echo sequence, this is achieved by varying the strength and the direction of the phase encoding gradient. In order for the magnetisation to return to thermodynamic equilibrium and avoid image artifacts, the delay should be chosen to provide $T_{\mathrm{R}} \approx 5T_1$, which results in very long scan times compared to the FLASH sequence. Dummy scans - repetitions without actually acquiring signal - can be used to ensure that a steady state of the magnetisation is already reached at the beginning of the actual scan, allowing for shorter T_{R}. However, even if dummy scans are performed, the minimum T_{R} will still be longer than for the gradient echo sequence because of the time needed for the refocussing pulse. The main advantage of the spin echo over the gradient echo sequence is the higher signal and the decreased vulnerability to susceptibility artifacts. The echo time can be adjusted by adding delay times before and after the 180° pulse while maintaining the correct timing.

Multi Echo Sequences

The basic spin echo sequence can be modified by using more than one refocussing pulse per repetition. A diagram for such a sequence is shown in Figure 2.9 c. Instead of applying both the read and phase gradients after the slice selective 90° pulse, the phase gradient is applied after the 180° pulse followed by frequency encoding. After acquiring the signal of the spin echo, an inverted phase gradient returns the **k**-vector to its position just before the previous 180° pulse. Subsequently, the next refocussing pulse is applied and the procedure is repeated several times within the same T_{R} before the next repetition is started. The refocussing pulses and spin echoes are separated by the echo time just as in the CPMG sequence in NMR. For every spin echo that is acquired, a different phase encoding gradient can be used and therefore several different lines in k-space can be acquired within the same T_{R}. This approach significantly reduces the required number of repetitions and therefore the scan time. Hennig et al. first described this technique in 1986 and called it RARE (Rapid Acquisition with Refocused Echoes) [42]. Commercial implementations of the RARE sequence are called fast spin (FSE) or turbo spin echo (TSE). The number of k-space lines that can be acquired within one repetition time depends on the T_2 time of the object. A different

approach is to use the same phase encoding gradient for all echoes acquired within the same T_{R}. In this way, the same k-space line is acquired at different echo times. Since the peak height of every spin echo is proportional to e^{T_{E}/T_2}, this can be used for T_2 quantification. This technique is usually called multi-echo spin echo (MESE).

A similar modification can be implemented for the gradient echo sequence and is usually called multi gradient echo (MGE) sequence. Analogous to the spin echo sequence, it can be used to either speed up the acquisition or for T_2^* quantification.

Other Sequences

There exist a great number of other sequences and modifications. For example, multi-slice imaging is commonly used in 2D sequences in order to speed up acquisition. Here, the signals of a number of slices are acquired within the same T_{R} by applying several slice selective RF excitation pulses, each with a different central frequency. Another important class of sequences are 3D sequences that use a broadband RF excitation pulse without a slice selecting gradient. The spatial encoding is then performed using two phase encoding and one frequency encoding gradient. 3D sequences can provide high resolution in all three spatial dimensions without gaps between neighbouring slices or crosstalk. They also deliver a better SNR per voxel compared to a standard, single slice 2D sequence.

2.3.3. Contrast

The main parameter for the quality and usefulness of an MRI image is the contrast-to-noise ratio CNR:

$$\mathrm{CNR} = \frac{\mid S_{\mathrm{A}} - S_{\mathrm{B}} \mid}{\sigma_0} = \mathrm{SNR_A} - \mathrm{SNR_B} \ , \tag{2.41}$$

where S_{A} and S_{B} are the signal intensities of two different structures within the imaged object and σ_0 is the standard deviation of the image noise. In this section, contrast mechanisms will shortly be discussed while the next section will deal with the signal-to-noise ratio.

One of the main advantages of MRI is the broad variety of contrasts - called weightings - that can be achieved. The overall contrast of an MR image is mainly determined by the low spatial frequency components in the center of k-space. When introducing MRI in Section 2.3.1, the contrast of the image was assumed to be entirely caused by spatial variations in proton density and relaxation effects were neglected. If T_1 and T_2 relaxation are taken into

account for the standard spin echo sequence, the signal in a pixel is given by:

$$S(t) \propto \rho_{\text{eff}} \left(1 - e^{-T_{\text{R}}/T_1}\right) \cdot e^{T_{\text{E}}/T_2} \quad . \tag{2.42}$$

According to this equation, mainly three different contrasts can be achieved depending on the choice of T_{R} and T_{E} for a given spatial distribution of T_1 and T_2 relaxation times within the imaged object:

1. $T_{\text{R}} \gg T_1$ and $T_{\text{E}} \ll T_2$: For long T_{R} and short T_{E}, neither longitudinal nor transverse relaxation affect the image contrast and the image is said to be purely proton density (PD) weighted.

2. $T_{\text{R}} \approx T_1$ and $T_{\text{E}} \ll T_2$: For short echo times, the differences in T_2 relaxation times of the distinct structures within the object cause no signal differences. However, if the repetition time is similar to the T_1 values within the object, small differences in T_1 times cause the signals of two separate structures to be different. This type of contrast is therefore sensitive to T_1 differences and the image is said to be T_1 weighted.

3. $T_{\text{R}} \gg T_1$ and $T_{\text{E}} \approx T_2$: If the echo time is of the order of the T_2 values within the object, small differences in the transverse relaxation times of distinct structures result in different signal intensities. The image is therefore said to be T_2 weighted.

The T_1 and PD weightings can also be achieved with a gradient echo sequence by choosing the appropriate parameters. In addition, for long T_{R} and $T_{\text{E}} \approx T_2^*$, a gradient echo image is T_2^* weighted. It should be noted that T_1, T_2 and T_2^* weighted images are also proton density weighted, because the differences in proton densities of distinct structures always cause signal differences, independent of the sequence parameters. In order to obtain a certain weighting, prior knowledge of the range of relaxation times within the object is necessary - which is the case for clinical imaging.

Several other contrasts can be obtained. For example, the magnetisation can be prepared by an inversion or saturation pulse prior to the actual excitation pulse. Moreover, specially designed sequences can provide contrasts such as diffusion or magnetisation transfer.

2.3.4. Signal-to-Noise Ratio

The signal-to-noise ratio is the most important parameter for image quality in MRI next to the contrast. In general, the SNR depends in a complicated manner on hardware and sequence parameters. Hardware parameters include for example the electronic noise and

type of the coil (birdcage, solenoid, surface) as well as the size of the coil compared to the imaged object - the larger the coil the worse the SNR. The SNR also depends strongly on the flux density of the main magnetic field, which is why MRI manufacturers try to build stronger magnets. Up to a flux density of 0.5 T, the SNR increases faster than linear with increasing flux density, but only linear above 0.5 T. Two other factors have to be considered which balance the gain in SNR at higher fields to some extent. First, the longitudinal relaxation time is shorter at lower fields, allowing for shorter T_{R} and therefore more SNR efficient acquisition. Second, susceptibility artifacts are smaller at lower fields and T_2^* is therefore longer, allowing for longer sampling times T_{S}, which in turn results in more SNR efficiency [40].

In practice, the SNR dependence on the sequence parameters is more important, since hardware parameters cannot be easily changed. First of all, longer T_{R} and shorter T_{E} result in better SNR due to longitudinal and transverse relaxation, respectively. In addition, the flip angle should be chosen to optimise SNR depending on T_{R} and T_1 (see Equation 2.40). For a 2D imaging experiment, the dependence of SNR per voxel on the main imaging parameters is given by [40]:

$$(\text{SNR/voxel})\,|_{\mathrm{2D}} \propto \Delta x \Delta y T H \sqrt{N_{\mathrm{acq}} N_{\mathrm{y}} N_{\mathrm{x}} T_{\mathrm{dwell}}}\ . \tag{2.43}$$

Here, TH is the slice thickness and $\Delta x \times \Delta y \times TH$ is therefore the volume of a voxel. The dwell time T_{dwell} is the time between the acquisition of two successive data points in k-space during frequency encoding and $N_{\mathrm{x}} \times T_{\mathrm{dwell}}$ is therefore equal to the sampling time T_{s}. The dwell time is relevant for the SNR because it is the inverse of the bandwidth for the signal readout $T_{\mathrm{dwell}} = \frac{1}{BW_{\mathrm{read}}}$. The larger the readout bandwidth, the more (white) noise is collected during readout.

The effect of the imaging parameters on SNR can be better understood by considering a doubling of the resolution ($\frac{\Delta x}{2}, \frac{\Delta y}{2}, \frac{TH}{2} \Rightarrow \frac{V_{\mathrm{voxel}}}{8}$). Halving the slice thickness results in halving the SNR per voxel and this can only be balanced by using four times as many acquisitions N_{acq} and a fourfold increase in total scan time. Halving Δy while keeping the FOV constant results in a decrease in SNR by a factor of just $\frac{1}{\sqrt{2}}$ because the number of phase encoding steps N_{y} has to be doubled at the same time. However, this also results in a doubling of the scan time and together with the doubling of N_{acq} to balance the drop in SNR, it results in a fourfold increase in scan time as well. Finally, halving of Δx while keeping the FOV constant also results in a decrease in SNR of $\frac{1}{\sqrt{2}}$, because N_{x} has to be

doubled. The doubling of N_{x} can be achieved without further increase in scan time. In order to balance the drop in SNR, the number of acquisitions has to be doubled which doubles the scan time. However, increasing N_{x} and therefore the sampling time can only be performed as long as $T_{\mathrm{s}} \ll T_2^*$. In summary, doubling the resolution in all three spatial dimensions results in a drastic decrease in SNR which can only be balanced by a 32- or 64-fold increase in total scan time - depending on the T_{s}/T_2^* ratio. This is the reason why MRI is so time consuming and the resolution for standard clinical applications is worse than for other imaging modalities such as CT.

2.3.5. Standard Artifacts

There are a great number of different artifacts in MRI that can distort the image and lead to misinterpretations. Some of the most common artifacts will be shortly reviewed here. Figure 2.10 a shows a round water sample and the so called Gibbs ringing artifact (left image). Gibbs ringing appears as parallel lines next to sharp transitions in signal intensities from one structure to another and can occur for all pulse sequences. It is a result of the limited extension of the k-space matrix together with the discrete Fourier transform for image reconstruction. Gibbs ringing can be reduced by using higher image resolution or image filtering. A second very common artifact is aliasing. It appears as a wrap around of the imaged object in phase encoding direction (see Figure 2.5 b, left). The aliasing artifact occurs when the spatial extension of the object is larger than the FOV as given by $\mathrm{FOV}_{\mathrm{y}} = \frac{1}{\Delta k_{\mathrm{y}}}$. In principal, it could appear in both phase and frequency encoding direction, but it can be avoided in frequency direction by using a bandpass filter during acquisition. In phase encoding direction, aliasing can only be avoided by choosing a larger FOV. The image in Figure 2.10 b to the right was acquired by swapping the phase and frequency encoding directions. A third artifact appears as stripes of noise in phase encoding direction (Figure 2.10 c) and is called zipper artifact. It is usually caused by RF interference resulting from electronic devices in the scanner room or bad RF shielding.

Another important type of artifacts is caused by susceptibility differences either within or at the edge of the object. Susceptibility artifacts are most prominent in gradient echo sequences with strong T_2^* weighting, but can also appear in spin echo images. They usually result in a strong signal extinction around the origin of the susceptibility inhomogeneity. If the susceptibility difference is very high, they can also cause a spatial distortion as seen in Figure 2.10. A strong susceptibility difference can occur when a metallic object is present or at air-water or air-tissue interfaces. Susceptibility artifacts get worse for higher main

fields and longer echo times. They can be reduced by using short echo times, spin echos and stronger imaging gradients, but in general, susceptibility artifacts depend in a rather complicated way on the sequence parameters (see [43] for more details).

Other common artifacts include ghosting due to patient motion and breathing (see Figure 2.10 e) as well as spatial distortions due to eddy currents caused by the rapid switching of the gradient coils. In Section 5.3.3, some more artifacts will be discussed that appeared during the course of this PhD.

2.3.6. Relaxometry

MRI relaxometry refers to the measurement of the NMR relaxation times T_1, T_2 and T_2^* by acquiring quantitative images (called maps) using MRI. In general, the approach is very similar to the measurement of relaxation times without imaging as described in Section 2.2. However, there are several complications that make MRI relaxometry more challenging.

T_1 Mapping

T_1 mapping can most easily be performed with the inversion recovery method by simply adding a slice selective 180° inversion pulse and an adjustable waiting period before the excitation pulse of a gradient or a spin echo sequence. The inversion time is given by the time between the inversion pulse and the excitation pulse. The signal of every k-space line is therefore proportional to the longitudinal magnetisation at time point T_1. In order to quantify the T_1 time, this IR sequence has to be repeated for different inversion times. This method is very time consuming because the repetition time of the sequence has to be approximately five times the expected T_1 time to allow for a fully recovered longitudinal magnetisation before the acquisition of every k-space line. In order to speed up the image acquisition, a multi echo sequence can be used for the readout of the longitudinal magnetisation. Another way to acquire T_1 maps quickly is to use an imaging version of the method developed by Look and Locker in 1970 described in Section 2.2. After an initial inversion pulse, the longitudinal magnetisation is read out using a train of short excitation pulses, each used to fill one line in k-space. This method was first described by Deichmann and Haase in 1992 [21]. Due to the spatial profile of the slice selection applied during the inversion pulse and all the following pulses, the problem with inaccurate flip angles is more pronounced for T_1 mapping than for the NMR T_1 quantification methods.

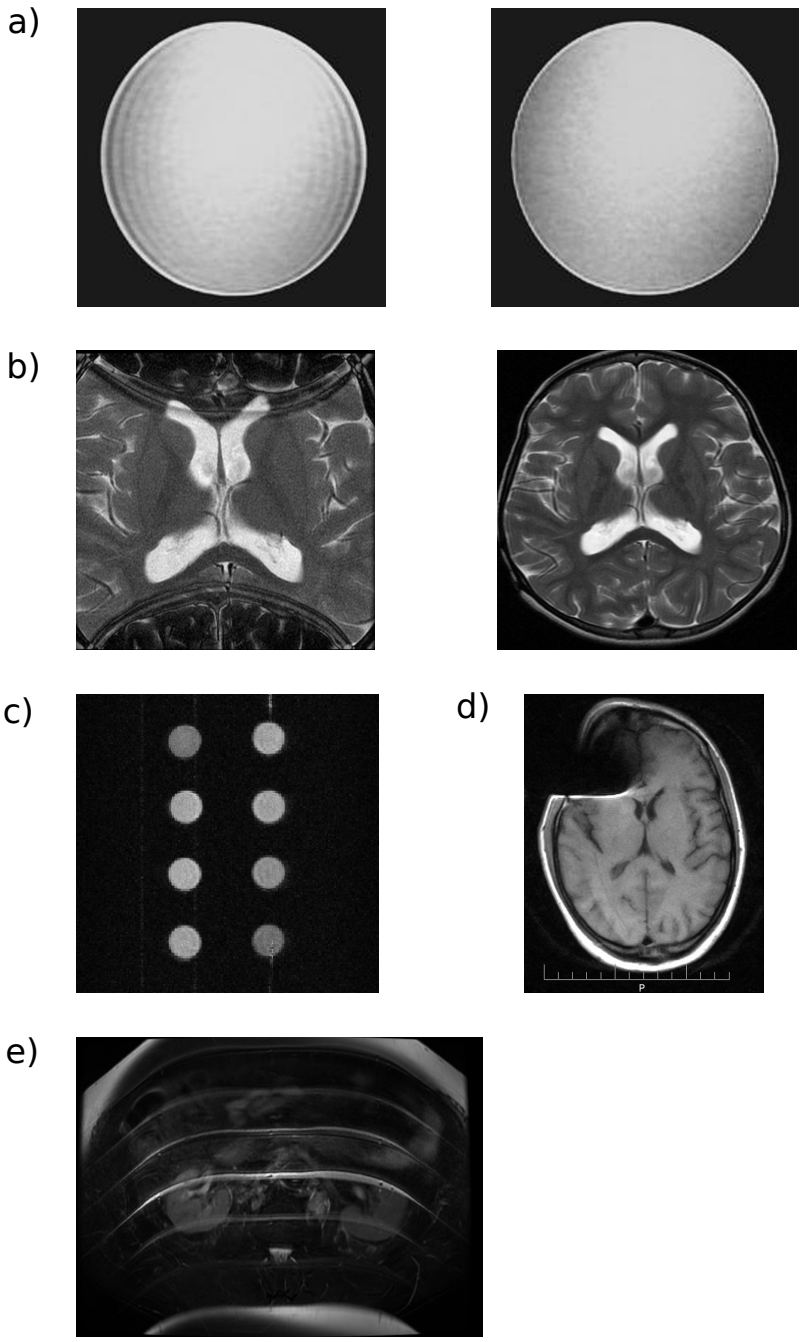

Figure 2.10.: a) Gibbs ringing artifact. Case courtesy of Dr J. Ray Ballinger, Radiopedia.org. From the case rID: 22133. b) Wrap-around due to aliasing artifact. Case courtesy of Dr Usman Bashir, Radiopedia.org. From the case rID: 16491. c) Vertical zipper artifact. d) Susceptibility artifact caused by a metallic substance in the scalp of the patient. Case courtesy of Dr Ayush Goel, Radiopedia.org. From the case rID: 22731. e) Ghosting due to motion artifact. Case courtesy of Dr Roberto Schubert. Radiopedia.org. From the case rID: 17928.

T_2 and T_2^* Mapping

T_2^* mapping is conceptually the simplest MRI relaxometry method. It just requires images being acquired with a standard gradient echo sequence using different echo times. In order to decrease the total scan time, a multi-echo gradient echo sequence (MGE) can be used. Each echo is used to fill a line in a different k-space. Using a train of eight echoes, for example, eight different images with decreasing signal are obtained.

T_2 mapping is conceptually simple as well, but much more problematic in practice. A T_2 map can either be acquired by repeating a single spin echo sequence with different echo times or by using a multi-echo spin echo sequence, in which every echo is used to fill a different k-space. In both cases, the repetition time should be chosen long enough to allow a full recovery of the magnetisation before the next excitation pulse. The disadvantage of the single echo version next to the longer scan time is the influence of diffusion. Due to the imaging gradients, the diffusion effect is stronger than for the NMR spin echo sequence. The diffusion effects and the scan time are reduced with the multi-echo method. Instead, the MESE sequence suffers from stimulated echoes [44], which are more problematic in imaging than in NMR. First, stimulated echoes cannot be avoided so easily by precise timing, because the imaging gradients can shift the echo formation in time. Second, the spatial profile of the slice selection performed together with the refocussing pulses results in even more inaccurate flip angles. One approach to minimise this effect is to use thicker slices. There is no consensus among researchers, whether the single or the multi-echo spin echo sequence should be considered the "gold standard" for T_2 mapping.

Another problem concerning T_2 and T_2^* mapping sequences is the minimal echo time. Due to the slice selection and the imaging gradients, the minimal echo times are considerably longer in imaging, which makes the T_2 and T_2^* quantification for fast relaxing samples difficult.

Fitting of Relaxation Maps

After acquiring images with different inversion times or echo times, respectively, the images are evaluated voxel by voxel to obtain the map. In general, the fitting procedures used for NMR relaxation curves is now used for every voxel (see Section 2.2.2). Again, in order to achieve a reliable fit, the sequence parameters such as minimum and maximum echo times have to be chose appropriately. However, this is more difficult in imaging, because there might be a broad range of different relaxation times within the imaged object.

The problems regarding the fitting procedures are the same as for the NMR relaxation curves, but they are more pronounced due to less SNR, more inaccurate flip angles and the presence of the gradients. The three parameter fit remains the standard method for fitting T_1 relaxation curves, while numerous methods have been published to account for the errors in T_2 and T_2^* fitting. Several fitting models have been proposed to correct for the problem of Rician noise in low SNR magnitude images [45, 46, 47, 48, 49]

$$S(T_{\mathrm{E}}) = Ae^{-T_{\mathrm{E}}/T_2^{(*)}} \tag{2.44}$$

$$S(T_{\mathrm{E}}) = Ae^{-T_{\mathrm{E}}/T_2^{(*)}} + B \tag{2.45}$$

$$S(T_{\mathrm{E}}) = \left[\left(Ae^{-T_{\mathrm{E}}/T_2^{(*)}}\right)^2 + B^2\right]^{1/2} \tag{2.46}$$

$$[S(T_{\mathrm{E}})]^2 = \left(Ae^{-T_{\mathrm{E}}/T_2^{(*)}}\right)^2 + B^2 \tag{2.47}$$

Another way of dealing with low SNR images is to discard all data points that are below a certain signal threshold and fitting with Equation 2.44. As mentioned in Section 2.2.2, the problem with noise statistics can be avoided by using the full complex data. Several groups have also published more sophisticated fitting or post-processing procedures to compensate for the effect of stimulated echoes [50, 51, 52, 53].

2.4. Superparamagnetism

Superparamagnetism was first described by W. C. Elmore in 1938 [54]. Elmore discovered that colloidal suspensions of magnetite and maghemite exhibit a magnetisation curve like a paramagnet (Langevin function), but with a much higher magnetic susceptibility, which is why this phenomenon was later called superparamagnetism [55]. The absence of magnetic remanence was surprising, since magnetite and maghemite are ferrimagnetic and should therefore show hysteresis. The reason for the lack of remanence is the small size of superparamagnetic particles. Below a certain size, ferro- and ferrimagnetic particles consist of just a single magnetic domain [56, 57]. While the quantum mechanical exchange interaction among the electrons of such a particle remains unchanged, two relaxation mechanism lead to the particle's total magnetisation direction to flip so rapidly, that the time average is zero.

The first relaxation mechanism is called Néel relaxation [58]. Due to thermal fluctuations,

the magnetic moment of a particle can overcome the energy barrier given by the anisotropic energy $E_{\mathrm{B}} = KV$ and flip between the directions of the easy axes. The characteristic time for the flipping process is given by the Néel time [58, 59]:

$$\tau_{\mathrm{N}} = \tau_0 \exp\left(\frac{KV}{k_{\mathrm{B}}T}\right) \quad , \tag{2.48}$$

where τ_0 is of the order of $10^{-13} - 10^{-9}$ s, K is the magnetic anisotropy constant, V the particle volume, k_B Boltzmann's constant and T the absolute temperature. If the measurement time is much longer than the τ_{N}, the time average of the magnetisation will be zero. If, however, the measurement time is much shorter than the Néel time, the magnetisation of the particle will appear to be blocked. For a given measurment time and temperature, the state of the particle - superparamagnetic or blocked - depends exponentially on the volume V according to Equation 2.48. Therefore, there exists a material dependent, but sharp size limit for magnetic nanoparticles below which they become superparamagnetic. For most materials, this limit is between 5 and 30nm (diameter). The second relaxation mechanism is called Brown relaxation. It is caused by the Brownian rotation of magnetic particles when they are suspended in a fluid with viscosity η. The formula for the corresponding relaxation time was originally developed by Peter Debye and states [60]:

$$\tau_{\mathrm{B}} = \frac{3V\eta}{k_{\mathrm{B}}T} \tag{2.49}$$

Equations 2.48 and 2.49 are based on the assumption of no externally applied magnetic field and have to be adjusted if such a field is applied to the MNP sample. Qualitatively, however, the relaxation mechanisms will counteract the particle's alignment with the external field, which is why the thermodynamic expectation value of the total magnetisation of an MNP sample has to be calculated using the Maxwell–Boltzmann statistics. If the anisotropy energy is small compared to the Zeeman energy, the magnetisation curve of MNPs can be described by the Langevin function:

$$\langle M(B) \rangle \approx n\mu L\left(\frac{\mu B}{k_{\mathrm{B}}T}\right) \quad , \quad L(x) = \coth(x) - \frac{1}{x} \quad , \tag{2.50}$$

where n is the density of nanoparticles in the sample. Due to the high magnetic moment μ of MNPs, their magnetisation curve saturates very quickly compared to paramagnetic substances. The high susceptibility combined with the absence of remanence make superparamagnetic nanoparticles very interesting for medical applications. Without an applied field, they do not aggregate as quickly as ferromagnetic particles, but at the same time they

can be easily magnetised when necessary, for example for drug targeting.

2.5. Mössbauer Spectroscopy

The Mössbauer effect is the recoil-free emission and absorption of gamma radiation by an atomic nucleus and was discovered by Rudolf Mössbauer in 1958 [61]. It is the basis for Mössbauer spectroscopy, a very sensitive spectroscopic method that detects tiny changes in the energy levels of an atomic nucleus due to its chemical environment and can be used to analyse the composition of iron-containing samples such as magnetic iron oxide nanoparticles. Mössbauer spectroscopy can only be performed on solid samples, since the Brownian motion of the atoms would otherwise lead to strongly broadened resonance lines. In order to obtain iron spectra, a radioactive gamma-ray source such as ^{57}Co in rhodium is usually used. The absorption lines of the sample are subsequently scanned by moving the source back and forth on an electromechanical velocity drive, thereby exploiting the Doppler effect. The main interactions that give rise to the changes in the energy levels and therefore the Mössbauer spectra of iron nuclei are the magnetic hyperfine (Zeeman) splitting, the isomeric shift and the quadrupole splitting.

The hyperfine splitting is caused by the interaction between the atomic nucleus and a magnetic field either produced by the electrons or applied externally. Due to the quantum mechanical selection rules, six transition between the ground state and the excited state of the iron nucleus are allowed, which results in the typical sextet spectrum. The quadrupole splitting is a result of the interaction between the electric field gradient produced by the electrons and a nucleus in a state with non-spherical charge distribution (for nuclear spin $I > 1/2$). In iron spectra, the quadrupole interaction shifts the positions of the six hyperfine lines. The isomeric shift is caused by the interaction of the s-electrons - whose density at the location of the nucleus depends on the chemical environment - and the electrostatic potential of the nucleus, which depends on the state of the nucleus.

For bulk material, the Mössbauer spectra of iron containing samples show well resolved, sharp sextets and can therefore be analysed quite easily. For iron oxide nanoparticles, however, the spectra can be severely broadened due to their superparamagnetic relaxation. A particle with unaxial magnetic anisotropy changes the direction of its magnetisation with the Néel relaxation time τ_{N} (see Equation 2.48). Due to the exponential function, the Néel time strongly affects the temperature and particle size dependence of Mössbauer spectra [62, 63, 64]. For Néel relaxation times that are much shorter than the timescale of Möss-

bauer spectroscopy ($\approx 10^{-9}$ s), the magnetisation of the nanoparticles flips so quickly, that the atomic nuclei, on average, do not experience a magnetic field. Therefore, the magnetic hyperfine splitting vanishes and the spectra just exhibit the sharp pattern of a paramagnetic material [65, 66]. For particles with a Néel relaxation time of the order of $\approx 10^{-9}$ s, the iron sextets are still identifiable, but severely broadened. The exact shape of the Mössbauer spectra in the transition region can be calculated [67].

When superparamagnetic nanoparticles are placed in a strong external magnetic field, their (electron) magnetic moments stop flipping and align with the field. For Mössbauer spectroscopy performed in the presence of an external field, this means that the hyperfine splitting is proportional to the total magnetic field at the location of the nucleus

$$\mathbf{B}_{\mathrm{tot}} = \mathbf{B}_{\mathrm{ind}} + \mathbf{B}_{\mathrm{app}} \ , \tag{2.51}$$

where $\mathbf{B}_{\mathrm{ind}}$ is the induced hyperfine field of the electrons at the atomic nucleus [63]. Above the blocking temperature, the induced field is approximately given by the Langevin function:

$$\mathbf{B}_{\mathrm{ind}} = \mathbf{B}_0 L\left(\frac{M_{\mathrm{S}} V B_{\mathrm{app}}}{k_{\mathrm{B}} T}\right) \ , \tag{2.52}$$

where $\mathbf{B}_0$ is the hyperfine field for slow superparamagnetic relaxation and M_S is the saturation magnetisation of the magnetic particle. The relative intensities of the six lines in the Mössbauer spectrum of iron depend on the angle θ between the total magnetic field at the nucleus and the propagation direction of the gamma rays [63]. If the sample is magnetised perpendicular to the gamma ray direction, for example, the area ratio of the six lines in the Mössbauer spectrum is $3:4:1:1:4:3$. In general, the relative areas are given by $3:x:1:1:x:3$ with

$$x = \frac{4\sin^2\theta}{2-\sin^2\theta} \ . \tag{2.53}$$

2.6. Magnetic Particle Imaging and Spectroscopy (MPI & MPS)

Magnetic particle imaging was introduced in 2005 by Gleich and Weizenecker [68] as a method to directly visualise superparamagnetic nanoparticles. Inside the MPI scanner, MNPs are typically exposed to two different magnetic fields. The first one, called drive field, is an oscillating field created by two opposing set of coils for each spatial direction and induces a non-sinusoidal oscillation of the magnetisation of the particles. This is only

possible for superparamagnetic particles, that have a non-linear magnetisation curve without remanence. The oscillation of the particle magnetisation is picked up by a receive coil and Fourier transformed. Due to the non-linearity of the M(H) curve, the Fourier spectrum shows contributions from higher harmonics that are characteristic of the particles. The second magnetic field, called selection field, is a static magnetic gradient field produced by a pair of coils. This field can magnetically saturate particles, so that their response to an oscillating field will be suppressed, because their magnetisation is at the plateau of their M(H) curve. By superimposing both fields, a field free point can be created that moves quickly through the imaged object. Particles that are outside of the field free region do not contribute to the Fourier spectrum, because they are saturated. Only those particles inside the field free region contribute and therefore the object is scanned by the field free point. In order to reconstruct an image from the obtained spectra during the movement of the field free point, a calibration has to be performed before the actual scan. For this purpose, a small particle sample containing the same MNPs that will be used for the actual scan is successively placed at every spatial position of the desired voxel grid and the corresponding frequency spectrum is measured. In this way, the reconstruction algorithm can deduce the spatial distribution of the MNPs in the object. This is called frequency-based reconstruction [69]. Other methods for reconstruction have been developed, for example X-Space MPI [70]. Since MPI only detects MNPs, it has to be combined with an anatomical imaging method such as CT or MRI for clinical applications [71]. In theory, MPI is a quantitative method, meaning that the signal response is proportional to the particle concentration. In practice however, the response depends on many parameters and is not always exactly proportional to the concentration.

MPI scans are rather effortful due to the experimental requirements and also time consuming as a result of the typically performed calibration. Magnetic particle spectroscopy measures the non-linear magnetic response of MNPs exposed to an oscillating magnetic field - like MPI, but without spatial encoding. MPS can be used to test the MPI performance of MNPs within a very short time [72]. Additionally, it is a very sensitive method for the characterisation of magnetic nanoparticles capable of quantifying particles and also able to reveal their size distribution and magnetic interactions, for example in aggregates [73, 74]. While the third harmonic A_3 of the frequency spectrum is usually used for particle quantification, the harmonic ratio A_5/A_3 can be used to assess the particle interactions.

2.7. Magnetometry

MPS and MPI detect the dynamic response of the MNP magnetisation when subjected to an oscillating external magnetic field. Another important method for MNP characterisation is to measure the M(H) curve, which represents the (quasi-)static response to an external field. An M(H) curve is typically obtained by placing a small sample inside a strong electromagnet that magnetises the particles. The magnetisation of the sample is then measured for different flux densities using a vibrating sample magnetometer (VSM). For this, the sample can be sinusoidally vibrated next to a SQUID, which measures the magnetic field created by the sample's magnetic moment.

The M(H) curve can provide a range of information about the properties of a sample. First, the overall shape of the curve can be used to tell whether the sample consists of paramagnetic, ferro-/ferrimagnetic or superparamagnetic particles. Second, if sufficiently high magnetic fields are available, the saturation magnetisation can be measured - independent of any interactions among the particles, since at high fields, all magnetic momenta are aligned with the external field. For this, the sample has to be given enough time at every externally applied flux density for the larger particles to fully align with the field - otherwise, the saturation magnetisation would depend on the measurement time. At lower fields, the size of the particles and their interactions among themselves determine the exact shape of the curve [75]. By fitting the M(H) curve data points to an integral over the size distribution and the Langevin function, the mean diameter and the standard deviation of the size distribution can be extracted [76].

3. Characterisation of MNPs Using Mössbauer Spectroscopy at Ambient Temperature

This chapter is based on the paper "'Characterisation of iron oxide nanoparticles by Mössbauer spectroscopy at ambient temperature"', published in 2016 in the Journal of Magnetism and Magnetic Materials [10]. Besides writing the major part of this publication, I have simulated the magnetic field of the Halbach array and contributed substantially to the planning of the Mössbauer measurements and to the discussion of the experimental results.

The publication describes a new method for obtaining sufficient hyperfine splitting in the Mössbauer spectra of magnetic nanoparticles with diameters less than 15 nm. This allows the distinction of the two most important types of iron oxides at room temperature.

3.1. Introduction

Magnetic nanoparticles are usually made of iron oxides, the most common iron oxide types used for particle synthesis are magnetite ($\mathrm{Fe_3O_4}$) and maghemite ($\gamma - \mathrm{Fe_2O_3}$). Because of its higher magnetisation (92 $\mathrm{Am^2\,kg^{-1}}$) magnetite is preferred to maghemite for many applications [77]. However, maghemite can be formed from magnetite through aging or oxidation, respectively. As a result of the different hyperfine patterns of the iron oxides, magnetite and maghemite can be distinguished using Mössbauer spectroscopy and their respective amounts can be determined. Therefore, Mössbauer spectroscopy enables the characterisation of iron oxides with respect to their manufacturing and ageing processes.

Magnetite and maghemite both have a spinel structure and show a strong hyperfine splitting even at ambient temperature because of their ferrimagnetic order [78]. In maghemite, the Mössbauer parameters of Fe(III) on the tetrahedral (A) and octahedral (B) sites are very similar and hardly distinguishable in the Mössbauer spectra [79]. Magnetite spectra, how-

ever, consist of two separate sextets, one belonging to the Fe(III) on the tetrahedral sites and one belonging to the mixed-valence Fe(2.5) on the octahedral sites [80, 81, 82]. The octahedral sites of magnetite are occupied by equal amounts of Fe(II) and Fe(III) and above the Verwey transition temperature ($T_{\mathrm{V}} = 119\,\mathrm{K}$, [83]), electron hopping between the different ions occurs. This leads to an effective mixed-valence state Fe(2.5), which is why the B-sites only yield one magnetically split sextet. This sextet has a smaller hyperfine field than the Fe(III) on the A-sites and an isomer shift intermediate between that of Fe(III) and Fe(II). Therefore, the sextets belonging to the A- and B-sites in magnetite can be distinguished. For pure magnetite, the relative amount of the A- and the B-components is 1:2. Below the Verwey transition temperature, the electrons on the B-sites become localised, which facilitates a distinction of the Fe(II) and Fe(III) lattice sites [84, 85].

Due to the additional sextet for the B-sites, bulk magnetite can therefore be distinguished from maghemite using Mössbauer spectroscopy rather easily [86, 87]. For a mixture of magnetite and maghemite or for partially oxidised magnetite, the Mössbauer parameters stay essentially the same and only the relative intensities of the sextets change. By fitting such spectra, one can determine the relative amounts of magnetite and maghemite or the degree of oxidation of magnetite at room temperature. Unfortunately, this is not generally true for iron oxide nanoparticles, for which the magnetic hyperfine splitting may be severely broadened or even collapse because of their superparamagnetic relaxation (see Equation 2.48). At ambient temperature, magnetite and maghemite exhibit well defined magnetic hyperfine splitting only for particles with a diameter larger than about 15 nm. For smaller particles, low temperatures are required to slow down the superparamagnetic relaxation [82, 88, 89, 90]. Therefore, Mössbauer spectra of partially oxidised magnetite nanoparticles measured at 4.2 K, where the relaxation is certainly blocked, appear to be the only possibility for a characterisation. The downside of this approach is - besides the cost and the effort of implementing the helium cooling - that the evaluation of helium spectra is rather difficult [91].

However, even when superparamagnetic relaxation is fast due to the small size of the particles, a well-defined magnetic hyperfine splitting can be obtained by applying an external magnetic field, which magnetises the nanoparticles (see Section 2.5 as well as [92, 93, 94, 95]. Ferrimagnetic substances like magnetite or maghemite can be magnetised very easily which results in a significant hyperfine splitting for superparamagnetic iron oxide particles at ambient temperature, even for applied fields less than 1 T [96]. Due to the ferrimagnetic order, the hyperfine field at the A-sites will be parallel and the hyperfine field at the B-sites

anti-parallel to the applied magnetic field. This results in an increased magnetic hyperfine splitting for the iron nuclei at the A-sites and a reduced splitting for those on the B-sites. If the applied field is sufficiently strong, the tetrahedral and octahedral Fe(III) components in maghemite can actually be distinguished [97]. A comprehensive theoretical description of the influence of an external magnetic field on the Mössbauer spectrum of superparamagnetic nanoparticles requires a sophisticated quantum mechanical approach and can be found in the literature [98, 99, 100].

In the following, the construction of a magnet using NdFeB permanent magnets in a Halbach array is described. In this way, one can obtain a magnetic field at the Mössbauer absorber that is sufficient to yield magnetically split spectra of magnetite/maghemite nanoparticles at ambient temperature. With this approach, it is possible to distinguish between the two iron oxides in particles with diameters smaller than 15 nm without having to resort to measurements at liquid helium temperature.

3.2. Magnet Construction

The magnet is shown in Figure 3.1 a. Eight cuboidal permanent magnets (height = 19 mm, width = 19 mm, length = 120 mm, NdFeB, Ni-N52, ChenYang Technologies, China) are arranged in a circular Halbach array to produce a transverse magnetic field [101]. The cylindrical holder (length = 120 mm, outer diameter = 95 mm) for the magnets was produced from VeroWhitePlus acrylic resin using a 3D printer (Objet Eden260V, Stratasys Ltd, USA). The central borehole, where the Mössbauer absorber is placed, has a diameter of 20 mm, which allows for a satisfactory geometry for the Mössbauer experiments. The sample holder is placed in the centre of the Halbach cylinder and the sample is magnetised perpendicular to the propagation direction of the gamma rays. For the Mössbauer experiments, the source was positioned about 5 cm and the front of the electromechanical velocity motor 10 cm from the end of the magnet cylinder. Finite element analysis with COMSOL Multiphysics (COMSOL Multiphysics GmbH) was used to determine the magnetic flux density and its homogeneity inside and outside of the magnet. The distribution of the magnetic flux density norm over the borehole of the magnet at the position of the sample holder is shown in Figure 3.1 b. Figure 3.2 shows the distribution of the magnetic flux density norm in the plane along the symmetry axis (z-axis) of the cylinder inside and outside of the Halbach array. The calculated flux density norm on the axis of the magnet at the absorber position is 750 mT. At the position of the source and the motor, the calculated flux density norm is 10 mT and 0.9 mT, respectively.

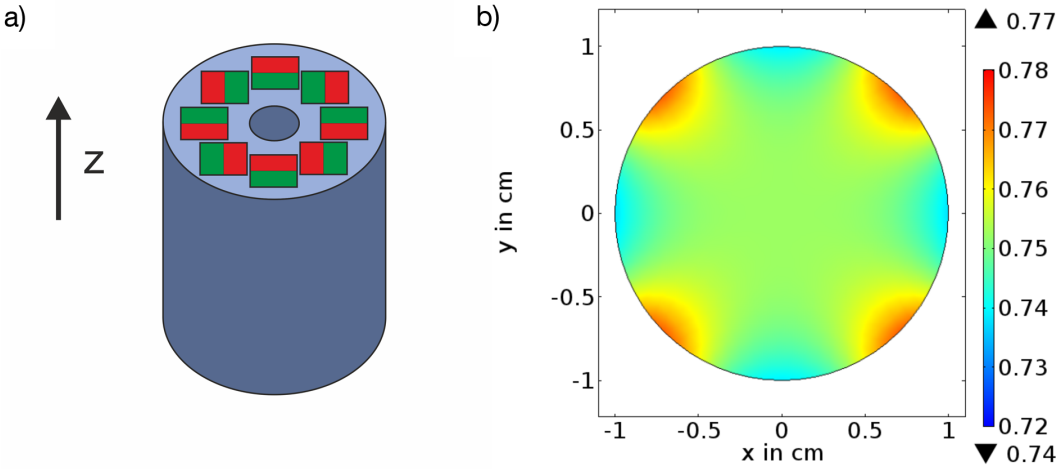

Figure 3.1.: Permanent magnets in a Halbach array for Mössbauer spectroscopy; (a) eight permanent magnets are arranged in a circle around an opening for the sample holder; (b) magnetic flux density norm distribution (in Tesla) at the position of the sample holder inside the magnet as determined by finite element analysis using COMSOL; The minimum (0.74 T) and the maximum value (0.77 T) of the flux density within the region shown here are indicated with a triangle pointing upwards and downwards, respectively. The magnetic field points in the y-direction. First published in [10].

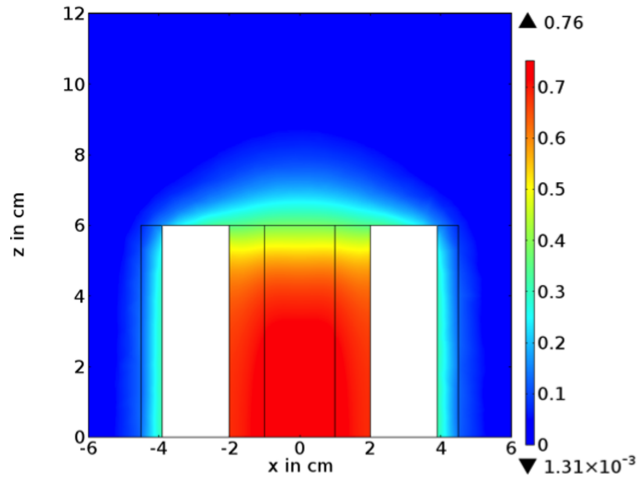

Figure 3.2.: Cross-sectional view showing half of the Halbach array and the magnetic flux density norm distribution (in Tesla) as determined by finite element analysis using COMSOL. The white areas represent the permanent magnets. The minimum and the maximum value of the flux density within the region shown here are indicated with a triangle pointing upwards and downwards, respectively. First published in [10].

In addition to the finite element analysis, the magnetic field was measured at three different positions with a Gaussmeter (Lake Shore Model 455 Gaussmeter, Lake Shore HMNT-4E04-VR transverse probehead, Lake Shore Cryotronics Inc.). The measured flux density on the symmetry axis of the magnet at the absorber position was 725 mT. At the position of the source, the flux density was 10 mT and at the position of the motor it had decreased to 0.9 mT, in excellent agreement with the calculations.

3.3. Magnetic Particles

For the synthesis of the magnetic nanoparticles, 45 mmol iron(II) chloride tetrahydrate were dissolved in 37 mmol 45% iron(III) chloride hexahydrate solution and were added to diethylene glycol (DEG) under constant stirring. The solution was purged with nitrogen throughout the reaction. Magnetite particles were precipitated at 170°C with sodium hydroxide and further incubated for 1 h. The DEG has been found to present a good protection of the particles against oxidation [102]. The following steps could therefore be carried out under aerobic conditions. After cooling to room temperature the magnetite particles were magnetically collected on a permanent magnet. A more detailed description of the particle

synthesis can be found in the literature [103, 102, 104].

The particles used for Mössbauer measurements were not separated from the DEG. For room temperature measurements, the particles were embedded in a solid matrix by mixing the DEG suspension with an equal amount of epoxy resin (Uhu Plus, UHU GmbH & Co. KG). After curing, the mixture became a solid suitable for room temperature Mössbauer spectroscopy and the particles were still found to be well protected against oxidation. For measurements at 4.2 K, the same sample was used. For particle size determination, the magnetically separated particles were dispersed in 1 M nitric acid and magnetically separated again. This washing step was repeated four times. After the last separation, the particles were re-suspended in de-aerated water to remove most of the acidic environment and stirred at room temperature overnight. The black suspension was sonicated in a water bath at room temperature for 45 min and afterwards centrifuged at 16700 rcf at 21°C for 1 h. The particle suspension thus obtained was used for size determination. For magnetisation measurements, a sample was freeze-dried overnight. Mössbauer measurements have shown that the treatment of the particles after removal from the DEG results in a considerable degree of oxidation [102].

3.4. Methods

For a more detailed description of magnetometry (magnetisation measurement) and Mössbauer spectroscopy please refer to Chapter 2.

3.4.1. Size Characterisation

The size of the particles was determined by transmission electron microscopy (TEM) and dynamic light scattering (DLS). TEM was performed with a JEM-100CX (JEOL Ltd.) at 100 kV. For the sample preparation, about 5 μl of a 10 mM Fe particle suspension were applied to a 300 mesh grid coated with carbon. Subsequently, the particles were air-dried at room temperature. The size distribution of the MNPs was determined from the TEM images with the Analyse Particles feature of the image-processing software ImageJ. The hydrodynamic diameter of the particles was determined using a Zetasizer Nanoseries NanoZS (Malvern Instruments GmbH), which allows both number and intensity weighted size distributions to be measured. The particles were diluted in deionised water to 10 mM Fe for both techniques.

3.4.2. Magnetisation Measurements

First, the freeze-dried particles were embedded in Fixogum (Marabu GmbH & Co. KG). The Superconducting Quantum Interference Device (SQUID) measurements were then performed using a MPMS XL (Quantum Design Inc.) at flux densities between -3.5 T and 3.5 T, thereby obtaining the room temperature M(B) curve.

3.4.3. Mössbauer Spectroscopy

The Mössbauer transmission measurements were performed with a source made of ^{57}Co in rhodium, which had an activity of about 1 GBq, and an electromechanical velocity drive using a sinusoidal velocity waveform (MA 250 Halder Electronics). At room temperature, measurements were performed with and without the external magnetic field. For the measurements at 4.2 K without magnetic field, a liquid helium bath cryostat was used, in which the source was also cooled to 4.2 K.

The spectra were fitted using the least-squares method with a superposition of sextets which in turn consisted of Lorentzian lines. In some cases, additional Voigt profiles were used in order to obtain good fits. These profiles correspond to static distributions of hyperfine fields, although this does not take into account the relaxation processes. Details of the Mössbauer spectra evaluation will be described together with the results.

3.5. Results and Discussion

3.5.1. Particle Size

The size of the MNPs was determined by the evaluation of TEM images and by DLS. Both measurements were performed after the particles had been transferred from DEG to the aqueous medium. Figure 3.3 depicts a TEM image (a), the resulting size distribution of the magnetic nanoparticles (b) and the DLS results with both the intensity and the number distribution (c). In TEM image analysis, the diameter of each single particle is measured and morphological information is provided at the same time with the size of the core. In order to obtain TEM images, the particles first have to be dried on the grids. During the course of the drying process, aggregation of the particles can occur, which can corrupt the size evaluation [105]. The mean diameter obtained from TEM analysis is $d = 5.8 \pm 1.7$ nm, where the uncertainty represents the width of the size distribution.

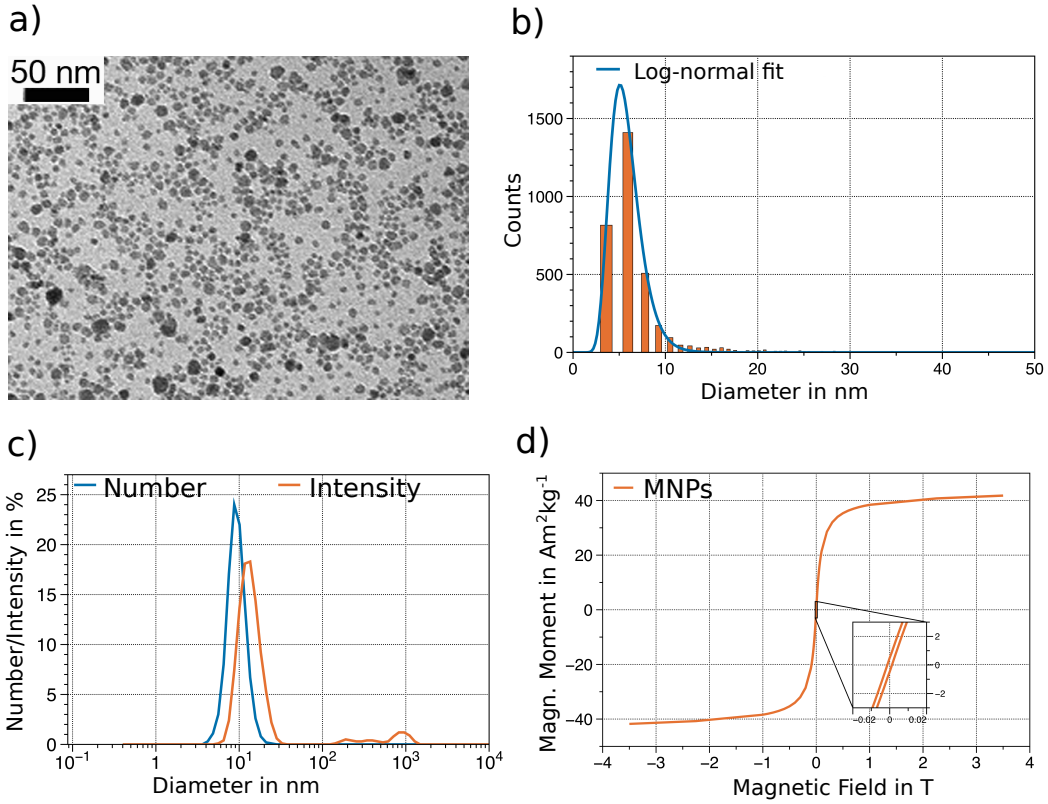

Figure 3.3.: a) TEM image of magnetic nanoparticles; b) the size distribution from TEM image analysis ($d = 5.8 \pm 1.7$ nm); c) determination of the size distribution by DLS measurements ($n = 3$) according to the intensity distribution ($d = 14.0 \pm 1.8$ nm) and the number distribution ($d = 9.7 \pm 1.1$ nm); d) M(B) curve of the freeze-dried particles (taken from [102]) which had completely oxidised to maghemite at the time of the measurement. The stated uncertainties represent the widths of the size distributions. First published in [10].

Using DLS measurements the hydrodynamic diameter can be obtained very quickly in a few minutes. The measurements are done in the liquid suspensions of many particles and not with just a few. In Figure 3.3 c one can see a clear shift from larger diameters in the intensity distribution to smaller diameters in the number distribution. The few bigger particles (> 100 nm in diameter) are only noticeable in the intensity distribution. The mean diameter for the intensity distribution is 9.7 ± 1.1 nm nm and for the number distribution it is 14.0 ± 1.8 nm.

The sizes obtained by DLS measurements are larger compared to the sizes obtained by TEM image analysis. There are various reasons for that. First, the solvent for the measurements

has to be chosen correctly to circumvent possible hydration artefacts and ion shells around the particles [106]. Second, the concentration of the particles has some influence on the results of the measurements. Third, in DLS measurements, larger particles are always more prominent in their detection than smaller particles [107]. To reduce this artifact, the diameter of number weighted size distributions is calculated from the intensity weighted size distributions taking this size shift into account. This can be seen in the difference between the intensity and the number weighted size distribution of the naked MNPs. Therefore, it is always important not only to rely on the mean values given by the DLS system, but also to observe the size distributions. Hence, it is not surprising that the diameters obtained by DLS measurements are larger compared to the ones obtained by TEM image analysis.

3.5.2. Magnetisation Measurements

The M(B) measurement was performed after the particles had been transferred to aqueous medium. According to Mössbauer spectroscopy the particles were completely oxidised to maghemite when this measurement was taken [102]. The saturation magnetisation of the particles was deduced from the M(B) curve (Figure 3.3 d) to be 41 Am^2kg^{-1}.

3.5.3. Mössbauer Spectra

Mössbauer measurements were first performed with freshly prepared magnetite nanoparticles embedded in epoxy resin. The resulting spectra are shown in Figure 3.4 a-c. After the same absorber had been kept in air for 16 months at room temperature, Mössbauer spectra were acquired again (Figure 3.4 d-f). The epoxy resin protects the nanoparticles quite well from oxidation, but after the prolonged exposure to air, the particles had oxidised to maghemite almost completely.

Mössbauer measurements were performed at room temperature (298 K) with and without the external magnetic field. For comparison and verification of the determined maghemite proportion and therby the degree of oxidation, the particles were also measured without magnetic field at 4.2 K. The Mössbauer parameters of the spectra at room temperature with field and at 4.2 K are summarized in Table 3.1. The parameters of the spectra acquired at room temperature without magnetic field are not presented, because these spectra do not permit a meaningful interpretation.

In all spectra, a small contribution of metallic iron of 2-3 % of the spectral area is observed. This must have formed during the handling of the nanoparticles and the preparation of the

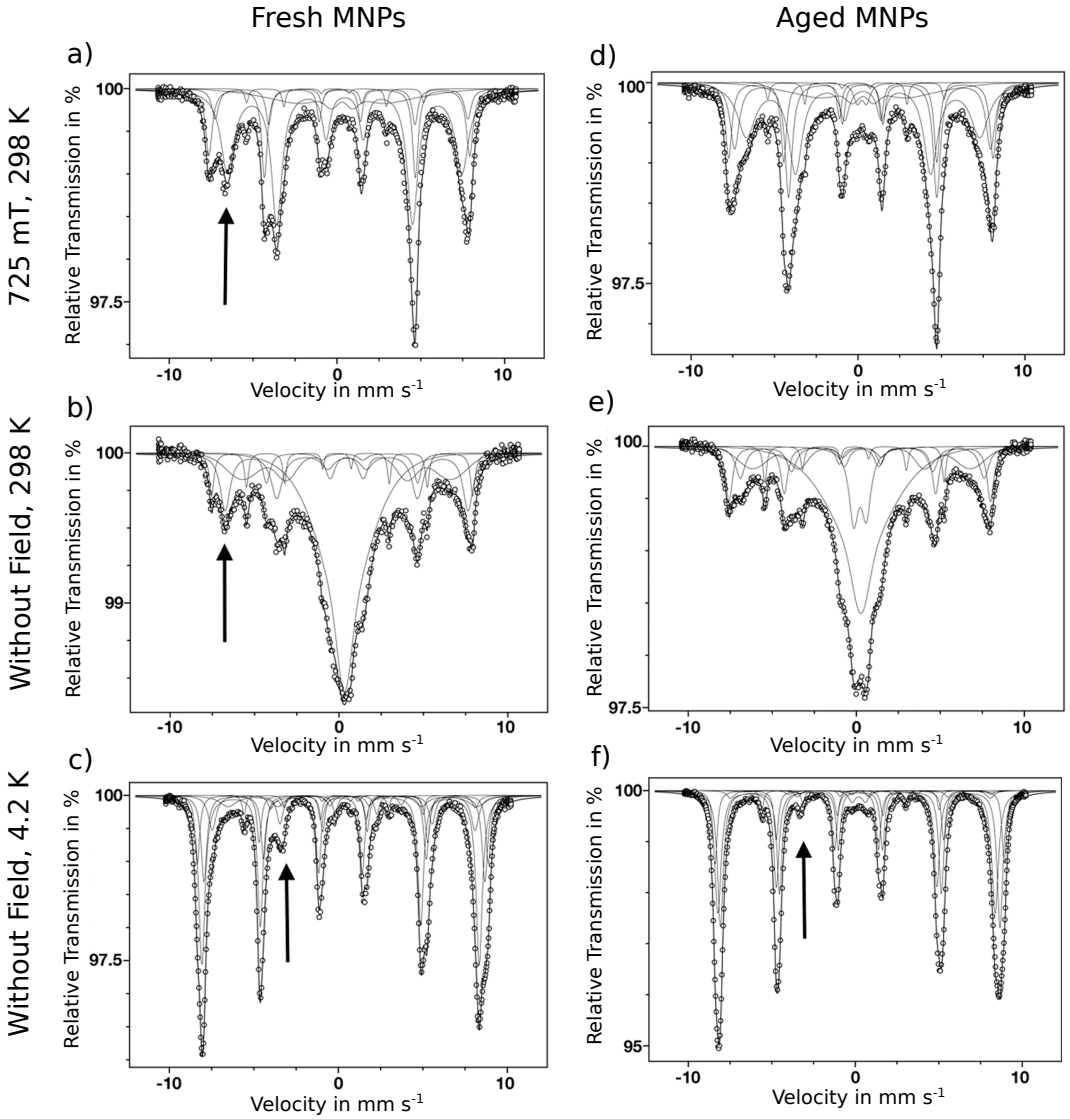

Figure 3.4.: ^{57}Fe Mössbauer spectra of the fresh and aged magnetic nanoparticles with and without external magnetic field as well as at 4.2 K. The arrows indicate the peaks that correspond to the Fe(2.5) contributions (a, b) and the Fe(II) contributions (c,f), respectively. First published in [10].

Table 3.1.: ^{57}Fe Mössbauer parameters of the fresh and aged samples at room temperature with external magnetic field ($T = 298$ K, left) and at helium temperature ($T = 4.2$ K, right). RA stands for the relative area in percent, IS is the isomer shift in mm s^{-1}, QS the quadrupole shift in mm s^{-1} and HF the hyperfine field in Tesla. First published in [10].

298 K

		Fresh	**Aged**
Gauss Sextet	RA	10.9±0.4	11.8±0.8
	IS	0.30±0.01	0.30±0.01
	QS	0.00±0.01	0.00±0.01
	HF	19.1±0.4	28.8±0.7
Tetr. Fe(III)	RA	21.3±0.5	14±1
	IS	0.16±0.01	0.19±0.01
	QS	-0.04±0.01	0.02±0.01
	HF	48.3±0.2	49.5±0.2
Oct. Fe(III)	RA	9.2±0.1	24.8±0.3
	IS	0.27±0.01	0.23±0.01
	QS	-0.02±0.01	-0.01±0.01
	HF	46.7±0.2	47.5±0.2
Fe(III)	RA		44±2
	IS		0.31±0.01
	QS		0.01±0.01
	HF		43.7±0.2
Fe(2.5)	RA	55.9±0.7	
	IS	0.46±0.01	
	QS	0.01±0.01	
	HF	43.4±0.2	
Doublet	RA		3.3±0.1
	IS		0.25±0.01
	QS		0.61±0.02
Iron (metal.)	RA	2.7±0.2	2.3±0.1
	IS	-0.11±0.01	-0.12±0.01
	QS	0.00±0.01	0.00±0.01
	HF	32.7±0.2	32.8±0.2

4.2 K

		Fresh	**Aged**
Tetr. Fe(III)	RA	42.4±0.5	36.3±0.4
	IS	0.12±0.01	0.07±0.01
	QS	-0.01±0.01	-0.02±0.01
	HF	51.0±0.3	51.5±0.3
Oct. Fe(III)-1	RA	23.0±0.6	40.7±0.6
	IS	0.36±0.01	0.29±0.01
	QS	0.01±0.01	-0.00±0.01
	HF	51.6±0.3	51.9±0.03
Oct. Fe(III)-2	RA	9.1±0.5	13.1±0.4
	IS	0.28±0.01	0.25±0.01
	QS	-0.02±0.01	0.02±0.01
	HF	53.5±0.3	53.7±0.3
Oct. Fe(II)-1	RA	10.0±0.4	1.6±0.1
	IS	0.69±0.01	0.68±0.01
	QS	-0.76±0.01	-0.73±0.01
	HF	48.4±0.2	48.2±0.2
Oct. Fe(II)-2	RA	9.4±0.3	2.4±0.2
	IS	0.73±0.02	0.75±0.02
	QS	0.12±0.04	0.17±0.01
	HF	46.0±0.2	45.6±0.2
Oct. Fe(II)-3	RA	3.4±0.1	0.9±0.1
	IS	1.14±0.01	1.14±0.01
	QS	1.78±0.01	1.85±0.01
	HF	37.6±0.2	37.6±0.2
Doublet	RA		1.9±0.1
	IS		0.21±0.01
	QS		0.80±0.01
Iron (metal.)	RA	2.7±0.1	3.0±0.1
	IS	-0.11±0.01	-0.08±0.01
	QS	0.00±0.01	0.00±0.01
	HF	34.0±0.2	34.0±0.2

Mössbauer samples. Unfortunately, attempts to determine why, how and at which point during the preparation this metallic iron formed, were not successful. The iron contribution was taken into account for the calculation of the magnetite content. The fraction of magnetite in the sample at room temperature was calculated by dividing the relative area of the mixed-valence sextet by 2/3, because its intensity is expected to be 2/3 for pure magnetite. At 4.2 K the intensities of the Fe(II) sextets was summed up and divided by 1/3, which corresponds to the value expected for pure magnetite.

The spectrum of the fresh sample without magnetic field at room temperature is dominated by a broad central peak (Figure 3.4 b) which was approximated by a broad Gaussian distribution of magnetic hyperfine fields. The mean value of this Gaussian distribution was set to zero. The peak can be attributed to the smaller particles in the sample and is a result of their fast superparamagnetic relaxation. A broad sextet pattern which is described by a distribution of hyperfine fields can be attributed to medium-sized particles. It is not possible to determine the iron oxide type of the parts of the spectrum mentioned so far. The rest of the spectrum originates from the biggest particles in the sample and shows sufficient hyperfine splitting for the identification of Fe(III) and a mixed-valence Fe(2.5) sextet. The latter is indicated by an arrow in Figure 3.4 b. However, smaller particles are likely to be more oxidised due to the higher ratio between surface area and volume and thus contain a higher fraction of maghemite than bigger particles. Hence, the part of the spectrum which arises from the biggest particles in the sample is not representative and cannot be used to determine the magnetite fraction of the whole sample.

The spectrum of the aged sample without magnetic field at room temperature is similar. In comparison to the spectrum of the fresh sample, however, the relative area of the Fe(2.5) sextet has significantly decreased in intensity and the sextet has become broader (Figure 3.4 e). Since this well-split sextet represent the bigger particles, this shows that these have oxidised to some extent, but not completely. In order to obtain a good fit of the spectrum, a quadrupole doublet is needed. This may represent the smallest particles in the sample, which now exhibit an even faster superparamagnetic relaxation due to oxdiation. On a general note, without the application of an external magnetic field at room temperature, the amount of magnetite compared to maghemite in a sample containing small particles (diameter < 15 nm) cannot be estimated.

However, if a magnetic field of 725 mT is applied at room temperature, the magnetic hyperfine splitting is strong enough to produce rather well resolved Mössbauer spectra (Figure 3.4

a and d). The mixed-valence Fe(2.5) contribution in the spectrum of the freshly prepared particles can easily be recognized and is indicated by an arrow in Figure 3.4 a. The applied field also makes it possible to differentiate between tetrahedral and octahedral Fe(III) because the external field increases the hyperfine field on the A sites but reduces it on the B sites. Besides the well resolved lines, a broad sextet is also necessary to obtain a good fit of the data, because of the drop of the spectrum at the center. Owing to the Gaussian distribution of the (static) hyperfine fields, this sextet is called 'Gauss sextet' in table 3.1. Presumably, this component represents particles that are so small that they cannot be magnetised in the applied field and therefore still show relaxation effects. Due to their small size, it is justified to assume that these particles were completely oxidised. For the calculation of the magnetite content, they were therefore presumed to consist of pure maghemite. Consequenty, a magnetite content of 86% was obtained from the spectrum of the fresh sample at room temperature with the magnetic field.

After 16 months, the mixed-valence Fe(2.5) sextet is no longer detectable in the spectrum (Figure 3.4 d), which indicates almost complete oxidation of the iron in the sample. As in the fresh sample, the tetrahedral and octahedral Fe(III) can be distinguished and the relative area of the octahedral iron has increased considerably. There is a third rather well-split sextet with a smaller hyperfine field, whose Mössbauer parameters indicate that it is also at least largely Fe(III). This component may represent particles at the lower end of the size distribution, which may not be fully magnetised. As in the spectrum of the aged sample acquired without external magnetic field, the quadrupole doublet is also present here.

The SQUID measurements showed a magnetic saturation of about 80% of the saturation magnetisation for the oxidised particles at 725 mT (Figure 3.3 d) [102]. The room temperature Mössbauer measurements bear out the expectation that the magnetic field of 725 mT is enough to induce sufficient hyperfine splitting for most particles in the sample to enable an estimation of the Fe(2.5) content (Figure 3.4 a and d) and that samples can be compared with respect to their magnetite content.

The 4.2 K spectra were fitted similar to [102] with one sextet for Fe(III) on the tetrahedral sites, two sextet components for Fe(III) on the octahedral sites and three sextet components for Fe(II) on the octahedral sites. The Fe(II) sextets are shifted towards positive velocities with respect to the Fe(III) sextets resulting in an asymmetric overall Mössbauer pattern. The three components for Fe(II) were found necessary because the Fe(II) lines were considerably broadened. The Fe(II) contribution in the spectra is most readily observable at

the position indicated by an arrow and the intensity of this peak allows for a rough, qualitative estimation of the magnetite content of a sample. The quantitative evaluation of the magnetite fraction yielded 70% in the fresh sample and 15% in the oxidised sample, which differs significantly from the values obtained at room temperature with applied field. The reason for this discrepancy is that the fitting procedure of the spectra is not unambiguous. This will be explained in more detail in the error analysis section. The metallic iron has only a minor influence on the evaluation of the magnetite fraction of the 4.2 K spectra.

3.5.4. Mössbauer Spectra - Error Analysis

The uncertainty of the quantitative evaluation of the magnetite content is mainly a result of the difficult fitting procedure. The room temperature spectra with external field typically consist of at least three sextets (not counting the 'Gauss sextet') while the the 4.2 K spectra are fitted using up to six sextets. Each sextet in turn is characterised by several parameters, for example intensity, isomer shift, quadrupole shift and line width. Therefore, a huge number of parameters determine the overall fit. It is up to the experience and the skill of the researcher evaluating the spectra to find a good fit by choosing the number and type of sextets and to play around with the different parameters. For this reason, the fitting procedure of iron oxide Mössbauer spectra is very challenging and the results of the fit and thereby the quantitative evaluation of the magnetite content depend on personal experience and ability. Furthermore, this makes a quantitative estimation of the uncertainty of the results extremely difficult.

A broad size distribution of the particles further complicates the fitting procedure. The results of the TEM measurements show that after centrifugation, the particles have a core diameter of 5.8 ± 1.7 nm. The sample used for Mössbauer spectroscopy was taken before centrifugation, which means that the size distribution was probably broader in the Mössbauer samples than in the samples used for TEM and DLS. While the superparamagnetic relaxation can be suppressed in bigger particles due to low temperature or application of an external field, smaller particles still experience Néel relaxation and therefore exhibit significant line broadening and less hyperfine splitting. The fitting procedure using a finite number of sextets cannot perfectly account for this behaviour. This is especially evident in Figure 3.4 e, where a total of three Gauss sextets and a doublet are used to account for the size distribution of the particles.

3.6. Conclusion

The experiments confirm that iron oxide nanoparticles with sizes smaller than about 15 nm cannot be characterised by means of Mössbauer spectroscopy at room temperature because of fast superparamagnetic relaxation. A Halbach array of permanent magnets was constructed and used for the magnetisation of the particle samples. This led to a suppression of the hyperfine field fluctuations. In this way, magnetically split Mössbauer spectra were obtained at room temperature. The small field of 725 mT induced sufficient hyperfine splitting in the nanoparticles for a meaningful evaluation of their magnetite content. This approach is cheap and does not require liquid helium cooling, which is why it is expected to facilitate the characterisation and quality assessment of iron oxide nanoparticles in the future.

4. Size-dependent MR Relaxivities of Magnetic Nanoparticles

Except for the section about the simulation, this chapter is based on the paper "Size-dependent MR relaxivities of magnetic nanoparticles", published in 2017 in the Journal of Magnetism and Magnetic Materials [11]. I wrote the whole publication and performed the relaxation rate measurements and their evaluation.

This publication investigates the dependence of the R_2 and R_2^* relaxivities on the size of magnetic nanoparticles using a relatively new method for fractionating MNPs with respect to their size. In addition, the particles were characterised using MPS. With this new approach, magnetic nanoparticles can be comprehensively characterised regarding their contrast enhancing properties in MRI and their suitability for quantification by MRI relaxometry.

4.1. Introduction

Various types of nanoparticles are used in biomedical applications. Magnetic nanoparticles are especially promising because of their multi-functional capabilities such as bioseparation, transfections, hyperthermia, targeted delivery of drugs and stem cell tracking [1, 2, 3]. For the latter two it is crucial to quantitatively determine the spatial distribution of the concentration and the aggregation state of the MNPs to monitor and improve the efficacy of the application. Quantitative imaging of MNPs is enabled by magnetic resonance (MRI) and magnetic particle imaging (MPI). While MNP specific MPI is inherently quantitative, MRI detects magnetic particles non-specifically by measuring the effect of local field disturbance.

Theoretical considerations, simulations and experiments have shown that the MR relaxation rates R_2 and R_2^* strongly depend on the size of the MNPs or aggregates, respectively [36, 108, 34, 33, 109, 110]. Three different regimes can be distinguished, with aggregates being treated the same way as particles using adapted overall hydrodynamic diameters d_{Hyd}

and saturation magnetisations M_S. A more detailed discussion of the relaxation theories can be found in Section 2.2.4, which is why just a brief repetition is given here. For small particles and aggregates that satisfy the motional averaging condition $\Delta\omega\tau_D < 1$ the quantum mechanical outer sphere theory applies:

$$R_2 = R_2^* = \frac{16}{45} f(\Delta\omega_{\mathrm{eq}})^2 \tau_D \propto {d_{\mathrm{Hyd}}}^2 \ . \tag{4.1}$$

where $\Delta\omega = \gamma\frac{\mu_0}{3}M_S$, $\tau_D = \frac{{d_{\mathrm{Hyd}}}^2}{D}$, D is the self diffusion coefficient of water and f the volume fraction of the particles in the sample, which can be converted into the iron concentration. For particles that are too big to satisfy the motional averaging condition ($\Delta\omega\tau_D > 1$), the relaxation behaviour can be described by the static dephasing regime (SDR) model [35]:

$$R_2 = R_2^* = \frac{2\pi}{3\sqrt{3}} f \Delta\omega_{\mathrm{eq}} \ . \tag{4.2}$$

Here, the relaxation rates only depend on the volume fraction and not on the particle size. For even larger particles, refocusing pulses become efficient and R_2 decreases again according to the partial refocusing model [36], while R_2^* remains the same:

$$R_2 = 2.25\frac{x^{1/3}}{\tau_D}[1.34 + fx]^{5/3} < R_2^* \ , \tag{4.3}$$

where $x = \sqrt{4/5}\gamma\frac{\mu_0}{3}M_S T_{\mathrm{E}}$ and T_{E} is the echo time.

This size-dependent behaviour shows that R_2 measurements can be used to assess the aggregation state of the MNPs whereas R_2^* measurements are independent of aggregation state and therefore suited for MNP quantification if the condition of static dephasing is met [8]. To allow a reliable quantification by MRI relaxometry, it is therefore essential to test whether the used particles are big enough to satisfy the SDR condition. In practice however, this is complicated by the size distribution of the particles.

A new experimental approach to characterise an MNP system with respect to quantitative MRI is presented here. This method is based on hydrodynamic fractionation producing MNPs with different well-defined sizes and subsequent geometric, magnetic and MR relaxation characterisation of the fractions. This allows to test the suitability of the MNP system for quantitative MRI and verify the theoretical predictions for the size dependence of relaxation rates at the same time. This new approach is applied to the two commercially

available MNP systems Resovist® and Endorem®.

4.2. Simulation of Relaxation Times

Before proceeding to the experimental part, a Monte Carlo method for the simulation of R_2 and R_2^* relaxation rates will be presented. Simulating relaxation rates improves the understanding of the underlying relaxation mechanism and can be used to double-check and even predict experimental results. I implemented the simulation using Matlab in the course of my Diploma research and this section is based on the corresponding section in my Diploma thesis [19]. The algorithm itself is based on an approach described in several publications [36, 108, 34, 111, 112, 113].

4.2.1. Algorithm and Implementation

The algorithm calculates relaxation curves based on the dominant relaxation mechanism for magnetic nanoparticles, which is the dephasing of the proton spins caused by the magnetic dipole fields of the particles. During the first step of the algorithm, the magnetic nanoparticles are placed inside a restricted, cubical simulation space by creating position vectors. The number of particles N_{MNP}, their size, shape, magnetic properties and spatial distribution are chosen depending on the application. The edge length of the cubical simulation space is calculated from the desired volume fraction and number of particles according to the following formula:

$$L = \sqrt[3]{\frac{N_{\mathrm{MNP}} \pi d_{\mathrm{Hyd}}^3}{6f}} \quad . \tag{4.4}$$

The position vectors of the water protons are randomly distributed in space, but the protons are not allowed to be inside a nanoparticle. The number of water protons is chosen depending on the available computational power - using more water protons essentially leads to a smoother relaxation curve, but increases the computation time and also the working memory requirements.

In the next step, the water protons perform a random walk, thereby mimicking the Brownian diffusion process in the magnetic field created by the nanoparticles (Figure 4.1 a). For every time step n, the new position of every water proton i is calculated by adding a randomly oriented three-dimensional displacement vector $|\Delta\vec{x}|$, whose length is given by the Stokes-

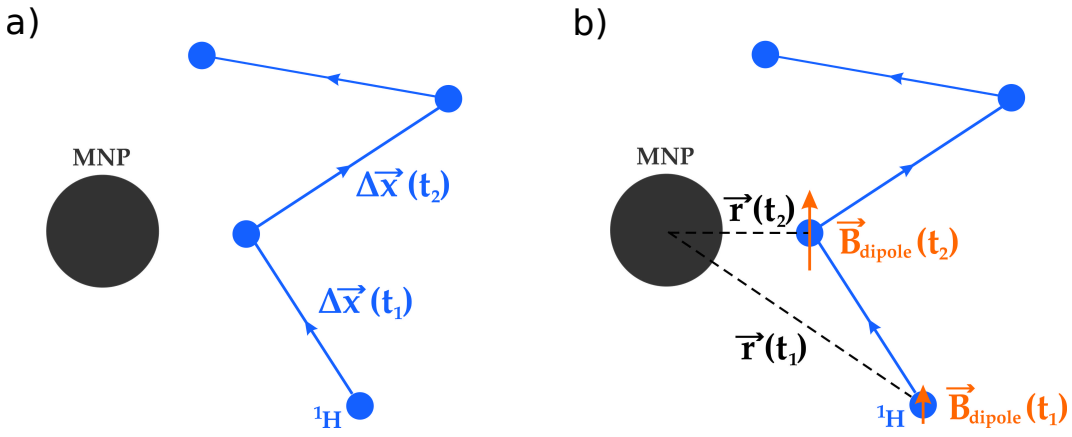

Figure 4.1.: a) Water proton performing a random walk in the vicinity of a magnetic nanoparticle; b) The magnetic dipole field experienced by the water proton is stronger when it is closer to the particle.

Einstein equation:

$$\vec{r}_{\mathrm{i,n}} = \vec{r}_{\mathrm{i,n-1}} + \Delta\vec{x} \ , \qquad |\Delta\vec{x}| = \sqrt{6D\Delta t} = \sqrt{\frac{k_{\mathrm{B}}T\Delta t}{\pi\eta R_{\mathrm{water}}}} \ . \tag{4.5}$$

Here, k_{B} is the Boltzmann constant, T the temperature, η the dynamic viscosity of the liquid, R the Radius of a water molecule and Δt is the chosen time step. Since the radius of a nanoparticle is at least a factor of 100 larger than that of a water molecule, the diffusion of the particles can be neglected. The movement of the water protons is restricted by two conditions that have to be checked for every proton at every time step. First, if a proton accidentally ends up inside of a particle, it is placed back at its previous position. Second, if a proton ends up outside the simulation space, its position is mirrored to the other side of the cube.

For every position in space, the magnetic dipole field that is created by the particles is different (Figure 4.1 b). The z-component of this dipole field therefore causes every water proton to precess at a slightly different Larmor frequency. In the rotating frame ($\omega = \gamma B_0$), the shift of the precession frequency results in a change of phase of every proton at every time step.

$$\Delta\phi_{\mathrm{i,n}} = \gamma B_{\mathrm{tot}}(\vec{r}_{\mathrm{i,n}})\Delta t \ , \quad B_{\mathrm{tot}} = \sum_{\mathrm{MNPs}} B_{\mathrm{dipole}} \ , \quad B_{\mathrm{dipole}} = \frac{\mu_0\mu}{4\pi}\frac{3\cos^2\theta - 1}{r^3} \ . \tag{4.6}$$

μ_0 is the vacuum permeability, μ the magnetic moment of the particle, r the distance between proton and particle and θ the angle between the connecting vector of the proton and the particle and the axis of magnetisation of the particle, which is assumed to be fully aligned with the B_0 field (z-direction). The magnetic nanoparticles are therefore being treated as point dipoles which has been confirmed to be a very good approximation using COMSOL. Protons close to the edge of the finite simulation space experience a slightly different magnetic dipole field than protons closer to the center, because they only get influenced by nanoparticles from one side. This edge effect is being neglected in the simulation.

After the initial $90°$-pulse around the y-axis, the normalised magnetic moment of a proton in the rotating frame is given by:

$$\vec{\mu}_{\mathrm{i,n}} = (\cos\phi_{\mathrm{i,n}}, \sin\phi_{\mathrm{i,n}}, 0)) \ , \quad \phi_{\mathrm{i,n}} = \phi_{\mathrm{i,n-1}} + \Delta\phi_{\mathrm{i,n}} \ . \tag{4.7}$$

The simulation treats the proton spins as a classical vector. The magnetic moment in Equation 4.7 must therefore be interpreted as the quantum mechanical expectation value of an ensemble of proton spins that follow the same diffusion path. In order to simulate the effect of a $180°$ refocusing pulse, the phase of every proton spin is simply inverted from $\phi_{\mathrm{i,n}}$ to $-\phi_{\mathrm{i,n}}$ at each echo time. In the final step of the simulation, the total transverse magnetisation $\langle\mu_{\mathrm{n}}\rangle$ at every time step is calculated by averaging over all magnetic moments and the relaxation rates R_2 or R_2^* are extracted by fitting the magnetisation curve. The simulation was implemented in Matlab and executed on a workstation for more computational power. In order to speed up the computation, parallel programming was used by distributing the individual proton spins among the CPU cores.

4.2.2. Applications

An important question is whether the simulation predicts the same size dependence of the R_2 relaxation times as the analytical theories. For this purpose, R_2 relaxation rates were simulated for ten different particle radii ranging between 5 nm and 300 nm using a constant volume fraction and the same physical parameters as in [34]. As opposed to [34], only one nanoparticle in the center of the simulation space and 2500 protons were used in order to save computation time. In addition, an adaptive increment $|\Delta\vec{x}| = d_{\mathrm{Hyd}}/2$ was used for the random walk. The simulation was run three times in order to get an estimate for the computational uncertainty. The average of the three runs and the standard deviations are shown in Figure 4.2. For comparison, the results of the analytical theories were plotted in the same diagram. Within the standard deviation, the simulated and the analytically calculated relax-

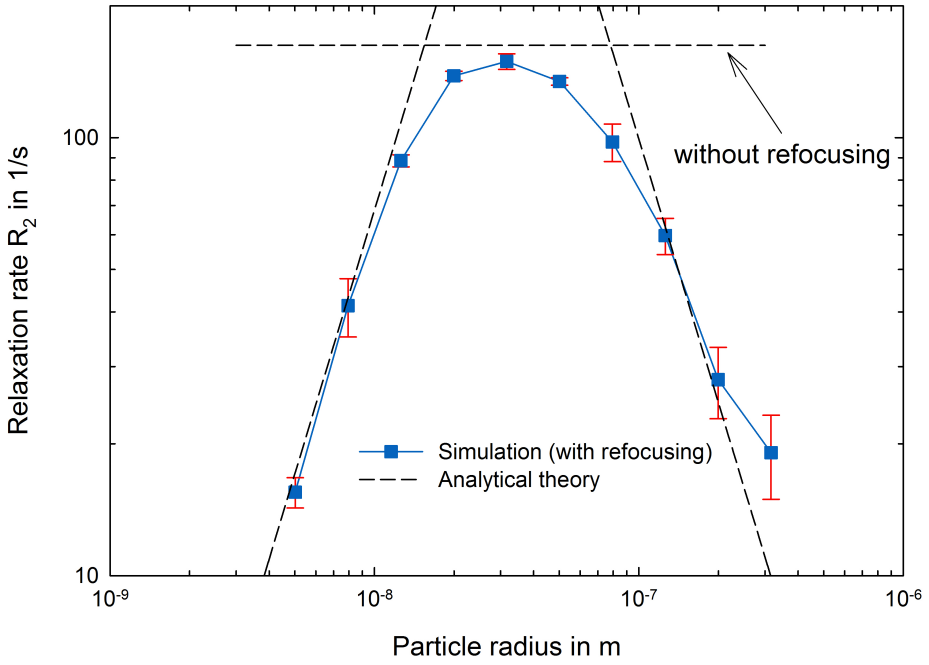

Figure 4.2.: Relaxation rate R_2 as a function of the particle radius as simulated using adaptive $|\Delta\vec{x}|$ and parameters as in [34]. The error bars represent the standard deviation of the three separate runs. The dashed lines represent the analytical theories.

ation rates are in good agreement. It was also found that the use of a larger increment $|\Delta\vec{x}|$ results in incorrect relaxation rates in the motional averaging regime.

Other situations that can be investigated using the simulation include the influence of the echo time and the effect of aggregation of particles by starting the simulation with different spatial distributions of nanoparticles. Since only one MNP was used for the above simulation, the result is only valid for monodisperse particles which is not always realistic. In order to investigate the effect of the size distribution, a lot more particles have to be used for the simulation, which will drastically increase the computation time. It is also possible to predict concrete experimental results for R_2 and R_2^*. For this purpose, the physical parameters entering the simulation such as the particle magnetic moment have to determined in a separate experiment.

In conclusion, the simulation is a powerful tool for understanding and investigating the NMR relaxation effects of magnetic nanoparticles. Most importantly, the analytical theories for the size dependence are strongly underpinned by the results of the simulation.

4.3. Material and Methods

The employed methods are only described here in a short form. More details about MPS and relaxation rate measurements can be found in Chapter 2.

4.3.1. MNPs

Ferucarbotran, which is a precursor of the commercial MRI contrast agent Resovist® was provided by Meito Sangyo (JPN) and Endorem® (namely ferumoxide) was purchased from Guerbet (FRA) . Both are aqueous suspensions of iron oxide nanoparticles and are approved specifically as MRI liver contrast agents. Whereas Resovist® is known to contain single and multi-core MNPs coated with dextran [76, 114], Endorem consists only of multi-core MNPs coated by a thin dextran layer [115, 116]. Transmission electron microscopy images can be found in [117, 118] for Resovist® and in [115, 116] for Endorem®. Deionized water containing 0.2% (v/v) FL70 detergent (Fisher Sci., USA) was used as carrier liquid for hydrodynamic fractionation.

4.3.2. Hydrodynamic Fractionation

The fractionation was performed using an asymmetric flow field-flow system (abbr. A4F; AF2000, Postnova Analytics GmbH, Germany) as described in [114] and fractions were collected from 5 (Resovist®) and 3 (Endorem®) consecutive runs. A4F is based on an elution method where the hydrodynamic diameter d_{Hyd} of an MNP is related to its retention time within a separation channel. The channel outlet was directly coupled to the UV detector, followed by MALS, DLS and finally MPS.

4.3.3. Size Characterisation by DLS and MALS

Hydrodynamic diameters were determined by dynamic light scattering (DLS) using a Malvern Instruments particle sizer (Zetasizer Nano ZS, Malvern Instruments, UK; λ = 633 nm). In addition, multi-angle laser light scattering (abbr. MALS; PN3621, Postnova Analytics GmbH; λ = 532 nm) was used to measure the angular dependence of scattered light on MNP size fractions. From this, the radius of gyration r_G was derived using the intensity

distribution function for spherical particles. The core diameter d_C was calculated by the following equation: $d_C = \sqrt{20/3} * r_G$. As small MNPs scatter light isotropically, the lowest detectable d_C is about 20 nm [119].

4.3.4. Magnetic Characterisation by MPS

The samples were magnetically characterised by Magnetic Particle Spectroscopy (MPS) using a commercial MPS device (MPS-3, Bruker BioSpin, Germany). Based on the same physical principle as MPI, waiving of any spatial encoding, MPS detects the non-linear dynamic magnetic susceptibility of MNPs. MPS is proven to be a straightforward technique for specific quantification and characterisation of MNPs [73], and allows for validation and improved understanding of MR relaxation measurement results. During an MPS measurement, a sinusoidal excitation is applied to the sample. Due to the non-linear magnetisation curve of the MNPs, the measured magnetic response contains odd multiples of the excitation frequency, which can be visualized by a Fourier transform. Therefore, the MPS signal depends on the effective magnetic moment of the MNPs. Here, the spectral magnetic moment of the third harmonic divided by the iron content is used.

4.3.5. Relaxation Rate Measurements

R_2 and R_2^* were measured in aqueous medium, because the process of embedding MNPs in agarose or other gels can cause aggregation which in turn would distort the size dependence of the MR relaxation rates. Precise measurements of R_2 and R_2^* with MRI takes at least several minutes. During this time span, the magnetic dipole-dipole interaction between the aligned magnetic moments of the MNPs can cause chain formation and aggregation as well [120]. Therefore, all samples were individually measured in an NMR spectrometer (Magritek Spinsolve 1 Tesla), allowing R_2 and R_2^* determination within seconds after inserting the sample into the magnetic field. In order to check whether the relaxation rates changed on this time scale, the measurements were repeated several times within one minute after inserting the samples.
To obtain the relaxation curves, an FID (90° pulse) was acquired for R_2^* while for R_2 a CPMG sequence was used (echo time 200 μs, 10000-20000 echoes). The relaxation rates were extracted by fitting $A \times \exp\left(-tR_2^{(*)}\right) + B$ to the measured signal decay, with A, B and $R_2^{(*)}$ as free parameters. The curve fitting was performed using Matlab (The MathWorks Inc., Natick, MA, USA). Relaxation rates were finally corrected by the relaxation rates of the solvent and divided by the iron content to get the relaxivities $r_2^{(*)}$.

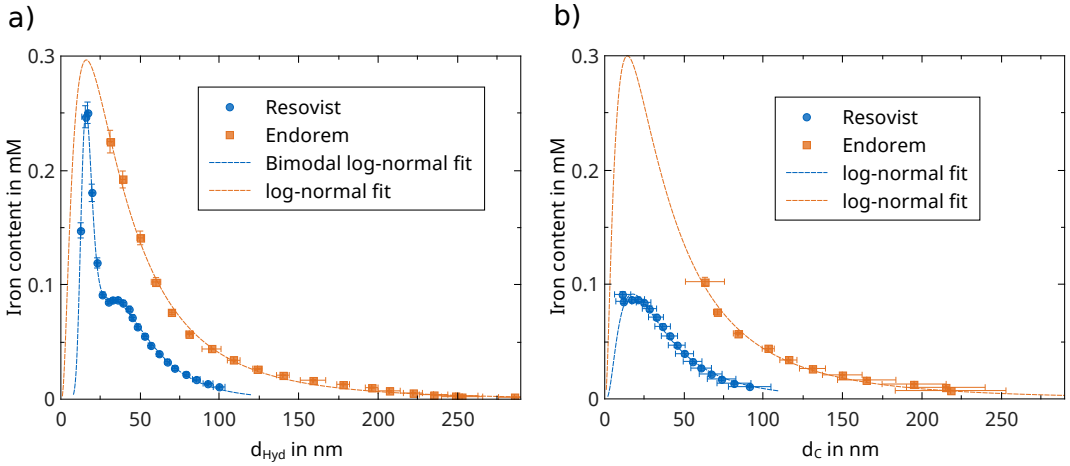

Figure 4.3.: a) Hydrodynamic (z-average) and b) core size distribution determined by DLS and MALS analysis of the fractions. First published in [11].

4.3.6. Iron Analysis

Iron quantification was conducted by means of an UV detector (PN3211, Postnova Analytics GmbH, Germany; λ = 280 nm). To directly quantify the iron content using the UV signal, calibration runs with MNPs of different sizes were performed.

4.4. Results and Discussion

4.4.1. Size Distributions

Hydrodynamic (d_{Hyd}) and core diameter (d_C) both linearly increased with fraction number for both particle systems. The hydrodynamic sizes of the fractions combined with the iron quantification yield the size distributions as shown in Figure 4.3 a. The polydispersity index of all fractions was around 0.1. The distribution of the Endorem®fractions was fitted with a log-normal function. If the assumption of a log-normal distribution is correct, the smallest fractions with the highest iron content were not collected after A4F. For Resovist®, the presence of a bimodal distribution of size was confirmed [121]. In general, the Endorem®particles are bigger than the Resovist®particles.

The distributions of the core sizes of the fractions are shown in Figure 4.3 b. Note that the lower size limit of MALS is around $d_{\mathrm{C}} \approx 20$ nm. Both distributions were fitted with a log-normal function. For the Resovist®fractions, d_{C} was smaller than d_{Hyd}, enabling the derivation of a shell thickness of about 6.5 nm. For the Endorem®fractions, the two size

parameters were the same within the measurement uncertainty which indicates that the shell thickness is negligible compared to the overall particle size.

4.4.2. Relaxivities

The results of the relaxation rate measurements for Resovist® are shown in Figure 4.4 a. Since the iron content of the size fractions differs, the relaxivities are shown here to be able to compare the relaxation effect of the fractions. The theoretical predictions for the relaxation rates can be rewritten for the relaxivities as well [109]. Both relaxivities exhibit a strong dependence on the hydrodynamic size. For smaller MNPs, r_2 and r_2^* are very similar and increase with increasing particle size. This is in accordance with the motional averaging regime or outer sphere theory (Equation 2.29). For larger nanoparticles, r_2 is considerably smaller than r_2^* and seems to reach saturation. This could be explained by the very short refocusing pulses (echo time 200 μs) already becoming effective and might indicate an early onset of the partial refocusing regime (Equation 2.31). The r_2^* trend for these MNPs is not so obvious because of the stronger scattering of the measured values. However, it can be safely stated that particles up to a diameter of 70 nm do not fulfill the condition of static dephasing because of the drastic increase of r_2^* relaxivities. With respect to iron content, these particles represent 88% of the unfractionated sample, which was calculated by integrating the bimodal log-normal function shown in Figure 4.3 a.

The results for Endorem® are shown in Figure 4.4 b and are essentially identical to those of Resovist®. For smaller MNPs, r_2 and r_2^* are similar and for larger particles, r_2 saturates. Despite the larger sizes of the Endorem® fractions compared to Resovist®, no saturation of r_2^* is observable within the measurement uncertainty. Particles up to a diameter of at least 150 nm fall into the motional averaging regime and thus do not meet the static dephasing condition. These particles represent 93 % of the unfractionated sample. r_2 seems to slightly decrease for the largest fractions which would be a strong indicator for the partial refocusing regime. However, this drop is close to the significance threshold.

As mentioned in Section 4.3.5, the relaxation rate measurements were repeated several times after inserting the samples into the magnet. The change of relaxation rates within one minute turned out to be less than 3% for R_2^* and less than 5% for R_2. The values shown in Figures 4.4 a and b were obtained within 10 seconds after inserting the samples and can therefore be considered reliable.

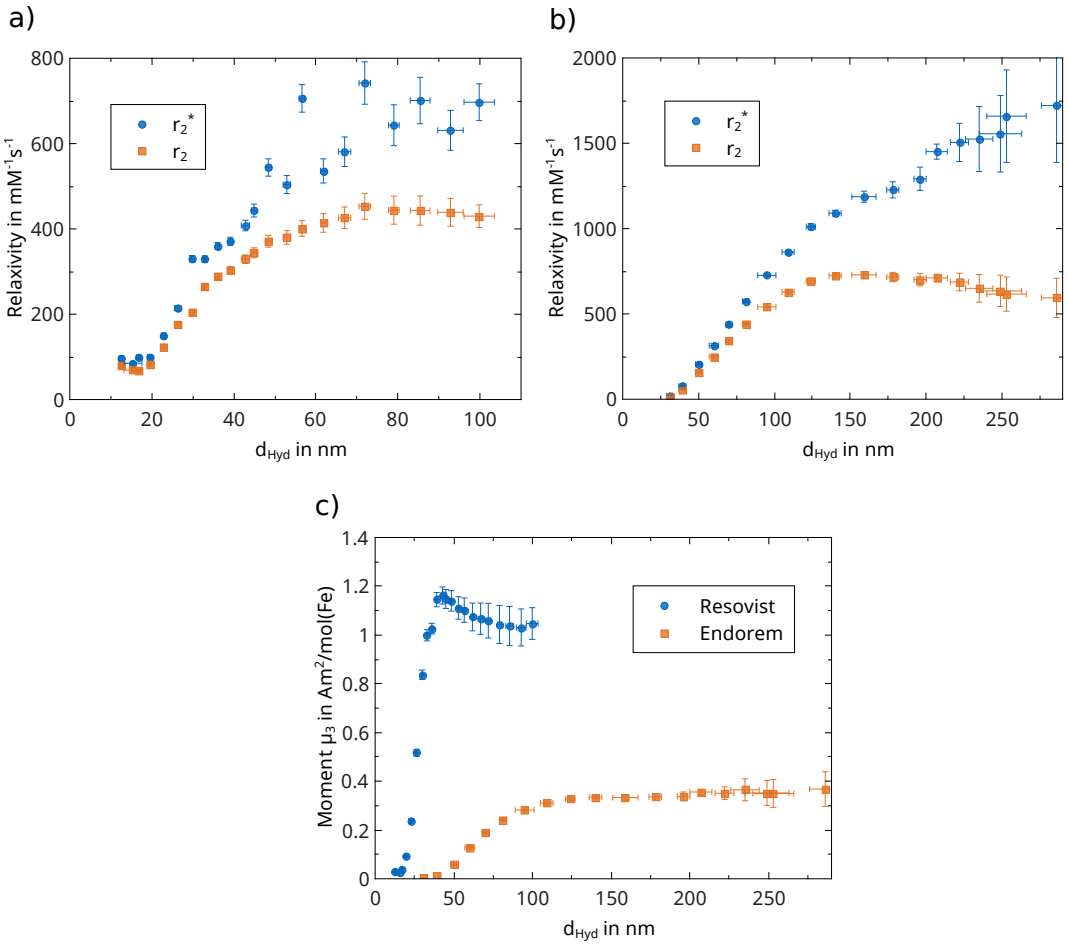

Figure 4.4.: a) MR relaxivites of the size fractionated Resovist® and b) Endorem® particles; c) Spectral moment μ_3 of the fractions as determined by magnetic particle spectrometry and normalized by the iron content. d_{Hyd} represents the z-average. First published in [11].

Due to the complex multi-core structure of the magnetic nanoparticles investigated here, the measured relaxivities could only be qualitatively explained by the analytical equations given in Section 4.1. Complications may arise from the assumptions of the formulas presupposing uncoated spherical MNPs without size distribution. These assumptions are not applicable here. If the shell thickness is constant for all particle sizes as observed for Resovist®, the overall magnetisation M_{S} of a particle increases with increasing size. In return, a decreasing packing density of a multi-core particle reduces its content of magnetisable material. The overall magnetisation of a particle determines its stray field and thus the influence on the surrounding water protons, which in turn is responsible for MR relaxation. The MPS results indicate different magnetic structures of Resovist®and Endorem®fractions even at the same hydrodynamic size (see next section).

4.4.3. Magnetic Particle Spectroscopy

Figure 4.4 c shows the spectral moment μ_3 of the fractions as determined by MPS. There is a strong nonlinear MPS signal dependence on the particle size indicating different magnetic structures of the fractions. This is in accordance with other studies [114, 118]. There is a maximal spectral moment for Resovist®, while μ_3 of Endorem®saturates with increasing particle size. In addition, the spectral moment of Endorem®is much smaller than that of Resovist®. Since the size parameters of Endorem®are relatively big, the smaller spectral moment can be a result of the dipole-dipole interaction between the single cores within the multi-core structure. This interaction could also explain the drop of the spectral moment of Resovist®at bigger diameters.

The MPS spectral moment cannot directly by related to the particle magnetisation M_S relevant for MR relaxation because MPS measures the magnetic response of the MNPs to a sinusoidal excitation field at a frequency of 25 kHz. Models to describe the MPS signal behaviour of magnetic nanoparticles and extract magnetic parameters like M_S are a subject of ongoing research [122, 123].

4.4.4. Error Analysis

The x-axis uncertainties shown in all figures represent the uncertainty of the hydrodynamic size determination retrieved from 6 subsequent measurements of the same sample. The uncertainty of the MPS signal results from the standard deviation of the MPS signal obtained from 100 empty sample holder measurements. The uncertainties of the relaxivities have been calculated by uncertainty propagation and are mainly a result of the uncertainty of

the iron quantification. The uncertainties of the relaxation curve fitting are included, but negligible. There was no sign of systematic errors.

4.5. Conclusion

The combination of hydrodynamic fractionation, geometric and magnetic characterisation and MR relaxometry is ideally suited to characterise complex MNP systems with regard to quantitative MRI. The experiments presented here qualitatively confirm the outer sphere relaxation theory for small nanoparticles. It was shown that the majority of Resovist®and Endorem®particles do not meet the condition for static dephasing which is a precondition for reliable quantification based on MRI relaxometry. Thus, neither Resovist®nor Endorem®provide particle systems capable of reliable quantitative MRI, since potential size alteration strongly affects MNP relaxivity.

This new approach is expected to facilitate the choice of MNPs for quantitative MRI and to help clarifying the relationship between size, magnetism and relaxivity of magnetic nanoparticles in the future. MPS combined with methods for particle size analysis has the potential to reveal important particle properties of MNPs (such as M_S) provided that adequate models for the signal behaviour are available. MPS also allows for a direct control of the MPI performance of a particle system or its size fractions. Additional characterisation methods enabling the determination of morphology and packing density of multi-core MNPs, for example transmission electron microscopy or X-ray diffraction, are essential for a deeper understanding of the relaxation behaviour and could allow for a quantitative comparison of MR relaxation theories with relaxation measurements.

5. Multiparametric Characterisation of Magnetic Viral Complexes

This chapter deals with the experiments that were performed to investigate whether MRI relaxometry can be used to quantify the concentration of magnetic-viral complexes and to assess the binding or aggregation state of the particles. The experiments were conducted in cooperation with researchers from the Department of Experimental Oncology of the Klinikum rechts der Isar der TU München and the Physikalisch-Technische Bundesanstalt in Berlin. I performed all MRI related experiments and their data analysis myself and also carried out the last step of the MRI phantom construction. The contents of this chapter are currently being prepared for publication.

5.1. Introduction

One of the most powerful applications of magnetic nanoparticles is their use as carriers for magnetic drug targeting in cancer therapy [4, 5, 1, 124]. The particles can be chemically bound to different kinds of anticancer agents such as oncolytic viruses, resulting in so called magnetic-viral complexes. After injection, these can be assembled at the target location inside the body using an appropriately designed setup of magnets. This ensures that the agent only affects the target location. Due to the strong contrast enhancing properties of magnetic nanoparticles, the progress of a therapy based on magnetic drug targeting can be monitored non-invasively using MRI. Being able to quantify the particles and to tell whether the particles are still bound to the agent and whether they are inside or outside of a potential cancer cell would be greatly beneficial to therapy monitoring. In principle, this can be achieved by MRI relaxometry [6, 7, 8, 9]. It has been shown theoretically and experimentally that R_2^* could be used for quantification of MNPs if the condition of static dephasing is met while R_2 is sensitive to bindings and the formation of clusters. However, the relaxation behaviour of magnetic nanoparticles is very complex (inter alia, due to the size dependence, see Chapter 4) and cannot be easily predicted for a specific combination of particles and viruses.

The experiments described in the following were designed to test and confirm whether MRI relaxometry is able to quantify the concentration of magnetic-viral complexes and to reveal whether the particles are bound to the viruses and inside the cancer cells. As a model system, two types of core-shell iron oxide nanoparticles were assembled with adenoids and vesicular stomatitis virus and transfected into human pancreatic carcinoma cells and rat Morris hepatocellular carcinoma cells. The samples were also characterised using magnetic particle spectroscopy and magnetometry. The information that can be gained from these additional techniques is especially valuable since they detect the magnetism of the particles and their interactions directly, whereas MRI just detects their effect on the proton spins. The combination of all three techniques therefore allows for a comprehensive understanding of the model system.

Initially, it was planned to conduct the MRI relaxometry experiments at three different fields (1, 3 and 7 Tesla) in order to find the optimal flux density for MNP quantification. Due to severe artifacts and technical problems, the experiments could either not be performed at all or the images could not be properly evaluated at 1 and 7 Tesla. Dealing with these issues was a major part of my PhD research and some of the problems will therefore be discussed in a separate section (Section 5.3.3). This will also enable other researchers to benefit from my experiences.

5.2. Materials

All samples were prepared by Olga Mykhaylyk at the Department of Experimental Oncology of the Klinikum rechts der Isar der TU München, essentially as described previously [125, 126, 127]. Therefore, just a brief summary will be given here.

5.2.1. Particles, Complexes and Cell Labelling

The core-shell iron oxide nanoparticles were synthesised by precipitation of Fe(II)/Fe(III) hydroxide from an aqueous solution of Fe(II) and Fe(III) salts. Coating with 25-kDa branched polyethylenimine (PEI) and the fluorinated surfactant Zonyl-FSA yielded PEI-Mag2 nanoparticles. These particles had a mean core diameter d_{C} of about 9 nm and a mean hydrodynamic diameter d_{Hyd} of 28 ± 2 nm. The second type of core-shell iron oxide particles was produced by initially coating with a silicon oxide layer with surface phosphonate groups resulting from the condensation of tetraethyl orthosilicate (TEOS) and 3-

(trihydroxysilyl) propylmethylphosphonate (THPMP). Subsequently, these particles were decorated with PEI in order to prepare them for binding to the negatively charged virus particles. The second type of particles will be called SO-Mag6 in the following and their size parameters were $d_{\mathrm{C}} \approx 6.7\,\mathrm{nm}$ and $d_{\mathrm{Hyd}} = 76 \pm 27\,\mathrm{nm}$. The core sizes were determined from X-ray diffraction data using the Scherer formula [128] and the hydrodynamic sizes were measured through DLS using a Malvern 3000 HS Zetasizer (Malvern Instruments Ltd., UK). The dry weight and the iron concentrations of the particle stock solutions were determined as described in [126].

The Ad complexes were prepared by assembling the nanoparticles with the adenovirus (Ad) in $\mathrm{ddH_2O}$/PBS and mixing at an iron-to-physical virus particle (VP) ratio of 5 fg Fe/VP. The YB-1 dependent oncolytic adenovirus Ad520 replicates in cancer cells with an elevated YB-1 expression. Similarly, the VSV complexes were prepared by assembling the MNPs with vesicular stomatitis virus (VSV) in $\mathrm{ddH_2O}$/PBS and mixing at a iron-to-infectious particle (IP) ratio of 500 fg Fe/IP. VSV is a negative-stranded RNA virus which is nonpathogenic in humans, but specifically replicates in interferon deficient tumor cells.

The Rat Morris hepatocellular carcinoma McA-RH7777 (McA) cells were labelled with both particle types using 10 pg iron/cell and infected with the corresponding magnetic-VSV complexes at a multiplicity of infection (MOI) of 20. Subsequently, magnetofection was performed by applying a magnetic field to the flasks and incubating for 1 hour at 37 °C. In the same way, the CAR-deficient multi-drug-resistant human pancreatic carcinoma EPP85-181RDB (RDB) cells were labelled with both MNP types by applying 25 pg iron/cell and infected with the corresponding magnetic-Ad complexes at a MOI of 120. Magnetofection was performed for 30 minutes. The iron loading of the cells was determined using a modification of the method of Torrance and Bothwell [129]. Essentially, the cells were put into an acidic mixture to break up the iron followed by iron analysis through a colorimetric method.

For every combination of particles, viruses and cells, four different types of samples were produced: Freely suspended MNPs, MNP-virus complexes, MNP labelled cells and cells infected with the MNP-virus complexes. Transmission electron microscopy (TEM) images of the suspended MNPs, the complexes and the magnetically labelled and infected cells can be found for both MNP, virus and cell types in [125].

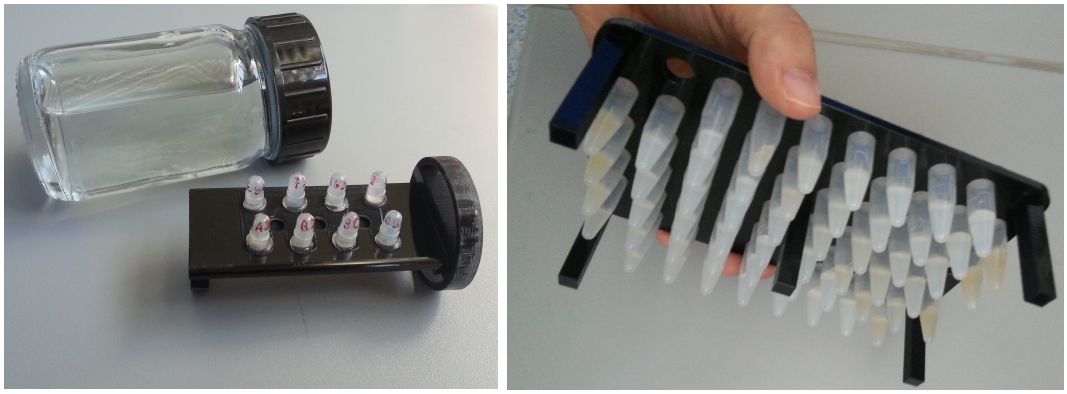

Figure 5.1.: Left: small sample holder with some PC tubes attached and its water filled container; right: large sample holder with about half of the Eppendorf tubes

5.2.2. Phantoms for MRI, MPS and Magnetometry

In order to determine the MRI relaxivities and a potential influence of dilution on the particle/complex stability, a dilution series of all samples was prepared using water for free MNPs and PBS for free MNP-virus complexes and magnetically labelled and infected cells. To prevent further aggregation of the particles and the magnetic-viral complexes (especially inside the field of the MRI scanners), the samples were fixed with 2.5 % (final concentration) agarose. For this purpose, the sample solutions were vortex-mixed with to 60 °C prewarmed agarose gel to distribute the material homogeneously and carefully pipetted into the designated sample containers while trying to avoid air bubbles. The containers were then left for slowly cooling down to room temperature, closed and sealed with parafilm to avoid water evaporation. For preservative purposes, 0.5 % (final concentration) of sodium azide was added to all samples.

The samples were prepared using two different types of containers: small vials for MPS (called PC tubes), magnetometry and MRI measurements with a sample volume of about 100 µl and 1.5 ml Eppendorf tubes just for MRI with a sample volume of about 0.5 ml. The total number of samples was 240, counting both types of containers and including a few control samples consisting of either cells in PBS and agarose or just PBS and agarose. For the last step of the MRI phantom construction, two different types of sample holders were printed using a 3D printer (Objet Eden260V, Stratasys Ltd, USA). The PC tubes were attached to their sample holders using hot glue, while the Eppendorf tubes were just inserted into the designated holes of their holder. Both sample holders were subsequently put into appropriately sized containers filled with $\mathrm{ddH_2O}$ in order to avoid susceptibility artifacts.

The two types of holders together with some of the samples are shown in Figure 5.1. The smaller holder and its container were chosen so that they fit into the bore of the 1 Tesla scanner, which is the smallest of the three scanners, and would not exceed the sensitive area of the coil either. The sample holders were constructed in such a way that there was enough distance between individual tubes to prevent the signal extinction caused by one tube (due to the high MNP concentrations) from affecting the signal of the neighbouring tube.

5.3. Methods

The MPS and magnetometry measurements were carried out at the Physikalisch-Technische Bundesanstalt in Berlin. For more details on the methods, please refer to Chapter 2.

5.3.1. Magnetic Particle Spectroscopy

MPS was performed at room temperature with the PC tube samples using a commercial magnetic particle spectrometer (MPS-3, Bruker BioSpin, Germany). During an MPS measurement, the sample is exposed to an oscillating magnetic field (25mT, 25kHz). Due to the non-linear magnetisation curve of superparamagnetic particles, the response of the sample is not a simple sinusoidal oscillation of the magnetisation, but contains contributions from higher harmonics with amplitudes A_3, A_5 and so on. These are detected by the spectrometer using a receive coil and Fourier transforming the signal. A_3 is mainly used for quantification, while the ration A_5/A_3 can be used to identify differences in the magnetic interactions within the particles themselves and among MNPs in clusters.

5.3.2. Magnetisation Measurements

In addition to the dynamic magnetic characterisation by MPS, the M(H) curve was measured as well with a commercial magnetometer (MPMS, Quantum Design). The M(H) curve represents the quasistatic response of the sample magnetisation in an external magnetic field and can also reveal information about the magnetic interaction among the particles. The measurements were performed at room temperature with the two types of particles in water and PBS and with the magnetic viral complexes in PBS, as well as with freeze dried particles.

5.3.3. MRI - Artifacts and Technical Problems

The original intention was to acquire R_1, R_2 and R_2^* maps with three different MRI scanners: Aspect M2 1 Tesla (preclinical, Aspect Imaging, Shoham, Israel), GE MR750w 3

Tesla (clinical, GE Healthcare, Chicago, USA), Agilent 7 Tesla (preclinical - using GE Firmware, Agilent Technologies, Santa Clara, USA). In order for the results to be comparable among the three different scanners, the exact same samples (small sample holders) and the same sequences with the same sequence parameters had to be used on all of them. Considering the large number of samples and the generally longer scan times needed for quantitative scans, fast (multi-echo) sequences had to be used and the parameters had to be well optimised. In the following, some of the problems that arose during the development of the scan protocols will be discussed. The issues have been categorized according to their suspected cause. A short review of standard MRI artifacts can be found in Chapter 2.3.5.

Susceptibility

Susceptibility artifacts are caused by abrupt changes in susceptibility, most commonly at air-water interfaces, and mainly affect gradient echo sequences. They appear as strong signal extinctions that are very difficult to distinguish from the signal extinction caused by magnetic nanoparticles in R_2 and R_2^* weighted images, which is why they corrupt the MNP quantification by MRI relaxometry. The susceptibility artifacts were particularly severe at 7 Tesla due to the high flux density, but could be minimised by embedding the sample holders in water. However, the small PC tubes are especially prone to artifacts caused by air bubbles because of their small size. For the larger Eppendorf tubes, the effect of the air bubbles could be minimised by evaluating just the center of the tubes. Using degassed water mostly prevented the formation of air bubbles, but the degasification had to be performed repeatedly because air continuously dissolves in water. In some of the tubes (for both types) water had already evaporated before the start of the experiments, probably due to incomplete sealing, which rendered the evaluation of those tubes very difficult and sometimes impossible.

In addition to the problems with standard susceptibility artifacts, strong distortions were sometimes observed in the gradient echo images acquired with the Aspect scanner (see Figure 5.2). These distortions were not consistent and seemed to appear randomly at long echo times. Despite consultation with the manufacturer's support, the problem could not be resolved and neither could the exact cause be determined, but it was speculated that the distortions were somehow related to susceptibility.

Permanent Magnet

The Aspect scanner employs a permanent magnet to create the B_0 field. This leads to problems that are not encountered in scanners using superconducting magnets. First, the

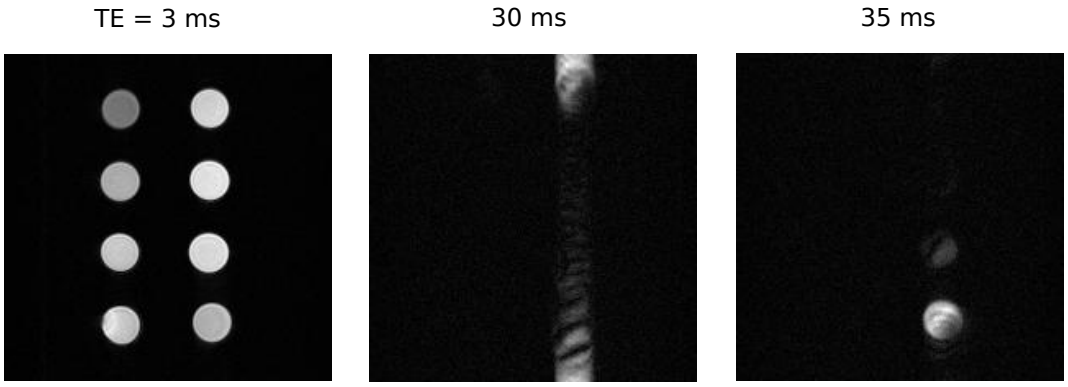

Figure 5.2.: Strong signal distortion at $T_{\mathrm{E}} = 30$ ms in the coronal image of eight tubes containing different MNP solutions. Acquired at 1 Tesla with a 2D gradient echo sequence using the following parameters: matrix 200 x 200, FOV = 70 mm, TH = 3 mm, $T_{\mathrm{R}} = 200$ ms, α = 65°, N_{acq} = 1 and horizontal frequency direction.

Larmor frequency drifts at a rate of about 1-2 Hz/s due to temperature fluctuations of the magnet. This frequency drift is usually linear over a timespan of several hours, according to the manufacturer's support. As a result of the drift, the excitation frequency has to be calibrated before each scan. However, the frequency drift during the acquisition can cause severe aliasing artifacts in the frequency direction for longer repetition times when using gradient echo sequences (see Figure 5.3). This basically renders gradient echo scans with long T_{R}s impossible, unless a drift compensation during the acquisition is performed. After a few hours, the frequency has usually drifted to such an extent, that the RF coil has to be tuned again. This means that manual interaction with the scanner is required every few hours making overnight scans impossible.

A second problem resulting from the use of a permanent magnet is that the gradient coils imprint small residual magnetisations on the B_0 magnet, which can persist for hours. These magnetisations cause a field inhomogeneity that depends on the sequence and the sequence parameters. In order to avoid field inhomogeneity artifacts, the desired sequence (with the desired parameters) has to be run several times first to enable a stationary formation of the residual magnetisations. Subsequently, the field has to be shimmed again before the actual scan can be started.

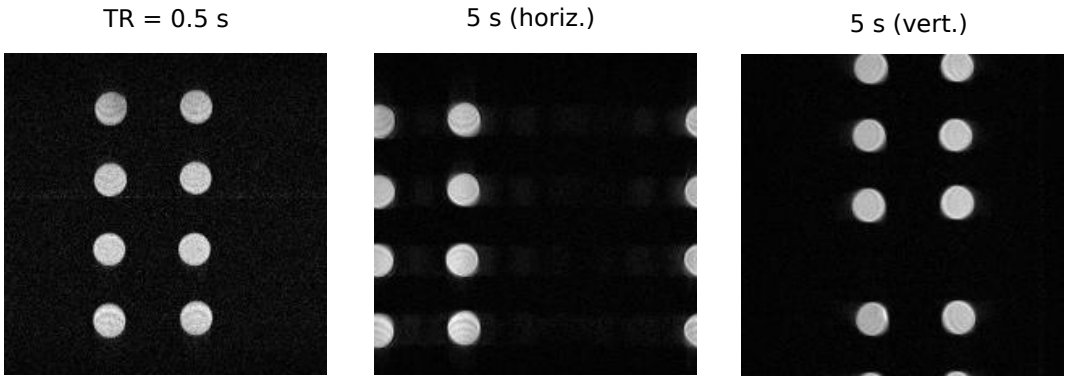

Figure 5.3.: Strong aliasing artifact at $T_{\mathrm{R}} = 5$ s in the coronal image of eight tubes containing water. Acquired at 1 Tesla with a 2D gradient echo sequence using the following parameters: matrix 200 x 200, FOV = 70 mm, TH = 3 mm, $T_{\mathrm{E}} = 3$ ms, α = 80°, N_{acq} = 1 and two different encoding directions.

Sequence Design

The inversion recovery (IR) sequences that were used to acquire R_1 maps on the 3 and 7 Tesla scanners only allowed inversion times of up to 4 s. Since the samples had T_1 times between 1 and 2 s, this was hardly sufficient to allow for a precise determination of the relaxation rates. In addition, there was no fast R_1 mapping sequence such as a Look-Locker sequence available on the 3 Tesla GE scanner which would have been very beneficial for decreasing scan times. The Look-Locker sequence available on the 7 Tesla system was in a testing state and very cumbersome to use.

The standard sequence for fast R_2 mapping is the multi-echo spin echo (MESE) sequence, which was available as a 2D version on the 3 and 7 Tesla systems and as a 3D version on the 1 Tesla scanner. However, the three systems produced different and strong artifacts in the MESE images that effectively made the use of these sequences impractical. The artifact produced by the Aspect system presents itself as broad black vertical stripes emerging at longer echo times (see Figure 5.4). The images were acquired with the small container filled with water. The cause of this artifact could not be determined and according to the manufacturer's support, it was not present on their own system. The artifact produced by the MESE sequence of the 7 Tesla system is shown in Figure 5.5 a. It looks similar to a ghosting artifact, but movement of the sample due to the system's vibrations could be ruled out. The artifact strongly distorts the signal intensities of the individual tubes, rendering a quantitative evaluation of the data useless. The problem could not be resolved and the cause

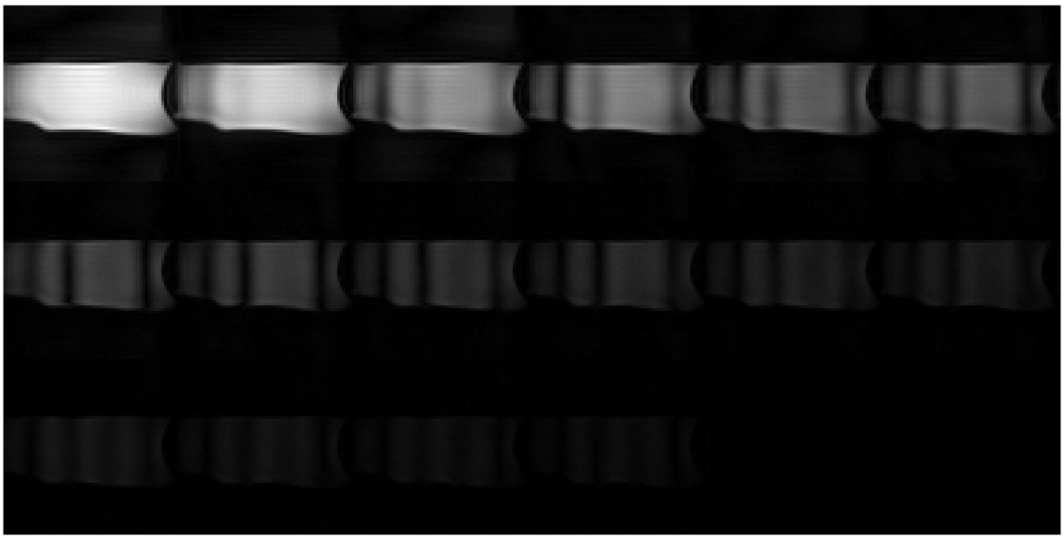

Figure 5.4.: Artifact in a series of sagittal 3D MESE images of the small ($CUSO_4$ doped) water container. Acquired at 1 Tesla using the following parameters: matrix 64 x 64 x 10, FOV = 85 mm, TH = 5 mm, N_{acq} = 1, 18 equidistant echoes with 20 ms separation.

of the artifact could not be found. In fact, the artifact appeared in all images acquired with multiple spin echoes including fast spin echo IR sequences. On the clinical 3 Tesla system, the relaxation curve acquired with the 2D MESE sequence showed a drop at the third echo (see Figure 5.5 b), which makes the quantitative evaluation of the data untrustworthy. A closer investigation revealed that this might be a result of the flip angles not always being set to 180°, presumably to decrease the SAR for clinical scans. Another explanation could be an incomplete optimisation of the sequence regarding stimulated echoes. This could also be a reason for the MESE artifacts on the other MRI systems.

For the purpose of fast R_2^* mapping, using a multi-echo gradient echo (MGE) sequence is indispensable. This sequence was available on the 3 and 7 Tesla systems, but not on the Aspect scanner, resulting in very long scan times. Together with the issues regarding the frequency drift, this rendered R_2^* mapping on the 1 Tesla system impractical.

Software and Data Evaluation

Initially, the R_2^* relaxation curves obtained from gradient echo acquisitions on the Aspect scanner did not show the expected exponential decay. When looking at the DICOM images from which the relaxation curves were extracted, the reason for this behaviour can easily

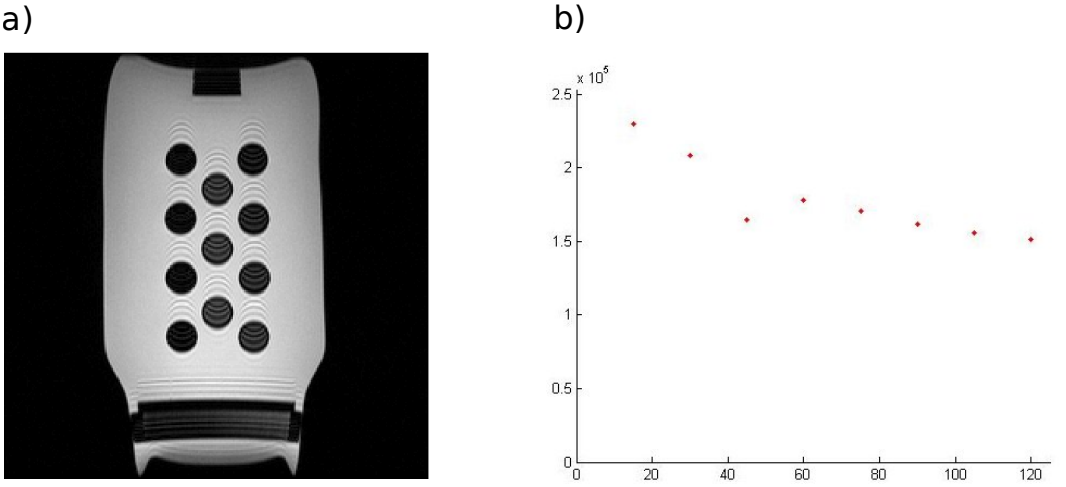

Figure 5.5.: a) Coronal image of the small container including 11 PC tubes; acquired with the 2D MESE sequence on the 7 Tesla system using the following parameters: matrix 192 x 192, FOV = 80 mm, TH = 1 mm, N_{acq} = 1, 8 equidistant echoes with 6 ms separation (12 ms image shown). b) Relaxation curve obtained from a ROI evaluation of a coronal 2D MESE acquisition on the 3 Tesla scanner (object: calibration phantom). Parameters: matrix 128 x 128, FOV = 25 cm, TH = 3 mm, N_{acq} = 1, 8 equidistant echoes with 15 ms separation

be spotted (see Figure 5.6): the noise level increases drastically with increasing echo time. This is a result of the acquisition software using different scaling for each image in order to preserve the full (16 bit) dynamic range of the DICOM images. Therefore, when performing quantitative evaluations based on the DICOM images produced by MRI scanners, the intensity values have to be divided by a scaling factor that is usually stored in the metadata of the DICOM files. For images acquired with multi-echo sequences, this is usually not necessary since the same scaling is used for all images of the echo train. Apparently, the GE 3 Tesla system does not use scaling factors.

Other problems involving scanner software include:

- The gradient echo sequence for R_2^* mapping on the 1 Tesla system always performs $N_{\mathrm{acq}} + 1$ scans, using the first scan for receive gain calibration. This resulted in even longer scan times. It could be avoided by setting the receive gain calibration to manual.

- Adjusting the slice orientation on the Aspect scanner using the two angles in the sequence parameters does not result in the correct slice orientation. Instead, the quick-

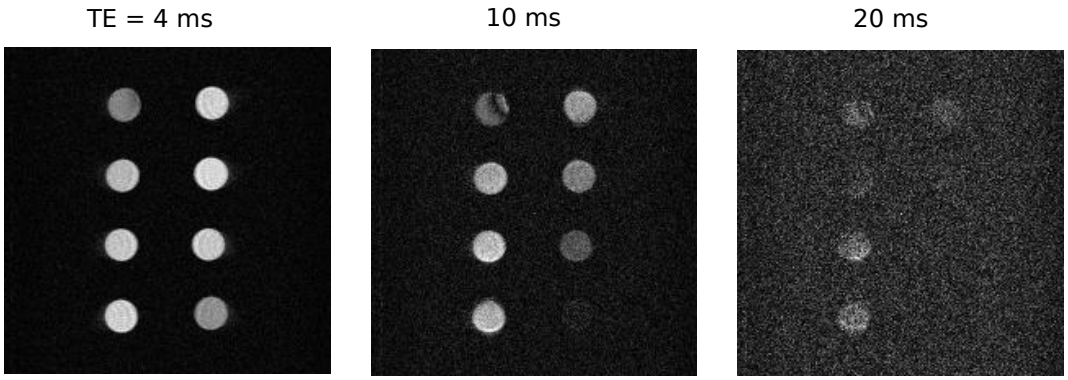

Figure 5.6.: Series of coronal 2D (single) gradient echo images of eight tubes containing different MNP solutions. Acquired at 1 Tesla using the following parameters: matrix 200 x 200, FOV = 70 mm, TH = 3 mm, $T_{\mathrm{R}} = 100$ ms, α = 50°, N_{acq} = 2

setup has to be used for this purpose by simply selecting axial/coronal/sagittal.

- In order to save scan time when imaging elongated samples, the smaller dimension is usually chosen for the phase encoding direction and the number of phase encoding steps is chosen to be smaller than the number of frequency encoding steps. In the GE software used by both the 3 and 7 Tesla systems, this can be achieved by selecting Phase FOV < 1. However, the number of frequency and phase encoding steps has to be chosen equally great if quadratic pixels are to be obtained. For example, if the matrix is set to 256 x 256 with FOV $= 8$ cm and Phase FOV $= 0.5$, the scanner will acquire an image with FOV $= 8$ cm $\times$ 4 cm and a 256 x 128 matrix.

5.3.4. MRI - Chosen Approach

As a result of the difficulties with the relaxometry experiments both at the 1 and 7 Tesla MRI systems, only the results obtained at 3 Tesla will be presented and discussed here. Due to the much larger bore of the 3 Tesla clinical scanner compared to the two other scanners, the larger 1.5 ml Eppendorf tubes could be used for the imaging experiments allowing for larger voxels - and consequently higher SNR - and less adverse effects from susceptibility artifacts. The general experimental approach is depicted in Figure 5.7. First, (half of) the samples were inserted into the holes of the black sample holder which, in turn, was put in a water filled container. This container was subsequently placed inside the head coil of the 3 Tesla MRI. The images for R_1 quantification were acquired using a inversion recovery sequence with two spin echoes for readout (ETL = 2) and the following sequence parame-

ters: matrix 128 x 128, FOV = 20 cm, Phase FOV = 0.6, slice thickness TH = 2.3 mm with coronal slice orientation, 3 slices with 3.8 mm gap, $T_{\mathrm{R}} = 7.5$ s, $T_{\mathrm{E}} = 6$ ms and N_{acq} = 1. Images were acquired with 16 different inversion times ranging between 50ms and 4000ms. Due to the problems with the MESE sequences, a single spin echo sequence was used for R_2 quantification with 19 different echo times ranging from 10ms to 160ms and otherwise identical sequence parameters as for R_1 quantification. For the quantification of R_2^*, a MGE sequence was used with 16 equally spaced gradient echoes ranging from 2.6 ms to 60.5 ms. While the geometrical parameters were the same as for the other two sequences, the other parameters were: matrix 256 x 256, $T_{\mathrm{R}} = 1$ s, $\alpha = 65°$ and N_{acq} = 16.

The images were subsequently evaluated by means of a self-programmed GUI in Matlab (The MathWorks Inc., Natick, MA, USA). First, the GUI was used to draw a ROI in an area without signal in order to determine the mean noise m_{air}. Second, the GUI was used to draw ROIs in the center of every sample in the coronal images to get the average signal intensity at every echo/inversion time and thereby increasing the SNR of the data evaluation as compared to the pixel-wise evaluation. The SNR of each sample for every sequence and slice was determined according to:

$$\mathrm{SNR} = S_{\max} / \sqrt{\frac{2}{\pi}} m_{\mathrm{air}} \ , \tag{5.1}$$

where $S_{\max}$ was the maximal measured signal intensity for that particular sample (see [130]). The relaxation curves were subsequently fitted using the three parameter fit for R_1 (see Equation 2.23) and a noise-corrected model for R_2 and R_2^* (see Equation 2.46):

$$S(T_{\mathrm{I}}) = A + Be^{-T_{\mathrm{I}} \times R_1}$$
$$S(T_{\mathrm{E}}) = \left[\left(Ae^{-T_{\mathrm{E}} \times R_2^{(*)}} \right)^2 + B^2 \right]^{1/2} \ .$$

Quality criteria were introduced for the fits as follows. Fit results not matching these criteria were discarded and not used for further analysis:

1. Coefficient of determination $R^2 > 0.99$
2. SNR > 5
3. At least 2 supporting points above noise level

All slices were evaluated and the slice that yielded the relaxation curve of highest quality was used for further analysis. This approach can be justified by susceptibility artifacts

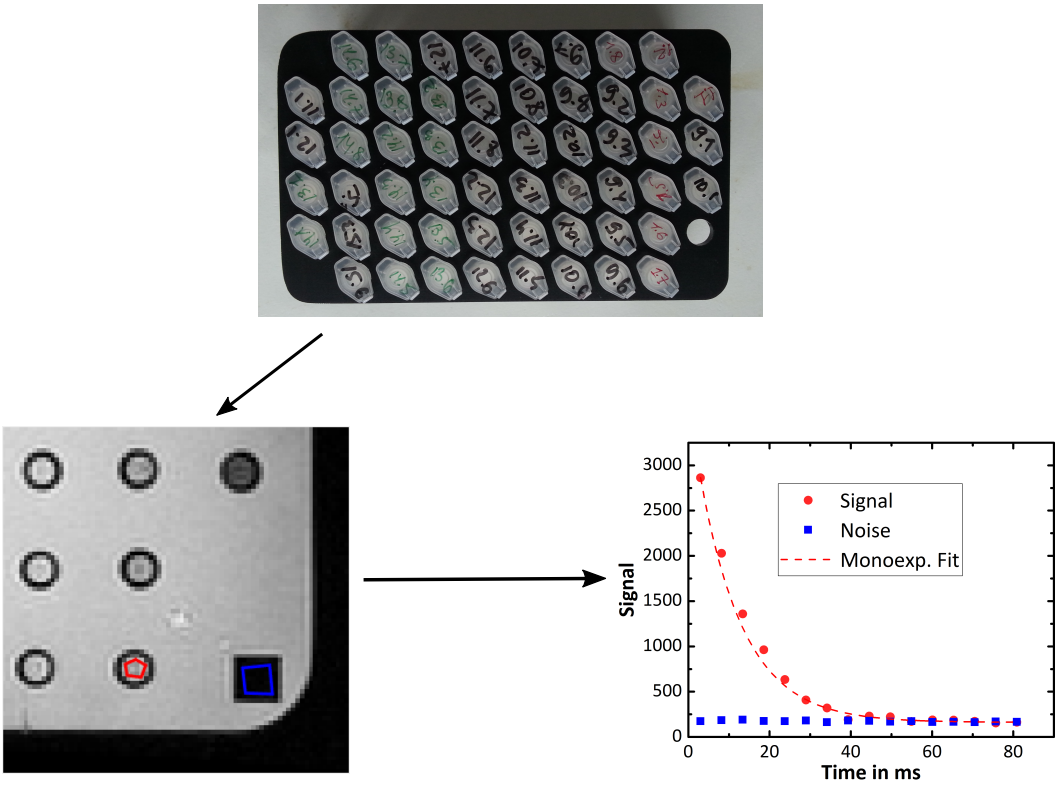

Figure 5.7.: Experimental approach for R_1, R_2 and R_2^* quantification: Eppendorf tubes are inserted into the sample holder (top) and images for are acquired. The images are subsequently evaluated by drawing red ROIs around the center of each tube to get the intensity values for the relaxation curves and a blue ROI in an area without signal for SNR determination (bottom left). The relaxation curves are fitted using Matlab to extract the relaxation rates and the SNR is calculated (bottom right).

corrupting the relaxation curves for slices close to an air-water interface. Finally, the relaxation rates were plotted against the iron content of every dilution series corresponding to a particular type of sample (MNPs in agarose, MNPs bound to viruses, MNPs in cells and MNPs bound to viruses in cells). These plots were linearly fitted - taking into account the uncertainty of each relaxation rate - using Qtiplot to get the relaxivities.

5.4. Results and Discussion

5.4.1. Magnetic Particle Spectroscopy

The results of the MPS measurements of all samples are shown in Figure 5.8. The amplitude of the third harmonic A_3 essentially depends linearly on the iron concentration of the samples and is largely independent of complex formation and cell incorporation with the VSV complexes being an exception. In general, the amplitudes of the SO-Mag6 particles are significantly higher than those of the PEI-Mag2 particles. The A_5/A_3 ratio, which is an indicator for the slope of the MPS spectrum and sensitive to a changing magnetic interaction among the particles, is mainly constant for samples containing more than 0.1 mM iron. This could be explained by assuming that particle clusters already form in the pure MNP (in water and agarose) samples. When larger complexes with the viruses are formed or the initial aggregates accumulate inside the cells, the magnetic dipole-dipole interaction among individual particles would only change for those sitting at the edge of a cluster. Lower concentrated samples, however, show higher deviations. This might be due to changed aggregate structures as a result of dilution.

5.4.2. Magnetisation Measurements

The results of the magnetisation measurements are shown in Figure 5.9. The data plotted in the top two diagrams was corrected by the magnetisation of the PC tubes and the diamagnetic magnetisation of the suspension medium (PBS). In the two bottom diagrams, the differences with respect to the magnetisation of the original particle suspensions (in water) were plotted. For better comparison, all M(H) curves were normalised at $H = 10^5$ A/m.

The differences in the M(H) curves of the measured samples shown in the top two diagrams are hardly noticeable. However, the difference curves shown in the bottom two diagrams reveal significant deviations at lower external fields. The PEI-Mag2 particles in PBS exhibit a 15% smaller magnetisation at fields below 10^4 A/m. This can be explained by stronger dipole-dipole interactions among the particles making them more resistive to alignment with the external field. The stronger dipole-dipole interaction in PBS is likely to be caused by the formation of particle clusters. The relative magnetisation drops even further for the magnetic-viral complexes, which indicates an even higher degree of cluster formation. This is not reflected to such an extent in the MPS measurements. At higher fields, the external field becomes stronger and overcomes the internal dipole-dipole interactions and the differences between the curves are mainly a result of the uncertainty of the iron content.

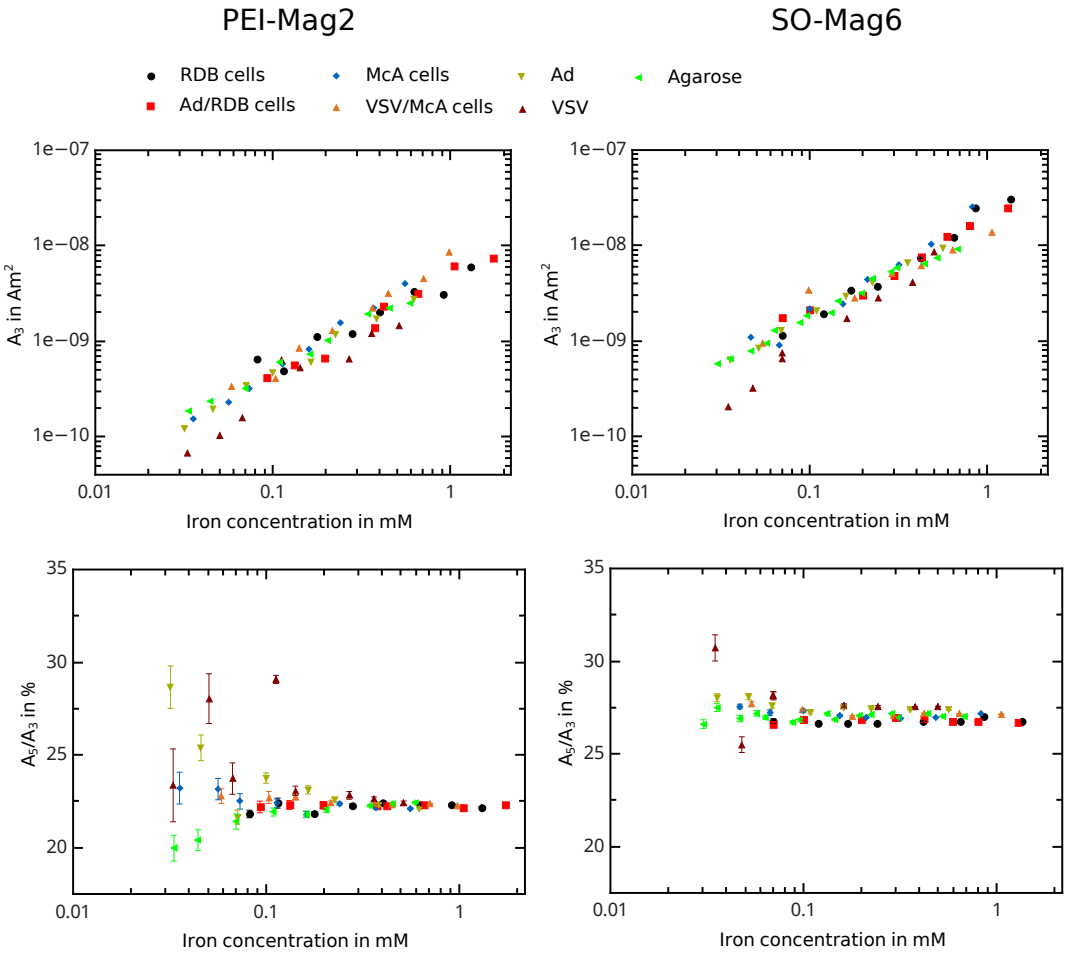

Figure 5.8.: Results of the MPS characterisation of all samples. While the amplitude of the third harmonic A_3 is plotted in the top two diagrams, the bottom two diagrams show the results of the ratio A_5/A_3, which is an indicator for the slope of the MPS spectrum.

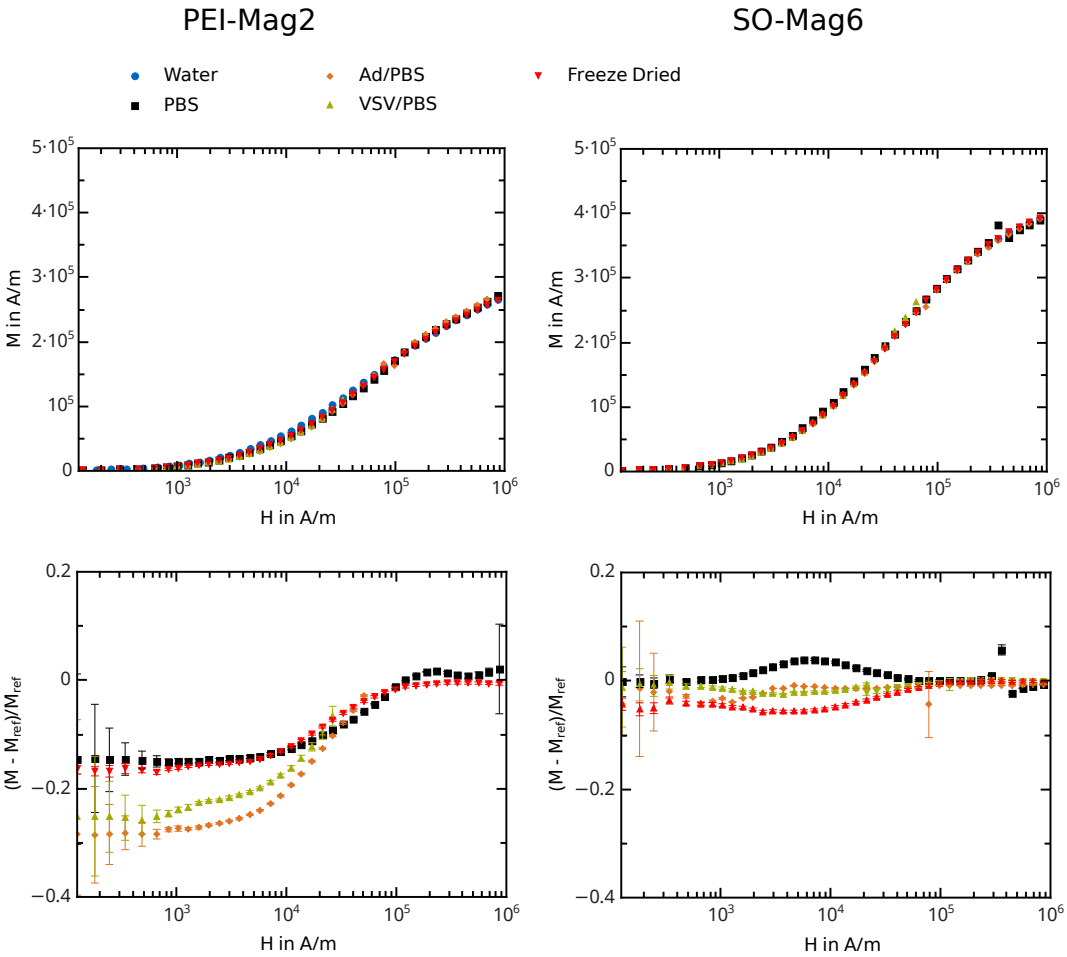

Figure 5.9.: Results of the magnetisation measurements. In the top two diagrams, the magnetisations of the (liquid) samples corrected by the magnetisation of the cuvette and the diamagnetic magnetisation of the suspension medium (PBS) are shown. The bottom two diagrams show the differences with respect to the magnetisation curve of the original (liquid) particle suspensions.

The differences in magnetisability for the SO-Mag6 particles are much smaller. This is either a result of little cluster formation or the clusters already formed in the original suspension medium (water), which would confirm the MPS results.

5.4.3. MRI Relaxometry

The results of the MRI relaxometry experiments are presented in Figure 5.10 for the PEI-Mag2 particles and in Figure 5.11 for the SO-Mag6 particles. The two figures show the relaxation rates R_1 (top), R_2 (center) and R_2^* (bottom) for all combinations of particles, viruses and cells. Each diagram shows the relaxation rates for the dilution series of four different types of samples: MNPs in agarose, MNPs bound to viruses, MNPs in cells and MNPs bound to viruses in cells. The diagrams also show the linear fits of the relaxation rates of each dilution series and the resulting relaxivities are summarised in Table 5.1.

As expected, the relaxation rates mostly increase linearly with increasing iron concentration, which allows for reliable determinations of sample relaxivities. The r_1 relaxivities show a very similar behaviour for both particle systems. When the particles form complexes with the adenovirus, the r_1 relaxivities are slightly lower than for the samples containing just MNPs in agarose, but r_1 drops drastically when the particles or the MNP-viral complexes are incorporated by the RDB cells. The r_1 relaxivities are radically lower for all combinations of MNPs, VSV virus and McA cells compared to the samples containing just MNPs in agarose. R_1 relaxation rates therefore appear to be sensitive to aggregation and cell incorporation. The qualitative behaviour is identical for the r_2 relaxivities for both particle systems. The drop in R_2 rates as a result of complex formation and cell incorporation could be explained by the mechanism of partial refocusing (see Section 2.2.4). The absolute r_2 relaxivity values, however, are greater by a factor of more than 100, which shows that PEI-Mag2 and SO-Mag6 particles are mainly $T_2^{(*)}$ contrast agents.

The r_2^* relaxivities are considerably higher than the r_2 relaxivities, especially for the SO-Mag6 particles. For the combination of MNPs with adenovirus and RDB cells, the r_2^* relaxivities are very similar, whereas they are a bit more erratic for the combination of MNPs with VSV virus and McA cells. In general, the R_2^* relaxation rates are much more independent of complex formation and cell incorporation than the other two relaxation rates, which could be explained by the static dephasing regime theory (see Section 2.2.4).

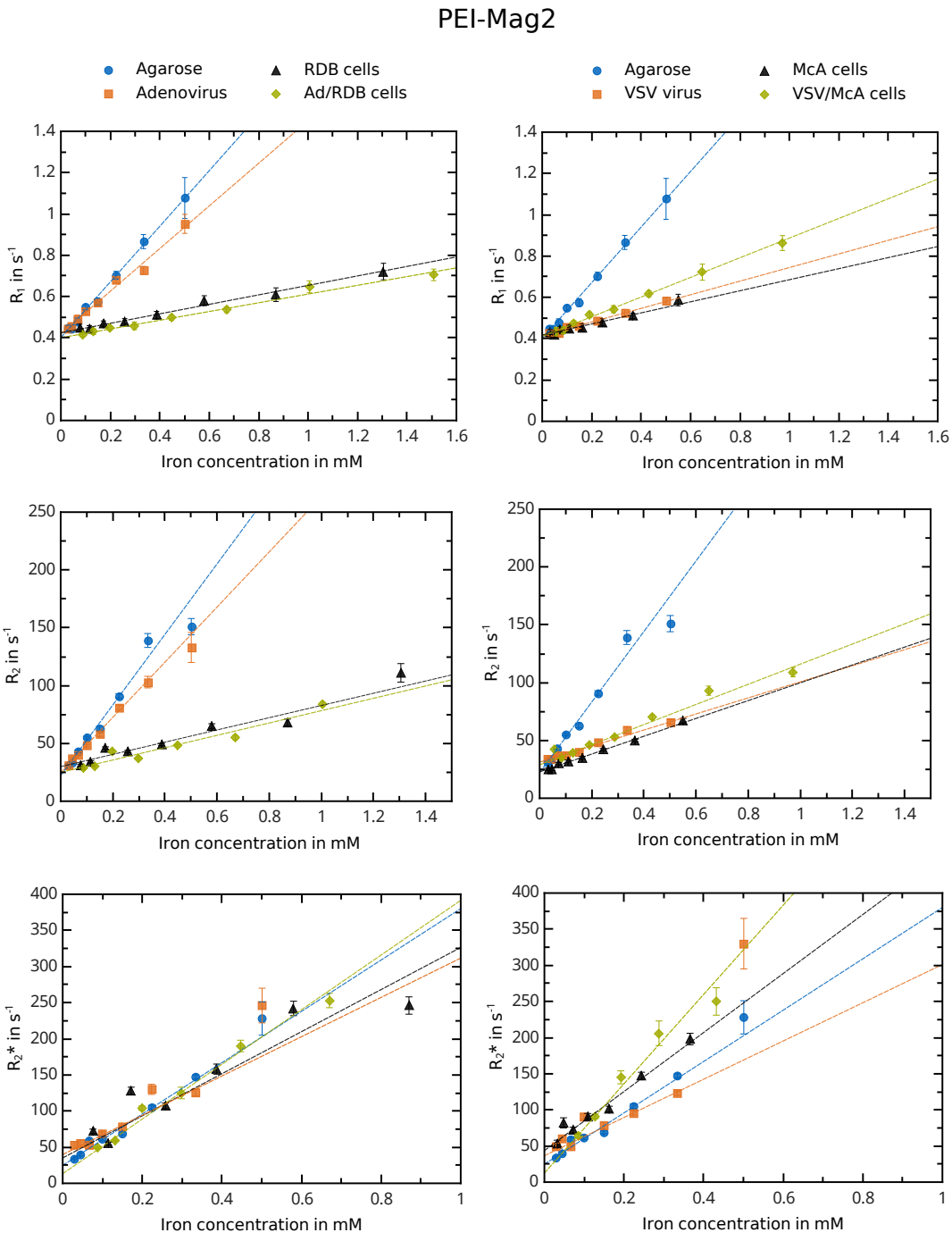

Figure 5.10.: Relaxation rates R_1 (top), R_2 (center) and R_2^* (bottom) for all combinations of PEI-Mag2 particles, viruses and cells including linear fits for each dilution series.

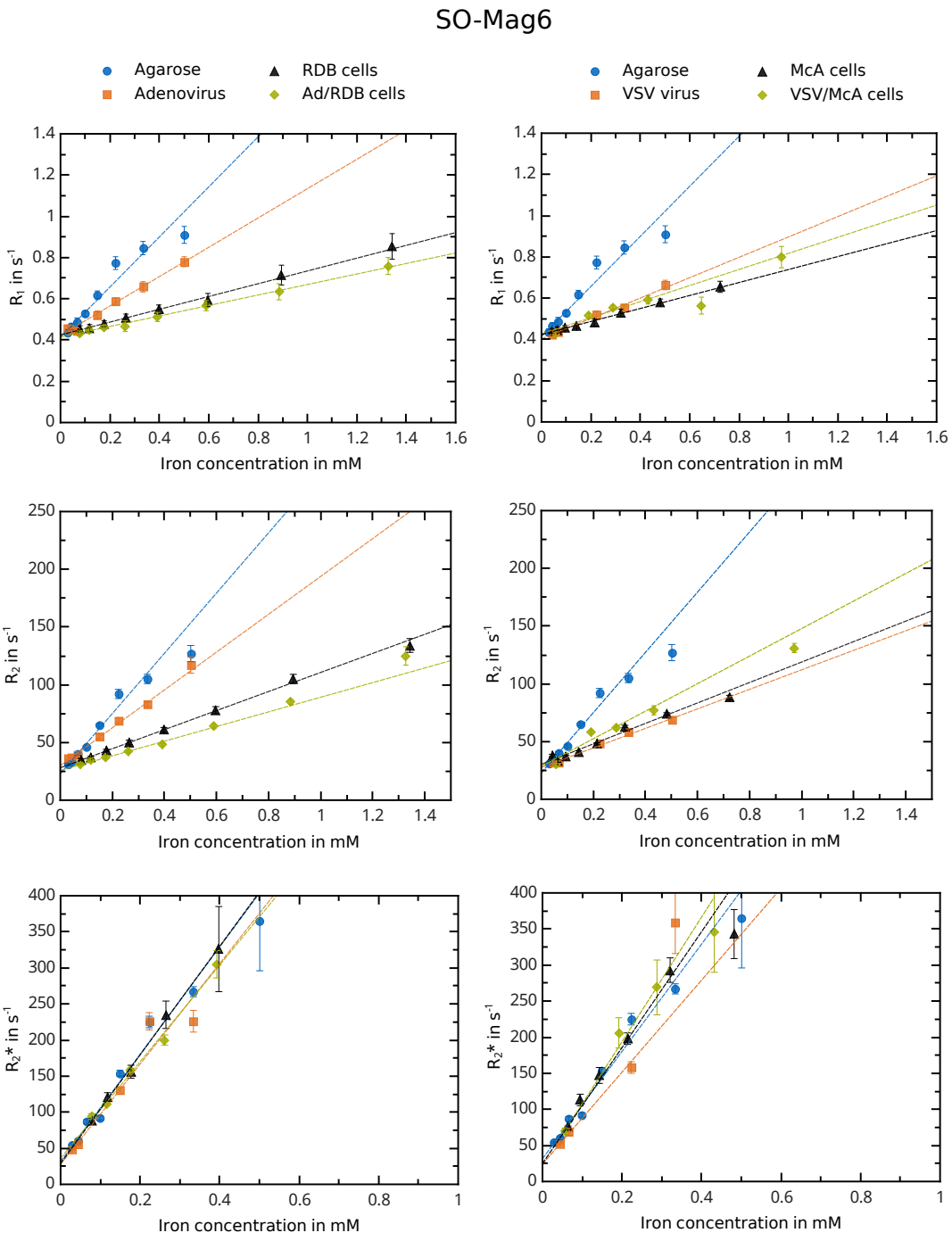

Figure 5.11.: Relaxation rates R_1 (top), R_2 (center) and R_2^* (bottom) for all combinations of SO-Mag6 particles, viruses and cells including linear fits for each dilution series.

Table 5.1.: Summary of the relaxivities for all types of samples resulting from the linear fits of the dilution series.

	PEI-Mag2		**SO-Mag6**	
	Ad/RDB	**VSV/McA**	**Ad/RDB**	**VSV/McA**
$\mathbf{r}_1[\mathrm{mM}^{-1}\mathrm{s}^{-1}]$				
Virus	1.03±0.05	0.33±0.04	0.71±0.05	0.49±0.05
Cells	0.23±0.03	0.27±0.04	0.31±0.03	0.31±0.03
Virus/Cells	0.21±0.02	0.48±0.03	0.25±0.03	0.39±0.04
Agarose	1.34±0.08	1.34±0.08	1.21±0.07	1.21±0.07
$\mathbf{r}_2[\mathrm{mM}^{-1}\mathrm{s}^{-1}]$				
Virus	238±8	70±4	164±6	85±4
Cells	53±3	77±3	83±3	89±2
Virus/Cells	53±2	88±3	64±2	119±4
Agarose	304±8	304±8	260±7	260±7
$\mathbf{r}_2^*[\mathrm{mM}^{-1}\mathrm{s}^{-1}]$				
Virus	272±17	265±10	696±29	635±43
Cells	292±11	408±21	750±66	800±36
Virus/Cells	378±12	617±42	669±30	863±92
Agarose	356±8	356±8	742±17	742±17

5.4.4. Error Analysis

The error bars in the top two MPS and M(H) diagrams were smaller than the size of the data points and are therefore not shown. The error bars in the diagrams showing the results of the MRI relaxometry represent the uncertainty of the relaxation curve fitting as provided by Matlab. Similarly, the error margins given in Table 5.1 correspond to the uncertainty of the linear curve fitting provided by Qtiplot, the fitting procedure of Qtiplot in turn already takes the uncertainty of the relaxation rates into account.

These fitting uncertainties, however, do not always represent the full uncertainty of the relaxation experiments. While the relaxation rates extracted from different slices are largely consistent for R_1 and R_2, the R_2^* values differed significantly between slices for most samples and some slices did not even allow for a proper exponential fit. This is a result of susceptibility artifacts due to air inside the Eppendorf tubes. For the results shown in Figures 5.10 and 5.11, the slices with the smallest fitting errors that also satisfied the quality criteria (see Section 5.3.4) were chosen and only those were used for the determination of the relaxivities. The R_2^* results should therefore be interpreted with care. Another issue may arise from water evaporation inside the Eppendorf tubes, distorting the iron content of the samples and therefore the relaxivities. With few exceptions (which were not used for further evaluation), the samples looked visually fine, but since the filling level of the samples differed already on delivery, some water evaporation cannot be ruled out completely.

5.5. Conclusion

The relaxation experiments showed that R_1 and R_2 rates are sensitive to aggregation and cell incorporation, while R_2^* measurements are more suitable for quantification of MNPs in biological systems. The R_1 rates of the two particle systems used here are too small to provide a good contrast, but a combination of R_2 and R_2^* measurements has the potential to allow for quantitative and non-invasive therapy monitoring for applications such as magnetic drug targeting. However, the two particle systems tested here already show some differences in the relaxation behaviour, which shows that the results cannot be simply transferred to other particle systems. Instead, each system of particles, viruses and cells has to be carefully and thoroughly characterised in-vitro before using relaxometry for therapy monitoring. In order to avoid problems arising from susceptibility artifacts, any air inside the test tubes has to be avoided. This is especially important for reliable R_2^* results. The second main problem regarding MRI relaxometry is the availability and the proper func-

tioning of the corresponding imaging sequences. Despite being standard methods in theory, multi echo sequences needed for fast relaxation rate mapping are often afflicted with artifacts or have considerable limitations in practise. M(H) and MPS measurements have been shown to provide valuable information about the magnetic properties and the aggregation behaviour of MNPs and MNP-virus systems. In contrast to MRI, these methods measure the particles directly and are therefore very important complementary techniques. In addition, MPS measurements also allow for an evaluation of the MPI performance of the samples.

6. Summary and Outlook

As stated in the introduction, in order to use MRI relaxometry for reliable and quantitative therapy monitoring for biomedical application such as magnetic drug targeting, it is essential to gather as much in-vitro information about the system of MNPs, target molecules and tissue as possible. The three experimental chapters comprised in this work deal with different aspects of MNP characterisation. The chapter on Mössbauer spectroscopy describes a new method for determining the magnetite fraction of small MNPs, which is an important quality control criteria for particle synthesis. Using an array of permanent magnets that magnetise the MNPs, well split Mössbauer spectra can be obtained from particles that would otherwise be too small to show significant hyperfine splitting.

Chapters 4 and 5 study the relaxation behaviour of MNPs. As a result of these investigations, the following advise can be given when a particular system of MNPs and target pharmaceutical molecules is to be used for treatment. First, the MNPs should be size fractionated and NMR relaxation measurements should be performed on all size fractions in order to test the suitability of the particles for quantification by R_2^* mapping. At the same time, other techniques such as MPS can be used to gain more information about the properties of the different fractions. Next, all combinations of MNPs, target molecules and cells have to be comprehensively characterised in-vitro by MRI relaxometry and at least one other independent method such as MPS in order to investigate the effect of the assembling of the MNPs with the target molecules and cell incorporation. This step is also necessary for calibration of the relaxation rates to be able to infer the particle concentration from the measured rates during therapy monitoring. In order to obtain reliable relaxation values, two crucial experimental requirements have to be met. First, the in-vitro samples, which usually use agarose to prevent aggregation of the MNPs in the field of the MRI, have to be produced in a way to avoid air-water interfaces. Second, fast and proper pulse sequences for R_1, R_2 and R_2^* mapping have to be available on the MRI system and those sequences have to operate without major imaging artifacts and without too many technical limitations with respect to minimum and maximum echo times and inversion times, for example. It should be kept in mind that relaxometry results obtained on one MRI system are not directly transferable

to other MRI systems, since the design of the pulse sequences and the parameters usually differ which results in different relaxation rates.

In the future, MRI relaxometry experiments should be extended to different B_0 fields in order to find the optimal flux density for therapy monitoring. To ensure comparability of the results, however, the same sequences and imaging parameters have to be used. MRI relaxometry can be accompanied by other quantitative MRI techniques such as quantitative susceptibility mapping, a post-processing method that uses the MRI phase data to calculate susceptibility maps. A major step for reliable therapy monitoring for drug targeting would be the combination of MRI and MPI. While MPI detects the nanoparticles directly but lacks anatomical contrast, MRI provides anatomical information and particle contrast. The results of MRI relaxometry and MPI detection of the nanoparticles can be correlated to obtain comprehensive information about the particles inside the targeted tissue. Another interesting project would be to evaluate the suitability of other standard particles used for quantitative imaging using the size fractionation approach.

A. Appendix

A.1. Abbreviations

A4F	asymmetric flow field-flow
Ad	adenovirus
BPP	Bloembergen, Purcell, Pound
CNR	contrast-to-noise ratio
CPMG	Carr, Purcell, Meiboom, Gill
DICOM	Digital Imaging and Communications in Medicine
DLS	dynamic light scattering
ETL	echo train length
FID	free induction decay
FLASH	fast low angle shot
FOV	field of view
FSE	fast spin echo
FT	Fourier transform
GUI	graphical user interface
IR	inversion recovery
LL	Look, Locker
MALS	multi-angle laser scattering
McA	Rat Morris hepatocellular carcinoma
MESE	multi-echo spin echo
MGE	multi-echo gradient echo
MNP	magnetic nanoparticle
MOI	multiplicity of infection
MPI	magnetic particle imaging
MPS	magnetic particle spectroscopy
MR	magnetic resonance
MRI	magnetic resonance imaging

NMR	nuclear magnetic resonance
PBS	phosphate buffered saline
PD	proton density
PEI	polyethylenimine
RARE	rapid acquisition with refocused echoes
RDB	human pancreatic carcinoma
RF	radio frequency
ROI	region of interest
SDR	static dephasing
SE	spin echo
SNR	signal-to-noise ratio
SQUID	superconducting quantum interference device
SR	saturation recovery
TEM	transmission electron microscopy
TEOS	tetraethyl orthosilicate
THPMP	3-(trihydroxysilyl) propylmethylphosphonate
TSE	turbo spin echo
UV	ultra violet
VSM	vibrating sample magnetometer
VSV	vesicular stomatitis virus

A.2. Parameters

Vectors are written in bold.

α	flip angle	R^2	coefficient of determination
B	magnetic flux density	R_1	longitudinal relaxation rate
B_0	MRI main magnetic field	$R_2^{(*)}$	transverse relaxation rate
BW_{read}	readout bandwidth	r_1	longitudinal relaxivity
D	(self) diffusion coefficient	$r_2^{(*)}$	transverse relaxivity
d_{C}	core diameter	S, m_{s}	spin quantum numbers
d_{Hyd}	hydrodynamic diameter	$\rho_{(\mathrm{eff})}$	(effective) spin density
η	viscosity	τ_{B}	Brown relaxation time
FOV	field of view	τ_{C}	correlation time
f	volume fraction	τ_{D}	diffusional correlation time
$G_{\mathrm{x,y,z}}$	x, y, z gradient	τ_{N}	Néel relaxation time
γ	gyromagnetic ratio	T	absolute temperature
H	magnetic field strength	T_{dwell}	dwell time
I	nuclear spin	T_{E}	echo time
K	magnetic anisotropy constant	TH	slice thickness
$k_{\mathrm{x,y,z}}$	spatial frequency	T_{I}	inversion time
k_{B}	Boltzmann constant	T_{R}	repetition time
m_{air}	mean noise level	T_{s}	sampling time
M	magnetisation	T_1	longitudinal relaxation time
M_{S}	saturation magnetisation	$T_2^{(*)}$	transverse relaxation time
μ	magnetic moment	V	volume
μ_0	magnetic constant	ω_0	Larmor frequency
N_{acq}	number of acquisitions	ω_1	frequency of RF field
N_{Ion}	number of ions per cm^3	$\Delta\omega_{\mathrm{eq}}$	frequency shift at MNP surface
$N_{\mathrm{x,y,z}}$	number of encoding steps	$\Delta x, \Delta y, \Delta z$	voxel dimensions

Bibliography

[1] Q. A. Pankhurst, N. T. K. Thanh, S. K. Jones, and J. Dobson, "Progress in applications of magnetic nanoparticles in biomedicine.," *Journal of Physics D: Applied Physics*, vol. 42, p. 224001, 2009.

[2] B. Gleich, T. Weyh, and B. Wolf, "Magnetic Drug Targeting: An Analytical Model for the Influence of Blood Properties on Particle Trajectories," *Appl Rheol*, vol. 18, p. 52023, 2008.

[3] S. Laurent, S. Boutry, I. Mahieu, L. Vander Elst, and R. N. Muller, "Iron oxide based MR contrast agents: from chemistry to cell labeling.," *Curr Med Chem*, vol. 16, no. 35, pp. 4712–4727, 2009.

[4] A. S. Lübbe, C. Alexiou, and C. Bergemann, "Clinical Applications of Magnetic Drug Targeting," *Journal of Surgical Research*, vol. 95, pp. 200–206, feb 2001.

[5] C. Alexiou, R. J. Schmid, R. Jurgons, M. Kremer, G. Wanner, C. Bergemann, E. Huenges, T. Nawroth, W. Arnold, and F. G. Parak, "Targeting cancer cells: magnetic nanoparticles as drug carriers," *European Biophysics Journal*, vol. 35, pp. 446–450, may 2006.

[6] R. Weissleder, H.-C. Cheng, A. Bogdanova, and A. Bogdanov Jr., "Magnetically Labeled Cells Can Be Detected by MR Imaging," *J Magn Reson Imaging*, vol. 7, pp. 258–263, 1997.

[7] J. W. M. Bulte, I. D. Duncan, and J. A. Frank, "In Vivo Magnetic Resonance Tracking of Magnetically Labeled Cells After Transplantation," *Journal of Cerebral Blood Flow & Metabolism*, pp. 899–907, aug 2002.

[8] C. V. Bowen, X. Zhang, G. Saab, P. J. Gareau, and B. K. Rutt, "Application of the Static Dephasing Regime Theory to Superparamagnetic Iron-Oxide Loaded Cells," *Magn Reson Med*, vol. 48, pp. 52–61, 2002.

[9] O. M. Girard, R. Ramirez, S. McCarty, and R. F. Mattrey, "Toward absolute quantification of iron oxide nanoparticles as well as cell internalized fraction using multiparametric MRI," *Contrast Media Mol Imaging*, vol. 7, pp. 411–417, 2012.

[10] A. Joos, C. Rümenapp, F. E. Wagner, and B. Gleich, "Characterisation of iron oxide nanoparticles by Mössbauer spectroscopy at ambient temperature," *J Magn Magn Mater*, vol. 399, pp. 123–129, feb 2016.

[11] A. Joos, N. Löwa, F. Wiekhorst, B. Gleich, and A. Haase, "Size-dependent MR relaxivities of magnetic nanoparticles," *Journal of Magnetism and Magnetic Materials*, vol. 427, no. November 2016, pp. 122–126, 2017.

[12] I. I. Rabi, J. R. Zacharias, S. Millman, and P. Kusch, "A New Method of Measuring Nuclear Magnetic Moment," *Phys Rev*, vol. 53, p. 318, 1938.

[13] F. Bloch, "Nuclear Induction," *Phys Rev*, vol. 70, pp. 460–474, 1946.

[14] E. M. Purcell, H. C. Torrey, and R. V. Pound, "Resonance Absorption by Nuclear Magnetic Moments in a Solid," *Phys Rev*, vol. 69, pp. 37–38, 1946.

[15] A. Abragam, *Principles of Nuclear Magnetism*. Oxford University Press, 1961.

[16] M. H. Levitt, *Spin Dynamics*. John Wiley & Sons, 2008.

[17] L. G. Hanson, "Is Quantum Mechanics Necessary for Understanding Magnetic Resonance?," *Concepts Magn Reson A*, vol. 32A, pp. 329–340, 2008.

[18] E. Hahn, "Spin Echoes," *Phys Rev*, vol. 80, pp. 580–594, nov 1950.

[19] A. Joos, *NMR-Relaxometrie an magnetischen Nanopartikeln*. Diploma thesis, 2012.

[20] D. C. Look and D. R. Locker, "Time Saving in Measurement of NMR and EPR Relaxation Times," *Review of Scientific Instruments*, vol. 41, no. 2, p. 250, 1970.

[21] R. Deichmann and A. Haase, "Quantification of T1 values by SNAPSHOT-FLASH NMR imaging," *Journal of Magnetic Resonance (1969)*, vol. 96, pp. 608–612, feb 1992.

[22] H. C. Torrey, "Nuclear Spin Relaxation by Translational Diffusion," *Phys Rev*, vol. 92, pp. 962–969, nov 1953.

[23] H. Y. Carr and E. M. Purcell, "Effects of Diffusion on Free Precession in Nuclear Magnetic Resonance Experiments," *Phys Rev*, vol. 94, pp. 630–638, 1954.

[24] S. Meiboom and D. Gill, "Modified Spin-Echo Method for Measuring Nuclear Relaxation Times," *Review of Scientific Instruments*, vol. 29, no. 8, p. 688, 1958.

[25] M. Weigel, "Extended phase graphs: Dephasing, RF pulses, and echoes - pure and simple," *Journal of Magnetic Resonance Imaging*, vol. 41, pp. 266–295, feb 2015.

[26] P. B. Kingsley, "Signal Intensities and T1 Calculations in Multiple-Echo Sequences with Imperfect Pulses," *Concepts in Magnetic Resonance*, vol. 11, no. 1, pp. 29–49, 1999.

[27] N. Bloembergen, E. Purcell, and R. Pound, "Relaxation effects in nuclear magnetic resonance absorption," *Physical Review*, vol. 73, pp. 679–715, apr 1948.

[28] L.-P. Hwang and J. H. Freed, "Dynamic effects of pair correlation functions on spin relaxation by translational diffusion in liquids," *J Chem Phys*, vol. 63, pp. 4017–4025, nov 1975.

[29] Y. Ayant, E. Belorizky, J. Aluzon, and J. Gallice, "Calcul des densités spectrales résultant d'un mouvement aléatoire de translation en relaxation par interaction dipolaire magnétique dans les liquides," *Journal de Physique*, vol. 36, no. 10, pp. 991–1004, 1975.

[30] J. H. Freed, "Dynamic effects of pair correlation functions on spin relaxation by translational diffusion in liquids. II. Finite jumps and independent T1 processes," *J Chem Phys*, vol. 68, no. 9, pp. 4034–4037, 1978.

[31] A. Roch and R. N. Muller, "Longitudinal Relaxation of Water Protons in Colloidal Suspensions of Superparamagnetic Crystals," *Proceedings of the 11th Annual Meeting of the Society of Magnetic Resonance in Medicine*, vol. 1992, p. 1447, jan 1992.

[32] P. Gillis, A. Roch, and R. A. Brooks, "Corrected equations for susceptibility-induced T2-shortening.," *J Magn Reson*, vol. 137, pp. 402–407, apr 1999.

[33] A. Roch, Y. Gossuin, R. N. Muller, and P. Gillis, "Superparamagnetic colloid suspensions: Water magnetic relaxation and clustering," *J Magn Magn Mater*, vol. 293, pp. 532–539, 2005.

[34] Q. L. Vuong, P. Gillis, and Y. Gossuin, "Monte Carlo Simulation and Theory of Proton NMR Transverse Relaxation Induced by Aggregation of Magnetic Particles Used as MRI Contrast Agents.," *J Magn Reson*, vol. 212, pp. 139–148, sep 2011.

[35] D. A. Yablonskiy and E. M. Haacke, "Theory of NMR Signal Behavior in Magnetically Inhomogeneous Tissues: The Static Dephasing Regime," *Magn Reson Med*, vol. 32, pp. 749–763, 1994.

[36] P. Gillis, F. Moiny, and R. A. Brooks, "On T2-shortening by strongly magnetized spheres: a partial refocusing model.," *Magn Reson Med*, vol. 47, pp. 257–263, feb 2002.

[37] P. C. Lauterbur, "Image Formation by Induced Local Interactions: Examples Employing Nuclear Magnetic Resonance," *Nature*, vol. 242, pp. 190–191, mar 1973.

[38] L. G. Hanson, "Introduction to Magnetic Resonance," 2009.

[39] Y. Gossuin, A. Hocq, P. Gillis, and Q. L. Vuong, "Physics of magnetic resonance imaging: from spin to pixel," *J Phys D Appl Phys*, vol. 43, p. 213001, 2010.

[40] R. W. Brown, Y.-C. N. Cheng, E. M. Haacke, M. R. Thompson, and R. Venkatesan, *Magnetic Resonance Imaging*. Chichester, UK: John Wiley & Sons Ltd, apr 2014.

[41] A. Haase, J. Frahm, D. Matthaei, W. Hanicke, and K.-D. Merboldt, "FLASH imaging. Rapid NMR imaging using low flip-angle pulses," *Journal of Magnetic Resonance (1969)*, vol. 67, pp. 258–266, apr 1986.

[42] J. Hennig, A. Nauerth, and H. Friedburg, "RARE imaging: A fast imaging method for clinical MR," *Magnetic Resonance in Medicine*, vol. 3, pp. 823–833, dec 1986.

[43] J. R. Reichenbach, R. Venkatesan, D. A. Yablonskiy, M. R. Thompson, S. Lai, and E. M. Haacke, "Theory and Application of Static Field Inhomogeneity Effects in Gradient- Echo Imaging," *J Magn Reson Imaging*, vol. 7, pp. 266–279, 1997.

[44] J. Hennig, "Multiecho Imaging Sequenceswith Low Refocusing Flip Angles," *Journal of Magnetic Resonance*, vol. 78, pp. 397–407, 1988.

[45] A. J. Miller and P. M. Joseph, "The use of power images to perform quantitative analysis on low SNR MR images.," *Magnetic resonance imaging*, vol. 11, no. 7, pp. 1051–6, 1993.

[46] J. G. Raya, O. Dietrich, A. Horng, J. Weber, M. F. Reiser, and C. Glaser, "T 2 measurement in articular cartilage: Impact of the fitting method on accuracy and precision at low SNR," *Magnetic Resonance in Medicine*, pp. NA–NA, 2009.

[47] O. M. Girard, J. Du, L. Agemy, K. N. Sugahara, V. R. Kotamraju, E. Ruoslahti, G. M. Bydder, and R. F. Mattrey, "Optimization of iron oxide nanoparticle detection using ultrashort echo time pulse sequences: comparison of T1, T2*, and synergistic T1- T2* contrast mechanisms.," *Magnetic Resonance in Medicine*, vol. 65, no. 6, pp. 1649–60, 2011.

[48] S. Bidhult, C. G. Xanthis, L. L. Liljekvist, G. Greil, E. Nagel, A. H. Aletras, E. Heiberg, and E. Hedström, "Validation of a new t2* algorithm and its uncertainty value for cardiac and liver iron load determination from MRI magnitude images," *Magnetic Resonance in Medicine*, pp. n/a–n/a, may 2015.

[49] D. Milford, N. Rosbach, M. Bendszus, and S. Heiland, "Mono-Exponential Fitting in T2-Relaxometry: Relevance of Offset and First Echo," *PLOS ONE*, vol. 10, p. e0145255, dec 2015.

[50] S. Majumdar, A. Gmitro, S. C. Orphanoudakis, D. Reddy, and J. C. Gore, "An estimation and correction scheme for system imperfections in multiple-echo magnetic resonance imaging," *Magnetic Resonance in Medicine*, vol. 4, pp. 203–220, mar 1987.

[51] R. M. Lebel and A. H. Wilman, "Transverse relaxometry with stimulated echo compensation," *Magnetic Resonance in Medicine*, vol. 64, pp. 1005–1014, jun 2010.

[52] T. Prasloski, B. Mädler, Q.-S. Xiang, A. MacKay, and C. Jones, "Applications of stimulated echo correction to multicomponent T2 analysis," *Magnetic Resonance in Medicine*, vol. 67, pp. 1803–1814, jun 2012.

[53] N. Ben-Eliezer, D. K. Sodickson, and K. T. Block, "Rapid and accurate T 2 mapping from multi-spin-echo data using Bloch-simulation-based reconstruction," *Magnetic Resonance in Medicine*, vol. 73, pp. 809–817, feb 2015.

[54] W. C. Elmore, "The Magnetization of Ferromagnetic Colloids," *Phys Rev*, vol. 54, pp. 1092–1095, 1938.

[55] C. P. Bean, "Hysteresis Loops of Mixtures of Ferromagnetic Micropowders," *J Appl Phys*, vol. 26, pp. 1381–1383, nov 1955.

[56] C. Kittel, "Physical Theory of Ferromagnetic Domains," *Rev Mod Phys*, vol. 21, pp. 541–583, 1949.

[57] E. H. Frei, S. Shtrikman, and D. Treves, "Critical Size and Nucleation Field of Ideal Ferromagnetic Particles," *Phys Rev*, vol. 106, pp. 446–455, 1957.

[58] L. Néel, "Theorie du Trainage Magnetique des Ferromagnetiques en Grains Fins avec Applications aux Terres Cuites," *Ann Geophys*, vol. 5, p. 99, 1949.

[59] J. L. Dormann, "Le phénomène de superparamagnétisme," *Revue Phys Appl*, vol. 16, pp. 275–301, jan 1981.

[60] P. Debye, *Polar Molecules*. Chemical Catalog Company, New York, 1929.

[61] R. L. Mössbauer, "Kernresonanzfluoreszenz von Gammastrahlung in Ir191," *Zeitschrift für Physik*, vol. 151, pp. 124–143, 1958.

[62] W. Kündig, H. Bömmel, G. Constabaris, and R. H. Lindquist, "Some Properties of Supported Small a-Fe2O3 Particles Determined with the Mössbauer Effect," *Phys Rev*, vol. 142, pp. 327–333, 1966.

[63] S. Morup, M. F. Hansen, and C. Frandsen, "Magnetic Nanoparticles," in *Comprehensive Nanoscience and Technology* (D. L. Andrews, G. D. Scholes, and G. P. Wiederrecht, eds.), pp. 433–487, Oxford: Academic Press, 2011.

[64] E. Tronc, P. Prene, J. P. Jolivet, F. D'Orazio, F. Lucari, D. Fiorani, M. Godinho, R. Cherkaoui, M. Nogues, and J. L. Dormann, "Magnetic behaviour of y-Fe2O3 nanoparticles by Mössbauer spectroscopy and magnetic measurements," *Hyperfine Interact*, vol. 95, pp. 129–148, 1995.

[65] G. Shirane, D. E. Cox, W. J. Takei, and S. L. Ruby, "A Study of the Magnetic Properties of the FeTiO3-aFe2O3 System by Neutron Diffraction and the Mössbauer Effect," *J Phys Soc Jpn*, vol. 17, pp. 1598–1611, 1962.

[66] T. Nakamura, T. Seinjo, Y. Endoh, N. Yamamoto, M. Shiga, and Y. Nakamura, "Fe57 Mössbauer Effect in Ultra Fine Particles of a-Fe2O3," *Phys Lett*, vol. 12, pp. 178–179, 1964.

[67] H. H. Wickman, M. P. Klein, and D. A. Shirley, "Paramagnetic Hyperfine Structure and Relaxation Effects in Mössbauer Spectra - Fe57 in Ferrichrome A," *Phys Rev*, vol. 152, pp. 345–357, 1966.

[68] B. Gleich and J. Weizenecker, "Tomographic imaging using the nonlinear response of magnetic particles," *Nature*, vol. 435, pp. 1214–1217, jun 2005.

[69] T. M. Buzug, G. Bringout, M. Erbe, K. Gräfe, M. Graeser, M. Grüttner, A. Halkola, T. F. Sattel, W. Tenner, H. Wojtczyk, J. Haegele, F. M. Vogt, J. Barkhausen, and K. Lüdtke-Buzug, "Magnetic particle imaging: Introduction to imaging and hardware realization," *Zeitschrift für Medizinische Physik*, vol. 22, pp. 323–334, dec 2012.

[70] P. W. Goodwill, E. U. Saritas, L. R. Croft, T. N. Kim, K. M. Krishnan, D. V. Schaffer, and S. M. Conolly, "X-Space MPI: Magnetic Nanoparticles for Safe Medical Imaging," *Advanced Materials*, vol. 24, pp. 3870–3877, jul 2012.

[71] M. Kaul, O. Weber, U. Heinen, A. Reitmeier, T. Mummert, C. Jung, N. Raabe, T. Knopp, H. Ittrich, and G. Adam, "Combined Preclinical Magnetic Particle Imaging and Magnetic Resonance Imaging: Initial Results in Mice," *RöFo - Fortschritte auf dem Gebiet der Röntgenstrahlen und der bildgebenden Verfahren*, vol. 187, pp. 347–352, apr 2015.

[72] S. Biederer, T. Knopp, T. F. Sattel, K. Lüdtke-Buzug, B. Gleich, J. Weizenecker, J. Borgert, and T. M. Buzug, "Magnetization response spectroscopy of superparamagnetic nanoparticles for magnetic particle imaging," *Journal of Physics D: Applied Physics*, vol. 42, p. 205007, oct 2009.

[73] N. Löwa, F. Wiekhorst, I. Gemeinhardt, M. Ebert, J. Schnorr, S. Wagner, M. Taupitz, and L. Trahms, "Cellular Uptake of Magnetic Nanoparticles Quantified by Magnetic Particle Spectroscopy," *IEEE Transactions on Magnetics*, vol. 49, pp. 275–278, jan 2013.

[74] W. C. Poller, N. Löwa, F. Wiekhorst, M. Taupitz, S. Wagner, K. Möller, G. Baumann, V. Stangl, L. Trahms, and A. Ludwig, "Magnetic Particle Spectroscopy Reveals Dynamic Changes in the Magnetic Behavior of Very Small Superparamagnetic Iron Oxide Nanoparticles During Cellular Uptake and Enables Determination of Cell-Labeling Efficacy," *Journal of Biomedical Nanotechnology*, vol. 12, pp. 337–346, feb 2016.

[75] D. Eberbeck and L. Trahms, "Experimental investigation of dipolar interaction in suspensions of magnetic nanoparticles," *J Magn Magn Mater*, vol. 323, pp. 1228–1232, may 2011.

[76] D. Eberbeck, F. Wiekhorst, S. Wagner, and L. Trahms, "How the size distribution of magnetic nanoparticles determines their magnetic particle imaging performance," *Applied Physics Letters*, vol. 98, no. 18, p. 182502, 2011.

[77] R. M. Cornell and U. Schwertmann, *The Iron Oxides*. Weinheim: Wiley-VCH Verlag GmbH & Co. KGaA, 2003.

[78] R. Bauminger, S. G. Cohen, A. Marinov, S. Ofer, and E. Segal, "Study of the low-temperature transition in magnetite and the internal fields acting on iron nuclei in some spinel ferrites, using Mössbauer absorption," *Phys Rev*, vol. 122, pp. 1447–1450, 1961.

[79] G. M. Da Costa, E. De Grave, and R. E. Vandenberghe, "Mössbauer studies of magnetite and Al-substituted maghemites," *Hyperfine Interact*, vol. 117, pp. 207–243, 1998.

[80] W. Kündig and R. S. Hargrove, "Electron Hopping in Magnetite," *Solid State Commun*, vol. 7, pp. 223–227, 1969.

[81] G. A. Sawatzky, J. M. D. Coey, and A. H. Morrish, "Mössbauer Study of Electron Hopping in the Octahedral Sites of Fe3O4," *J Appl Phys*, vol. 40, pp. 1402–1403, 1969.

[82] I. Dézsi, C. Fetzer, Á. Gombkötö, I. Szücs, and J. Gubicza, "Phase transition in nanomagnetite," *J Appl Phys*, vol. 103, p. 104312, 2008.

[83] E. J. W. Verwey, "Electronic Conduction of Magnetite (Fe3O4) and its Transition Point at Low Temperatures," *Nature*, vol. 144, pp. 327–328, 1939.

[84] F. J. Berry, S. Skinner, and M. F. Thomas, "57Fe Mössbauer spectroscopic examination of a single crystal of Fe3O4," *J Phys: Condens Matter*, vol. 10, pp. 215–220, 1998.

[85] A. C. Doriguetto, N. G. Fernandes, A. I. C. Persiano, E. Nunes Filho, J. M. Grenèche, and J. D. Fabris, "Characterization of a natural magnetite," *Phys Chem Miner*, vol. 30, no. 5, pp. 249–255, 2003.

[86] M. J. Graham, D. A. Channing, G. A. Swallow, and R. D. Jones, "A Mössbauer study of the reduction of hematite in hydrogen at 535 degree Celsius," *J Mater Sci*, vol. 10, no. 7, pp. 1175–1181, 1975.

[87] I. Mitov, Z. Cherkezova-Zheleva, and V. Mitrov, "Comparative Study of the Mechanochemical Activation of Magnetite (Fe3O4) and Maghemite (γ-Fe2O3)," *Phys Stat Sol (a)*, vol. 161, pp. 475–482, 1997.

[88] S. Kamali-M, T. Ericsson, and R. Wäppling, "Characterization of iron oxide nanoparticles by Mössbauer spectroscopy," *Thin Solid Films*, vol. 515, pp. 721–723, 2006.

[89] J. Santoyo Salazar, L. Perez, O. de Abril, L. Truong Phuoc, D. Ihiawakrim, M. Vazquez, J.-M. Greneche, S. Begin-Colin, and G. Pourroy, "Magnetic Iron Oxide Nanoparticles in 10-40 nm Range: Composition in Terms of Magnetite/Maghemite Ratio and Effect on the Magnetic Properties," *Chem Mater*, vol. 23, pp. 1379–1386, mar 2011.

[90] M. D. Carvalho, F. Henriques, L. P. Ferreira, M. Godinho, and M. M. Cruz, "Iron oxide nanoparticles - the influence of synthesis method and size on composition and magnetic properties," *J Solid State Chem*, vol. 201, pp. 144–152, 2013.

[91] S. Morup and H. Topsoe, "Magnetic And Electronic Properties Of Microcrystals Of Fe3O4," *J Magn Magn Mater*, vol. 31-34, pp. 953–954, 1983.

[92] M. Eibschütz and S. Shtrikman, "Restoration of Motionally Narrowed Hyperfine Splitting in Superparamagnetic Particles by Magnetic Field," *J Appl Phys*, vol. 39, pp. 997–998, 1968.

[93] R. H. Lindquist, G. Constabaris, W. Kündig, and A. M. Portis, "Mössbauer Spectra of 57Fe in Superparamagnetic Nickel," *J Appl Phys*, vol. 39, pp. 1001–1003, 1968.

[94] E. Tronc, A. Ezzir, R. Cherkaoui, C. Chanéac, M. Nogues, H. Kachkachi, D. Fiorani, A. M. Testa, J. M. Grenèche, and J. P. Jolivet, "Surface-related properties of y-Fe2O3 nanoparticles," *J Magn Magn Mater*, vol. 221, pp. 63–79, 2000.

[95] W. Chen, S. Morup, M. F. Hansen, T. Banert, and U. A. Peuker, "A Mössbauer study of the chemical stability of iron oxide nanoparticles in PMMA and PVB beads," *J Magn Magn Mater*, vol. 320, pp. 2099–2105, 2008.

[96] S. Morup, F. Bodker, P. V. Hendriksen, and S. Linderoth, "Spin-glass-like ordering of the magnetic moments of interacting nanosized maghemite particles," *Phys Rev B*, vol. 52, pp. 287–294, jul 1995.

[97] L. T. Kuhn, A. Bojesen, L. Timmermann, M. Meedom Nielsen, and S. Morup, "Structural and magnetic properties of core-shell iron-iron oxide nanoparticles," *J Phys: Condens Matter*, vol. 14, pp. 13551–13567, 2002.

[98] D. H. Jones and K. K. P. Srivastava, "Many-state relaxation model for the Mössbauer spectra of superparamagnets," *Phys Rev B*, vol. 34, pp. 7542–7548, 1986.

[99] S. Morup and P. H. Christensen, "Magnetic Hyperfine Splitting in Superparamagnetic Particles in External Magnetic Fields," *J Magn Magn Mater*, vol. 68, pp. 160–170, 1987.

[100] M. A. Chuev, "Multilevel Relaxation Model for Describing the Mössbauer Spectra of Nanoparticles in a Magnetic Field," *J Exp Theor Phys*, vol. 114, pp. 609–630, 2012.

[101] K. Halbach, "Design of permanent multipole magnets with oriented rare earth cobalt material," *Nucl Instrum Methods*, vol. 169, pp. 1–10, 1980.

[102] C. Rümenapp, F. E. Wagner, and B. Gleich, "Monitoring of the aging of magnetic nanoparticles using Mössbauer spectroscopy," *J Magn Magn Mater*, vol. 380, pp. 241–245, 2015.

[103] C. Rümenapp, B. Gleich, H. G. Mannherz, and A. Haase, "Detection of molecules and cells using nuclear magnetic resonance with magnetic nanoparticles," *J Magn Magn Mater*, vol. 380, pp. 271–275, 2015.

[104] D. Forge, A. Roch, S. Laurent, H. Tellez, Y. Gossuin, F. Renaux, L. V. Elst, and R. N. Muller, "Optimization of the synthesis of superparamagnetic contrast agents by the design of experiments method," *J Phys Chem C*, vol. 112, no. 49, pp. 19178–19185, 2008.

[105] E. E. Finney and R. G. Finke, "Nanocluster nucleation and growth kinetic and mechanistic studies: A review emphasizing transition-metal nanoclusters," *J Colloid Interface Sci*, vol. 317, no. 2, pp. 351–374, 2008.

[106] J.-C. Bacri, R. Perzynski, D. Salin, V. Cabuil, and R. Massart, "Ionic ferrofluids: A crossing of chemistry and physics," *J Magn Magn Mater*, vol. 85, no. 1-3, pp. 27–32, 1990.

[107] N. C. Bell, C. Minelli, J. Tompkins, M. M. Stevens, and A. G. Shard, "Emerging Techniques for Submicrometer Particle Sizing Applied to Stöber Silica," *Langmuir*, vol. 28, no. 29, pp. 10860–10872, 2012.

[108] R. N. Muller, P. Gillis, F. Moiny, and A. Roch, "Transverse Relaxivity of Particulate MRI Contrast Media: from Theories to Experiments," *Magn Reson Med*, vol. 22, pp. 178–182, 1991.

[109] Q. L. Vuong, J.-F. Berret, J. Fresnais, Y. Gossuin, and O. Sandre, "A Universal Scaling Law to Predict the Effi ciency of Magnetic Nanoparticles as MRI T2-Contrast Agents," *Adv Healthcare Mater*, vol. 1, pp. 502–512, 2012.

[110] J. B. Haun, T.-J. Yoon, H. Lee, and R. Weissleder, "Magnetic nanoparticle biosensors," *WIREs Nanomed Nanobiotechnol*, vol. 2, pp. 291–304, 2010.

[111] P. A. Hardy and R. M. Henkelman, "Transverse Relaxation Rate Enhancement Caused by Magnetic Particulates," *Magn Reson Imaging*, vol. 7, pp. 265–275, jan 1989.

[112] Y. Matsumoto and A. Jasanoff, "T2 relaxation induced by clusters of superparamagnetic nanoparticles: Monte Carlo simulations," *Magn Reson Imaging*, vol. 26, pp. 994–998, 2008.

[113] K. A. Brown, C. C. Vassiliou, D. Issadore, J. Berezovsky, M. J. Cima, and R. M. Westervelt, "Scaling of transverse nuclear magnetic relaxation due to magnetic nanoparticle aggregation," *J Magn Magn Mater*, vol. 322, pp. 3122–3126, 2010.

[114] N. Löwa, P. Radon, D. Gutkelch, R. August, and F. Wiekhorst, "Hyphenation of Field-Flow Fractionation and Magnetic Particle Spectroscopy," *Chromatography*, vol. 2, pp. 655–668, nov 2015.

[115] C. W. Jung and P. Jacobs, "Physical and chemical properties of superparamagnetic iron oxide MR contrast agents: Ferumoxides, ferumoxtran, ferumoxsil," *Magnetic Resonance Imaging*, vol. 13, pp. 661–674, jan 1995.

[116] M. F. Casula, P. Floris, C. Innocenti, A. Lascialfari, M. Marinone, M. Corti, R. A. Sperling, W. J. Parak, and C. Sangregorio, "Magnetic Resonance Imaging Contrast Agents Based on Iron Oxide Superparamagnetic Ferrofluids," *Chemistry of Materials*, vol. 22, pp. 1739–1748, mar 2010.

[117] J. Lohrke, *Herstellung und Charakterisierung neuer nanopartikulaerer SPIO-Kontrastmittel fuer die Magnetresonanztomographie*. PhD thesis, Martin-Luther-Universität Halle-Wittenberg, 2010.

[118] R. M. Ferguson, A. P. Khandhar, and K. M. Krishnan, "Tracer design for magnetic particle imaging (invited)," *Journal of Applied Physics*, vol. 111, no. 7, p. 07B318, 2012.

[119] P. J. Wyatt, "Mean square radius of molecules and secondary instrumental broadening," *Journal of Chromatography A*, vol. 648, pp. 27–32, oct 1993.

[120] D.-X. Chen, G. Via, F.-J. Xu, C. Navau, and A. Sanchez, "Waiting time dependence of T2 of protons in water suspensions of iron-oxide nanoparticles: Measurements and simulations," *J Appl Phys*, vol. 110, p. 73917, 2011.

[121] A. F. Thunemann, S. Rolf, P. Knappe, and S. Weidner, "In Situ Analysis of a Bimodal Size Distribution of Superparamagnetic Nanoparticles," *Analytical Chemistry*, vol. 81, pp. 296–301, jan 2009.

[122] F. Ludwig, H. Remmer, C. Kuhlmann, T. Wawrzik, H. Arami, R. M. Ferguson, and K. M. Krishnan, "Self-consistent magnetic properties of magnetite tracers optimized for magnetic particle imaging measured by ac susceptometry, magnetorelaxometry and magnetic particle spectroscopy," *Journal of Magnetism and Magnetic Materials*, vol. 360, pp. 169–173, jun 2014.

[123] M. Graeser, K. Bente, and T. M. Buzug, "Dynamic single-domain particle model for magnetite particles with combined crystalline and shape anisotropy," *Journal of Physics D: Applied Physics*, vol. 48, p. 275001, jun 2015.

[124] C. Alexiou, R. Tietze, E. Schreiber, R. Jurgons, H. Richter, L. Trahms, H. Rahn, S. Odenbach, and S. Lyer, "Cancer therapy with drug loaded magnetic nanoparticles—magnetic drug targeting," *Journal of Magnetism and Magnetic Materials*, vol. 323, pp. 1404–1407, may 2011.

[125] I. Almstätter, O. Mykhaylyk, M. Settles, J. Altomonte, M. Aichler, A. Walch, E. J. Rummeny, O. Ebert, C. Plank, and R. Braren, "Characterization of Magnetic Viral Complexes for Targeted Delivery in Oncology," *Theranostics*, vol. 5, no. 7, pp. 667–685, 2015.

[126] O. Mykhaylyk, Y. S. Antequera, D. Vlaskou, and C. Plank, "Generation of magnetic nonviral gene transfer agents and magnetofection in vitro," *Nature Protocols*, vol. 2, pp. 2391–2411, oct 2007.

[127] O. Mykhaylyk, T. Sobisch, I. Almstätter, Y. Sanchez-Antequera, S. Brandt, M. Anton, M. Döblinger, D. Eberbeck, M. Settles, R. Braren, D. Lerche, and C. Plank, "Silica-iron oxide magnetic nanoparticles modified for gene delivery: A search for optimum and quantitative criteria," *Pharmaceutical Research*, vol. 29, no. 5, pp. 1344–1365, 2012.

[128] C. E. Krill and R. Birringer, "Estimating grain-size distributions in nanocrystalline materials from X-ray diffraction profile analysis," *Philosophical Magazine A*, vol. 77, pp. 621–640, mar 1998.

[129] J. Torrance and T. Bothwell, *Tissue Iron Stores*. New York: Churchill Livingstone, 1980.

[130] O. Dietrich, J. G. Raya, S. B. Reeder, M. F. Reiser, and S. O. Schoenberg, "Measurement of signal-to-noise ratios in MR images: influence of multichannel coils, parallel imaging, and reconstruction filters.," *Journal of magnetic resonance imaging : JMRI*, vol. 26, pp. 375–85, aug 2007.

List of Publications

Peer-Reviewed Articles

- **A. Joos**[1], C. Rümenapp[1], F. E. Wagner, and B. Gleich , "Characterisation of iron oxide nanoparticles by Mössbauer spectroscopy at ambient temperature", *J Magn Magn Mater*, vol. 399, pp. 123-129, 2016
- **A. Joos**, N. Löwa, F. Wiekhorst, B. Gleich and A. Haase, "Size-dependent MR relaxivities of magnetic nanoparticles", *J Magn Magn Mater*, vol. 427, pp. 122-126, 2017
- J. M. S. e Silva, J. Utsch, **A. Joos**, C. Rümenapp, J. Marciniszyn, B. Gleich, F. Pfeiffer, "A novel approach to workflow analysis in magnetic nanoparticles-based biomedical research", submitted to the *Journal of Nanobiotechnology*, 2017

Conference Contributions

- **A. Joos**, O. Mykhaylyk, B. Gleich, A. Haase, "Multiparametric MRI characterisation of Magnetic Viral Complexes", *International Conference on Magnetic Resonance Microscopy*, 2015 (poster)
- **A. Joos**, O. Mykhaylyk, B. Gleich, A. Haase, "Multiparametric MRI characterisation of Magnetic Viral Complexes", *Annual Meeting of the European Society of Magnetic Resonance in Medicine and Biology*, 2015 (poster)
- **A. Joos**, O. Mykhaylyk, N. Löwa, D. Eberbeck, B. Gleich, A. Haase, "Multiparametric MRI characterisation of Magnetic Viral Complexes", *Annual Meeting of the International Society for Magnetic Resonance in Medicine*, 2016 (oral presentation)
- **A. Joos**, N. Löwa, S. Düwel, C. Hundshammer, F. Wiekhorst, B. Gleich, A. Haase, "Size-dependent MR relaxivities of magnetic nanoparticles", *11th International Conference on the Scientific and Clinical Applications of Magnetic Carriers*, 2016 (poster)

[1] contributed equally

Acknowledgements

I would like to thank those who have guided, supported and helped me during the course of my PhD

- Prof. Axel Haase for giving me the opportunity to perform my PhD under his supervision, for his ideas, support and his patience with my numerous questions during our scientific discussions.
- Dr. Bernhard Gleich for his patience, his support and his outstanding commitment at the IMETUM.
- Dr. Anh Van Tu for helping me with Matlab problems and with the 3 Tesla MRI at the IMETUM and for the scientific discussions.
- Dr. Alexandra Heidsieck for helping me with Matlab.
- Dr. Christine Rümenapp for her support and working with me on the Mössbauer project.
- My other colleagues Stephan, Christoph and Andi for the nice conversations, especially during our traditional lunch sessions.
- Dr. Franz Schilling and Dr. Geoffrey Topping for helping me with the 7 Tesla MRI at the Klinikum rechts der Isar.
- Prof. Fritz Wagner from the Physics Department for performing the Mössbauer measurements and data analysis and for sharing his knowledge and expertise during our extensive discussions about Mössbauer spectroscopy and our Mössbauer project.
- Dr. Norbert Löwa, Dr. Dietmar Eberbeck and Dr. Frank Wiekhorst from the Physikalisch-Technische Bundesanstalt in Berlin for performing the hydrodynamic fractionation, the MPS and M(H) measurements, for hosting me during my internship at the PTB and for many scientific discussions.
- Dr. Olga Mykhaylyk for manufacturing the magnetic viral complexes.

- Susanne Schnell-Witteczek and Sepp Hintermair for their practical support at the IMETUM.
- Dr. Peter Bendel from Aspect Imaging for helping me with the experimental difficulties on the 1 Tesla MRI.
- Dr. Marianne Hanzlik from the Department of Chemistry for acquiring the transmission electron microscopy image of the magnetic nanoparticles and Dr. Matthias Opel from the Walther-Meissner Institute for measuring the M(H) curve shown in the Mössbauer chapter.
- Stephan Düwel and Christian Hundshammer for their help with the relaxation measurements at the Klinikum rechts d. Isar.
- Last but not least: my family - especially my parents Julia and Walter - and my friends for their great support and my girlfriend Bhedita Seewoo for her patience during the writing phase of my thesis.

Additionally, my PhD would not have been feasable without the financial support from the German Academic Scholarship Foundation and the German Research Foundation through the DFG Research Unit FOR917.